INTEGRATIVE REMOTE SENSING APPLICATIONS TO UNDERSTANDING NOCTILUCENT CLOUDS AND THE GREENLAND ICE SHEET

by

JASON DAVID REIMULLER

B.S., Florida Institute of Technology, l995

M.S., San Francisco State University, 2003

M.S., University of Tennessee, Knoxville, 2006

M.S., University of Colorado, Boulder, 2007

A thesis submitted to the

Faculty of the Graduate School of the

University of Colorado in partial fulfillment

of the requirement for the degree of

Doctor of Philosophy

Department of Aerospace Engineering Sciences

2011

This thesis entitled:

Integrative Remote Sensing Applications to Understanding Noctilucent Clouds and the Greenland Ice Sheet
written by Jason David Reimuller
has been approved for the Department of Aerospace Engineering Sciences

_____
Jeffrey Thayer

_____
Waleed Abdalati

*Date*_____

The final copy of this thesis has been examined by the signatories, and we Find that both the content and the form meet acceptable presentation standards Of scholarly work in the above mentioned discipline.

Reimuller, Jason David (Ph.D., Aerospace Engineering Sciences)

Integrative Remote Sensing Applications to Understanding Noctilucent Clouds and the Greenland Ice Sheet

Thesis directed by Associate Professor Jeffrey P. Thayer

Integrative remote sensing methods are effective in the study of large heterogeneous phenomena that contribute towards our understanding of global climatological trends. This study focuses upon two climatological subjects of integrative remote sensing techniques: glaciers and noctilucent clouds. Glaciers are considered among the most sensitive observable effects of climate change, whereas noctilucent clouds provide a means to observe the trends of a changing atmospheric composition. Through synchronized aircraft and spacecraft observations, this study verified for the first time that synchronous imagery of noctilucent cloud structures from airborne and spaceborne platforms could be obtained as similar band structures were identified, along with orthogonal structures only perceptible by the aircraft imagers. This helped to validate the processing algorithm at the day-to-night solar terminator of the Cloud Imagery and Particle Size (CIPS) instrument on the NASA Aeronomy of Ice in the Mesosphere (AIM) satellite.

Furthermore, integrative methods were successful in determining the sliding component of glacial motion along the flowlines leading to the Sermeq Avannarleq glacier in Greenland and correlating this component to bedrock topography. Using a combination of airborne, spaceborne, and in-situ measurements, it was found that the initial onset of sliding occurs near the equilibrium line, quickly constituting approximately half of overall motion and increase steadily to the terminus, providing insight to positive feedback mechanisms that could accelerate glacial disintegration.

DEDICATION

To my grandfather, B/Gen. Willis Fred Chapman

ACKNOWLEDGEMENTS

I would like to first acknowledge the support of Dr. Jeffrey Thayer and Dr. Waleed Abdalati. To Jeff for his constant support of my endeavors and his patience for my meandering nature. And to Waleed for his confidence in my success and his support in opening new doors and directions when they were needed the most.

I would also like to acknowledge the support of Bruce Hulley as being essential to the successful completion of the flight research aspects of this study as well as to my maturation as an aviator, which has become a critical skill in my developing profession, and for negotiating the incessant drama of aircraft acquisitions.

I would also like to acknowledge the support of Dr. Tad Pfeffer, who first opened the doors for me to get involved with glacial science and then saw through my understanding of glaciology, as well as the support of Dr. Brian Argrow, whose expertise in airborne remote sensing was vital to my research, and the support of Dr. Peter Pilewskie, who laid a solid foundation to my understanding of remote sensing principles.

To Dr. Harihar Rajaram for his patient support in bringing me from the depths of MATLAB ignorance to a level of fluency in numerical modeling techniques.

To William Colgan and Dr. Thomas Phillips, without whose invaluable support I would have never been able to adapt to the new challenges and rewards that glacial research brought to me.

To Dr. Jay Falker, Dave Forrest, Gordon Aaseng, and all the amazing people at NASA that have allowed me the freedom to continue my research and studies while being fully engaged with the Constellation Program, and their confidence in me as a developing systems engineer.

To Dr. David Rusch, Dr. William McClintock, Dr. Scott Bailey, and Dr. Aimee Merkel of the Laboratory for Atmospheric and Space Physics for the opportunities to be involved with the AIM mission that they have provided to me as well as for their assistance in the post-campaign interpretations of the results of the noctilucent flight campaign

To Dr. Gerd Baumgarten and Dr. Amal Chandran for their assistance in the geolocation of noctilucent cloud imagery and of flight data.

I would also like to acknowledge the support received from the National Aeronautics and Space Administration (NASA) and the National Science Foundation (NSF) in the form of funding from NSF project ATM-0930658 and NASA Earth and Space Science Fellowship (NESSF) NNX07AO82.

Finally, I would like to acknowledge my kinfolk whose continued support is invaluable. In particular, to my parents Patricia Chapman and David Reimuller, to Jason Gatten, Mike Hinke, and to John Winternitz for helping me to keep things in perspective, and to Chris Lundeen for always reminding me to keep a healthy play ethic.

CONTENTS

TABLES

FIGURES

1. Introduction

Our current understanding of global climate change derives from global climate models that integrate both natural and anthropogenic elements. These models iterate the complicated interconnections between atmospheric composition and dynamics with other observables, commonly obtained through remote sensing methods.

The known natural drivers of global climate change include solar output, orbital variations, volcanism, and ocean processes. The net radiative input to the Earth is predominantly produced by the sun, and both long- and short-term variations in solar intensity are known to affect global climate. Milankovitch cycles, produced through a combination of variations in the eccentricity of Earth's orbit, the tilt of the Earth's axis, and precession, are an additional driver of climatic variability as these slight variations lead to changes in the seasonal distribution of sunlight reaching the Earth's surface [Qin et al., 2007]. Volcanism is also considered a driver of climatic variability as large eruptions can affect the radiative balance of the Earth and cause brief periods of cooling by partially blocking the transmission of incident solar radiation [Gerlach, 2011]. Finally, the thermohaline circulation redistributes heat globally through a slow and very deep redistribution of water throughout the Earth's oceans [Knauss, 1996].

However, it is generally accepted that global climate change is principally driven by anthropogenic, or man-made, causes largely through the atmospheric forcing of carbon dioxide (CO2), methane, nitrous oxide, and other gasses. Human activities such as the burning of oil, coal and gas, and deforestation, generate more than 100 times the amount of carbon dioxide emitted by volcanoes [Gerlach, 2011]. The increase of concentration of atmospheric CO2 from pre-industrial concentrations has doubled since 1980 and the present level is higher than at any

time during the last 800 thousand years (source: http://www.esrl.noaa.gov/gmd/ccgg/trends/). The US Environment Protection Agency (EPA) documents these known greenhouse gas emissions and sinks in the 'Inventory of U.S. Greenhouse Gas Emissions and Sinks: 1990-2009', results of which are summarized in the following paragraphs.

The largest source of anthropogenic CO_2 emissions globally is the combustion of fossil fuels such as coal, oil and gas in power plants, automobiles, industrial facilities and other sources. In addition, a number of specialized industrial production processes such as mineral production, metal production and the use of petroleum-based products also lead to CO_2 emissions. Furthermore, since trees and plants absorb or remove CO_2 from the atmosphere, deforestation can lead to increased levels of CO_2 emissions.

In addition to CO_2, methane (CH_4) is a significant driver of global climate change. The US EPA estimates that the majority of methane emissions comes from human-related activities such as fossil fuel production, animal husbandry (enteric fermentation in livestock and manure management), rice cultivation, biomass burning, and waste management. Natural sources of methane include wetlands, gas hydrates, permafrost, termites, oceans, freshwater bodies, non-wetland soils, and other sources such as wildfires.

Nitrous oxide (N_2O) is produced by both natural and human-related sources. Primary human-related sources of N_2O are agricultural soil management, animal manure management, sewage treatment, mobile and stationary combustion of fossil fuel, adipic acid production, and nitric acid production. Nitrous oxide is also produced naturally from a wide variety of biological sources in soil and water, particularly microbial action in wet tropical forests.

Numerous gasses are categorized as having a high potential to contribute to global warming due to their ability to catalyze reactions in the atmosphere. These gases are emitted from a variety of industrial processes including aluminum production, semiconductor manufacturing, electric power transmission, magnesium production and processing, and the production of HCFC-22. Chlorofluorocarbons (CFCs), hydrochlorofluorocarbons (HCFCs) and halons have long been known to deplete ozone in the atmosphere [Houghton et al., 2001].

1.1 Observable evidence of climate change

Evidence of climate change on or near the Earth's surface can be seen in 1) reduction in glacial volume, 2) shifts in vegetation, 3) shifts in dendroclimatology, 4) changes in the palynological record, and 5) changes in insect distribution. Vegetation is commonly used as an observable of climate change since a mild change in climate may result in increased precipitation and warmth, resulting in improved plant growth and the subsequent sequestration of airborne CO_2. Dendroclimatology is the study of tree rings, which provides insight into the distribution of rainfall. Palynology is the study of pollen and is used to infer the geographical distribution of plant species.

Glaciers are considered among the most sensitive indicators of climate change. Glacial size is determined by a mass balance between snow input and melt output, though observations must be averaged over decadal or longer time-scales and/or over many individual glaciers to smooth out the local short-term variability. The World Glacier Monitoring Service collects data annually on glacial retreat and glacial mass balance and has found glaciers globally to be shrinking significantly, with strong glacier retreats in the 1940s, stable or growing conditions during the 1920s and 1970s, and retreat from the mid 1980s to present [Zemp et al., 2008].

The Greenland Ice Sheet is often used as a proxy of climate change as it is the second largest ice sheet in the world, after the Antarctic Ice Sheet. It is a mass of ice that dates back to the Pleistocene, approximately 110,000 years ago, covers over 80% of the total surface area of Greenland (approximately 1,710,000 square kilometers), and rises to a mean elevation of 2135m [Meese et al., 1997]. The ice sheet is surrounded by small ice caps and various outlet glaciers. The best known of these outlet glaciers is Jakobshavn Isbræ, which is responsible for approximately 7% of the total loss component of the ice sheet's mass balance [Houghton et al., 2001]. Sermeq Avannarleq, located just north of Jacobshavn Isbrae and chosen as the region of interest in this study, is a location ideal to study these effects as it lies in an area starting to become dynamic and is well surveyed by radar, LiDAR, imagery, and in-situ observations from airborne, space-based, and ground-based observational platforms.

1.2 Observable indicators of atmospheric climate change

The remote sensing of the atmosphere has generally been focused on better characterizing the physical thermodynamical processes (atmospheric physics) and the chemical composition (atmospheric chemistry) of the atmosphere. Climate change is studied through analysis of the frequency and trends of meteorological systems over periods spanning years to millennia. In the upper layers of the atmosphere where dissociation and ionization become key factors, the atmosphere is particularly sensitive to the natural or human-induced factors that cause climates to change [Rishbeth and Roble, 1989].

Noctilucent clouds (NLCs), also referred to as Polar Mesospheric Clouds (PMCs) from space-based observations, have been observed in increasing frequency and geographic extent

throughout the last century [e.g. Zalcik, 1998; Thomas et al., 2003; Taylor, 2002]. This increase is seen by many scientists as a probable indicator of long-term global climate change as they are likely attributable to increasing levels of atmospheric 'greenhouse gasses', such as carbon dioxide and methane. Carbon dioxide warms the lower atmosphere, but radiate heat into space in the thin upper atmosphere. Thus, as carbon dioxide levels rise, the upper atmosphere cools. Further, as methane levels rise, more hydrogen is released through photo-disassociation in the middle atmosphere (~60km), which reacts with oxygen to form water vapor. Both of these effects increase PMC brightness and geospatial distribution [Thomas et al., 2003, von Zahn, U., 2003].

Over the past few decades NLCs have been considered an observable phenomena of the upper atmosphere that may also be a good indicator of global climate change, due to the direct relationship that has been observed between their presence and man-made industrial products, such as atmospheric aerosols from industrial gasses, water vapor from rocket exhaust, and warmer tropospheric temperatures driven by 'greenhouse processes' [Thomas et al., 2003].

The argument for PMC research was compellingly made by Dr. James Russell III, who is the principal investigator for NASA's Aeronomy of Ice in the Mesosphere (AIM) small explorer mission:

> *"It is clear that PMCs are changing, a sign that a distant and rarefied part of our atmosphere is being altered, and we do not understand how, why or what it means...These observations suggest a connection with global change in the lower atmosphere and could represent an early warning that our Earth's environment is being altered."*

It is becoming more and more evident that the industrial revolution has introduced the presence of NLCs. We know with certainty that methane, carbon dioxide, and water vapor all

trigger the presence of these clouds [von Zahn, et al, 2004; Thomas et al., 2003]. We have observed directly that the water vapor produced by the Space Shuttle's main engines trigger the formation of NLCs [Stevens et al., 2003]. Aeronomers and climate change scientists are interested in determining if 1) NLCs are extending and migrating to more equatorial latitudes, and if 2) NLCs are getting thicker and thus play a role in altering the albedo of the Earth and thus the thermodynamic balance of the Earth. Thus, by better understanding NLCs, we hope to gain insight into the elements of global climate change believed to cause their expanding presence.

1.3 Why NLCs and glaciers provide a good means to understand global climate trends

Integrative remote sensing methods support many studies that contribute elements towards our understanding of global climatological trends. As described previously, there are numerous observable effects of climate change that largely result from a changing atmospheric composition driven principally by the anthropogenic forcing of carbon dioxide and methane [Thomas, 2003; Roble and Dickinson, 1989]. This dissertation focuses upon two climatological subjects of integrative remote sensing techniques: glaciers and noctilucent clouds. Glaciers are considered among the most sensitive observable effects of climate change, whereas noctilucent clouds provide a means to observe the trends of a changing atmospheric composition.

There are several reasons why NLCs and the Greenland Ice Sheet have been chosen as foci in this study. Both NLCs and glaciers provide a means to observe effects of global climatic change, and thus they provide two different angles towards the understanding of broader changes in the Earth's climate system. The methods through which to study both have similarities as well. As noctilucent clouds consist largely of ice particles, ice dynamics play an essential part in

the study of both. In particular, the impacts of both are driven by the vertical characteristics of the ice dynamics. Further, large continental glaciers, such as the Greenland Ice Sheet, possess the same relative spatial scale as noctilucent cloud formations, and this drives the question of how to observe such large heterogeneous phenomena effectively. Due to this large relative size, the best ways to study the physical processes of the entire system generally involves an integration of space-based, ground-based, and airborne sensing techniques, where each sensing method brings a unique mix of spatial and temporal coverage and detail. It is because glaciers best represent the observable effects of climate change, noctilucent clouds represent well the observable effects of a changing atmospheric composition, and both phenomena contain several distinct similarities in common, that they were chosen to be the foci of the analyses presented within this dissertation.

1.4 Using integrative methods to address key issues associated with climate change

Due to the large relative size of both continental glaciers and noctilucent cloud structures, the best ways to study the physical processes of the entire system generally involves an integration of space-based, ground-based, and airborne sensing techniques, where each sensing method brings a unique mix of spatial and temporal coverage and detail. The remote sensing techniques used, and the integrative methods employed, in the study of both glaciers and noctilucent clouds are similar, though they may be applied in very different ways. For both applications, critical information may best be obtained through airborne remote sensing techniques, as aircraft mounted instrumentation may provide an essential mix of large spatial coverage and fine detail. In both cases, the data sensed from airborne platforms are then combined with satellite data and ground-based observations to provide a more comprehensive

understanding of the climatic trends behind the observable phenomena in the most sensitive and difficult to model areas.

1.4.1 Employing integrative methods to understand NLC formations at the day-night terminator

The day-night terminator resides near the low-latitude threshold of NLC cloud formations near local midnight. As NLCs represent a means to observe the trends of a changing atmospheric composition, the low-latitude thresholds of NLCs contain the most tenuous cloud structures and are thus the region of observables most sensitive to external climate forcing. It is for this reason we seek a comprehensive means to observe this region, though prior observations have shown a gap between the imagery obtainable from space-based imagers and ground-based observations.

Spaceborne imagers have not been successful in extracting detail in the low-latitude regions near the day-night terminator since the ultraviolet (UV) background, used to produce an optimal signal-to-noise ratio (SNR) for NLC observations, generally resides near stratopause altitudes (~48km) and thus confines NLC observations to higher latitudes. Conversely, ground-based imagery at visible wavelengths is confined to low latitudes where the background illumination of lower levels of atmosphere can be shadowed by the Earth. Synchronized observations between spaceborne platforms and ground observation stations have been limited because of the challenging and opposing conditions for optimal observing by satellite and ground cameras. Satellite observations require sufficiently scattered sunlight which diminishes appreciably as the satellite transitions through the day-to-night terminator. Ground cameras require reduced background signals while sunlight illuminates the higher altitudes. Furthermore,

the requisite low solar depression angles consist of rays passing through the lower atmosphere prior to their scattering from particulates in the upper mesosphere altitudes where NLCs reside (~83km). The sensitivity of the ultraviolet (UV) imagery produced by the Cloud Imagery and Particle Size (CIPS) experiment onboard the AIM satellite can thus be confined by the UV terminator where stratospheric ozone can attenuate the signal, yielding imagery only at latitudes poleward of about six degrees south of the terminator. Notable efforts to synchronize imagery of ground-based NLCs with space-based PMC observations have been performed recently [Baumgarten et al., 2009a]. Coincident measurements of NLCs have also been performed between ground-based optical cameras, the Poker Flat incoherent scatter radar, and lidar at Poker Flats, AK in 2007 and characterized from different viewing geometries and scattering properties [Taylor et al., 2009].

With the successful launch in April 2007 of the Aeronomy of Ice in the Mesosphere (AIM) satellite, a unique opportunity arose to study detailed PMC structure and temporal development through a coordinated campaign of airborne NLC observations with AIM overpasses. An aircraft flight experiment, equipped with low-cost optical cameras, to image NLCs was carried out in the summer of 2009 in the Canadian subarctic. Though CIPS was successful in observing prominent bands, the principle purpose of the airborne campaign was to observe all formations of NLCs previously observed through ground observation near the day-night terminator throughout the time duration of one orbital period of the AIM satellite.

At the cold mesopause temperatures where PMCs form (typically less than 140 K), microscopic ice crystals can nucleate and grow to observable sizes (typically 40 nm diameter, von Savigny et al., 2005, Karlsson and Rapp, 2006, Baumgarten et al., 2008), over periods of

several hours to a few days [Gadsden, 1981, Jensen and Thomas, 1988; Rapp and Thomas, 2006]. The AIM satellite, in a 600 km sun-synchronous orbit of 96^{O} inclination, takes PMC images with extensive polar coverage but can only observe a cloud region for a few minutes, returning 90 minutes later and 25 degrees displaced in longitude [Rusch et al., 2009]. CIPS images over the same geographical region from successive orbits spaced 90 minutes apart, have very often shown rapidly varying cloud structures. The airborne platform has the advantage in being able to capture the temporal extent of PMC development within the time span between successive satellite overpasses.

Though airborne observations incur larger errors in geolocation, higher costs, and shorter observation periods, they are attractive because the portability enables flexibility in observing. Aircraft observations are less influenced by the presence of tropospheric clouds and can provide an observational platform above a large percentage of absorbing/scattering elements in the atmosphere. Also, carefully pre-planned flight trajectories can lead to additional observing opportunities. One scenario is to fly on a trajectory that maintains a constant solar depression angle for extended periods of time to partly remove changing scattering conditions during sequential observations. In this manner, the constant solar depression angle (SDA) relative to the aircraft constrains viewing conditions while recognizing that the cloud dynamics can change during the sequence of photos. Another aspect is to intercept overflights of the AIM satellite to obtain common volume images with the cameras integral to the Cloud Imaging and Particle Size (CIPS) experiment onboard the AIM satellite. It is this latter aspect of the airborne campaign we will focus on in this discussion.

1.4.2 Employing integrative methods to understand the relative contribution of glacial sliding

As glaciers best represent the observable effects of climate change, an integrative methods approach was employed at Sermeq Avannarleq, a location well surveyed by radar, laser radar (LiDAR), imagery, and in-situ observations from airborne, space-based, and ground-based observational platforms. The study of volumetric trends of the Greenland Ice Sheet have long been a goal but the tools that would enable an accurate study of the ice sheet have only been in place throughout the preceding decade. Large uncertainty exists in any future projections of the evolution of the ice sheet resulting from a relative lack of knowledge of the positive feedbacks that could drive an accelerated disintegration. Such positive feedbacks include the enhanced meltwater effect, where enhanced surface melting causes water to penetrate to the bedrock and drive glacial sliding resulting from reduced basal friction [Zwally et al., 2002], and the development of force imbalances at the calving fronts due to thinning, which causes the glacier to be more buoyant through reduced frictional back forces, and causes the glacier to become more lubricated at the calving front [Thomas et al., 2003]. As both of these positive feedbacks are directly related to the net change in overall glacial sliding, a greater understanding of the role of glacial sliding will increase our understanding of the nature of these positive feedback loops.

The principle purpose of the glacial analysis is to determine the relative contribution of sliding in the ablation zone near Sermeq Avannarleq and in doing so, establish a method from which sliding ratios could be inferred at other outlet glaciers, thus establishing a framework for assessing one of the largest uncertainties of climate change studies. A secondary purpose of the glacial analysis is to identify where the greatest improvements can be made to observational and modeling techniques, which is enabled through the integration of a wide range of observations.

2. Background of key topics

Noctilucent clouds, shown in Figure 2.1, are the highest clouds in the Earth's atmosphere, residing at an altitude of approximately 83 km (50 miles) and observed slightly below the mesopause in the polar summertime. These clouds are also called Polar Mesospheric Clouds (PMCs) when observed from space and are of special interest as they are sensitive to both global climate change and to solar/terrestrial influences, i.e. the coupling between the heliosphere and the Earth's atmosphere. NLCs have also provided a basis to understand high-altitude, low-pressure clouds that may be present on other planets and have also been seen to be a risk driver of spacecraft missions. Notably, the Space Shuttle mission rules prohibit flight through observed NLCs, and missions to the International Space Station, confined to a 51.6 degree inclined orbit, reach latitudes where low-latitude NLCs may be present.

The first recorded sightings of NLCs were reported in 1885 at high latitudes and were recognizable because they were of such altitude as to still reflect sunlight after the sun had set, thus giving the appearance of glowing at night. [Backhouse, 1885, Leslie, 1885]. Observations of these clouds were never recorded before 1885, even in the clearly documented histories of indigenous Arctic cultures. Since these initial sightings, observations from the ground have recorded NLCs with increasing frequency and in increasing area and albedo. In addition, satellite observations over the past four decades have confirmed earlier observations by indicating that the presence of these clouds has been increasing in frequency and extending to lower latitudes. Since these clouds form on condensation nuclei through cold temperatures and the presence of water vapor, and since the presence of carbon dioxide has been observed to act as a cooling agent in the mesosphere, and since the presence of methane has been observed to

photo-disassociate in the mesosphere to form water vapor, the anthropogenic (man-made) causes of climatic change are believed to be directly related to the presence of NLCs [Thomas et al., 2003].

Figure 2.1: Noctilucent clouds

2.1 Observational Trends of Noctilucent Clouds

NLCs are mesospheric clouds generally observable between a latitude range of 50-65 degrees and visible to the naked eye during the hours of twilight when the observer and the lower atmosphere lie in the Earth‘s shadow, while the clouds themselves are still exposed to direct sunlight. Thus, there is a limited viewing opportunity corresponding to a range of solar depression angles between 6 and 12 degrees [Gadsden, 1998; Gadsden and Schröder, 1989; Baumgarten et al. 2009b], that occur within the latitude range of 50–65°. The strong forward scattering of sunlight from the ice particles characterize the extensive cloud layers observable within NLC structures [Witt, 1962; Grahn and Witt, 1971; Taylor et al., 1984]. The mesosphere is no longer illuminated south of 50°, due to the sun being more than 12° below the horizon (astronomical twilight). Conversely, the sky is too light north of 65° as the sun is less than 6° below the horizon (civil twilight). NLCs are so optically thin that they scatter less than 1 part in 1000 of light incident upon them, making them invisible to a ground observer against the residual brightness present during civil twilight. At the end of civil twilight the clouds become visible as sky brightness has decreased by a factor of several hundred. Here, the low angle of the sun below the horizon also allows the high altitudes at which the NLC reside to be in direct sunlight [Gadsden and Schroder, 1989].

NLC formations typically span large areas of the polar upper atmosphere, extending at times up to 4×10^7 km^2 for time periods lasting from several minutes to more than 5 hours. Dynamically they tend to migrate to the southwest at an average velocity of 40 m/s, though individual bands often move in different directions and at speeds differing from the NLC display

as a whole. NLCs are also highly polarized in the same sense as, but less sharply than, the twilight sky [Gadsden and Schroder, 1989].

2.1.1 Structure and color

Ground-based photographs of NLCs often exhibit distinct wave-like structures with alternate dark and bright bands spaced from 10–100 km. Larger scale structures are commonly described as 'bands' while smaller-scale features often occur orthogonal to the bands, with a spacing of 3–10 km and are commonly termed 'billows' (e.g. Witt, 1962; Fogle and Haurwitz, 1969; Fritts and Rastogi, 1985; Gadsden and Parviainen, 1995; Thomas, 1991). Hines (1960, 1968) first proposed that these structures seen in NLCs were the manifestation of internal gravity waves (GWs). Chandran et al [2009] have since classified these GW structures extensively in PMC images from the Cloud Imaging and Particle Size (CIPS) experiment onboard the AIM satellite. As such, GWs play an important role in the thermal structure of the polar MLT, and hence the structure and evolution of PMCs.

Each PMC is composed of different forms, of which there are four major groups, veil (Type I), bands (Type II), billows (Type III) and whirls (Type IV). There are further sub divisions of these four major classes. Generally NLCs are an electric blue color, but red, gold and white are not uncommon and are due in part to the angle of the sun below the horizon. The general blue coloring is caused by absorption of incident sunlight by ozone in the Chappuis bands which reside in the yellow portion of the spectra [Gadsden and Schroder, 1989]. The standard reference for description of cloud forms is the "International Noctilucent Cloud Observation Manual" (WMO 1970), which breaks down NLCs into five types:

TYPE I. VEILS (fig 2.2)

Veils are the simplest of NLC formations and are very tenuous with no well-defined structure, and are often present as a background for other categories or forms. They are somewhat like cirrus clouds of uncertain shape; however, occasionally they exhibit a faintly visible fibrous structure. They often flicker.

Figure 2.2: Type I NLC with veil structure

TYPE II. BANDS (fig 2.3)

Band formations are characterized by long streaks with diffuse edges (type IIa) or sharply defined edges (type IIb). They are sometimes hundreds of kilometers long and often occur in groups arranged roughly parallel to each other or interwoven at small angles (perhaps visible evidence of the gravity waves propagating through the region). Occasionally an isolated band is observed. Bands change very little with time and blurred bands with little movement are often the predominant structure in the noctilucent cloud field. When they do move, it is often in a direction and with a speed that is different than that of the display as a whole. Very closely spaced thin streaks, called serrations, are occasionally seen in the veil background. They look like a continuous cloud mass as serrations are separated by only a few kilometers.

Figure 2.3: Type II NLC structure with band structure

TYPE III. BILLOWS (fig 2.4)

Billow formations are characterized as groups of closely spaced short bands which sometime consist of straight and narrow, sharply outlined parallel short bands (type IIIa). Sometimes they exhibit a wave-like structure (type IIIb). The distance separating pairs of billows is about 10 km. Billows sometimes lie orthogonal to the long bands and their alignment usually differs noticeably in close portions of the sky. Unlike the long bands, billows may change form and arrangement or even appear and disappear within a few minutes.

Figure 2.4: Type III NLC structure with billow structure

TYPE IV. WHIRLS (fig 2.5)

Whirls of varying degrees of curvature are also observed in veils, bands, and billows; infrequently, complete rings with dark centers are formed. Whirls of small curvature are classified as type IVa while whirls having a single simple band or several bands are classified as type IVb. Larger scale whirls are classified as type IVc.

Figure 2.5: NLC Formation with whirl structure

TYPE V. AMORPHOUS (fig 2.6)

Amorphous formations are similar to veils in that they have no well-defined structure but they are brighter and more readily visible than the veil type NLC.

Figure 2.6: Complex NLC formation

2.1.2 Altitude

The visibilities of NLCs are due to their great altitude. Their altitudes have been accurately determined by ground based parallactic photography (e.g. Taylor et al., 2009), LiDAR observations (e.g. Thayer at al., 1995), and in-situ rocket measurements (e.g. Gumbel et al., 1998). The clouds reside at an altitude of 80-85 km with an average altitude of 83 km. This places the clouds just below the temperature minima of the mesopause which is approximately 150K (-123°C). It is theorized that the clouds nucleate at the mesopause over several hours during nucleation and growth and then descend by a few kilometers to the altitude at which they are observed [Gadsden and Parviainen, 1995].

2.1.3 Formation

A number of models have been constructed to model the microphysics involved with the evolution of NLC particles [e.g. Turco et al., 1982; Jensen and Thomas, 1988]. These models assume that nucleation occurs under the supersaturated conditions in the cold summer mesopause region, when the ambient temperature can drop to 135K. The particles grow through condensation of water vapor until sedimenting out of the supersaturated region. Sublimation of the particles once out of the supersaturated region, however, is slow compared to the fall speed of the particles so the particles retain their size over most of their downward trajectory, leading to an accumulation of particles near their peak particle size, generally around 50nm. NLCs are very stratified, possessing a thickness in the vertical of only 0.5 to 2.0 km. The visible band structures result from vertical waves that reach an amplitude of approximately 1.5 to 3.0 km. [Thomas, 1991].

The mechanisms of PMC formation are still highly contested. Some maintain that the ice crystals nucleate around terrestrial dust particles and there are even some hypotheses that suggest deposition of dust particles from libration clouds provide the nuclei upon which PMCs grow [Reid, 1997]. The Cosmic Dust Experiment (CDE) onboard the AIM satellite is an instrument designed to monitor the variability of the cosmic dust influx into Earth's mesosphere in order to address its role in the formation of PMCs, testing the viability that the nucleation particles may be of extraterrestrial origin. (SOURCE: aim.hamptonu.edu/instrmt/cde). Meteoric smoke has been detected just above the sulfate layer (~35 km) to ~85+ km by the Solar Occultation for Ice Experiment (SOFIE) onboard the AIM satellite. It is currently estimated that between 10 to 100 tons of meteoric material enter Earth's atmosphere per day, where about 70% of the incoming meteoroids ablate at altitudes between 70 and 110 km, [Hervig et al., 2009].

The mesosphere is extremely dry and cold so it is unusual that PMCs form at all. Nucleation occurs due to super-saturation in the mesosphere. This is possible due to the very low temperatures and pressures at and near the mesopause. Temperatures as low as 111K (-162 degrees C) have been measured just a few kilometers above a PMC. These temperatures are set by mixing in the atmosphere due to hemisphere to hemisphere circulation from the movement of upward cooling air in the summer polar regions and the downward, warming movement of air over the winter polar regions [Gadsden and Schroder, 1989]. These temperatures are further maintained or adjusted by the attenuation of upwardly propagating gravity waves (buoyancy waves).

Gravity waves also supply the water molecules from which PMCs form by upward diffusion from lower down in the atmosphere. Water vapor is also supplied by the photo-dissociation of methane molecules in the mesosphere by ultraviolet light. Even with these sources of water the levels of water in the mesosphere available for PMC formation are extremely low - a few water molecules are present for every million atmospheric molecules. Mixing ratios for water at 80 km have been estimated to be approximately 3ppm, explaining why PMCs have been observed to be very thin. Indeed, measurements have suggested the optical thicknesses of PMC layers to be in the region of 10^{-4} with cloud particle diameters in the range of 50nm. [Gadsden and Schroder, 1989].

It is generally believed that upper atmospheric water vapor is increasing because of increases in methane, leading to observable effects on NLC brightness, which has been recorded since 1885. At present, methane oxidization accounts for about one half of the total water content above the troposphere and it is believed that the increase in water vapor in the upper atmosphere from methane oxidization will continue and increase the brightness and occurance frequency of NLCs [Thomas et al., 1989]. The relationship between water vapor concentration and solar cycle is less determined. While relationships between the solar cycle and upper atmospheric temperature and humidity have been documented at low to middle latitudes (e.g. Remsburg et al., 2002; Marsh et al., 2003; Chandra et al., 1997), much less information is available for high latitudes, particularly in summer. As discussed in the review by Beig et al. (2003), the existing measurements are inconsistent.

2.2 Evolution of Remote Sensing Techniques for Noctilucent Clouds

Following the initial observations of NLCs in 1885, NLCs have been observed by a range of methods including ground-based photography including stereography and globally coordinated imagery campaigns. Data have also been obtained from space-borne methods through imagery and spectrometry as well as from in-situ methods using sounding rockets. Though aircraft flight crew and passengers have been encouraged to take and submit photographs, the campaign outlined in this study marks the first airborne campaign dedicated to the study of noctilucent clouds, demonstrating how aircraft can also be used to obtain critical information to complement the data obtained through the previous means.

2.2.1 History of In-Situ NLC Research using Sounding Rockets

The first successful sounding rocket flights were conducted in 1962 in northern Sweden and employed particle collectors that opened at altitudes between 75 and 98 km that revealed an abundance of particles at least 1000 times the size of particles that were detected following a flight that did not penetrate NLC formations. [Hemenway et al., 1964]. The experiment was attempted again in 1967 by Witt [1969], though his experiment failed to produce the abundance of detections as Hemenway's experiment. Early rocket experiments were also able to to measure airglow, nitric oxide ionization, and solar irradiance [Witt et al., 1971] and to show that a large percentage of collected particles contained elements of high atomic number (e.g. Hf, Ni, Co, and Ce) [Hemenway et al., 1964].

Several rocket launchings from Kiruna in 1982 during the Cold Arctic Mesopause Project (CAMP) proved that in summer mesopause, temperatures at high latitudes are as low as 110 K and demonstrate a graduated temperature profile [Philbrick et al., 1984]. In 1993, The NLC-93 rocket campaign at Esrange, Sweden investigated the vertical structure of a noctilucent cloud layer in-situ, showing little vertical variation of the population of NLC particles through the layer, though the lower part of the cloud was observed to have an increase in particle size and a decrease in particle density near the cloud base [Gumbel and Witt, 1998].

The MIDAS-DROPPS campaign was a rocket-borne campaign conducted in Norway in 1999 that synchronized rocket and ground-based observations to determine particle sizes through analysis of the scattering phase functions of NLC particles. Optical photometers were flown onboard two rocket payloads through different mesospheric conditions. Using Mie calculations, the NLC observed in the first flight was determined to have small particles ($r<20$nm) and the relatively stronger NLC observed in the second flight was dominated by particles in the size range of 40-50nm [Gumbel et al., 2001].

In 2007, a rocket-borne experiment was conducted to quantify the smoke number density and size distribution as a function of altitude as well as the fraction of charged particles of NLCs. This experiment showed how the size-dependent, altitude-dependent and charge-dependent detection efficiency can be determined for a given instrument design, related the measured particle population to the atmospheric particle population, and found that rocket-borne smoke detection with conventional detectors is largely limited to altitudes above 75 km. Further, they found that there is no general difference between neutral and charged particles for particle sizes

down to 1 nm and that the use of a Brownian motion model is mandatory to correctly describe the statistical motion near the Faraday cup detector in the rocket payload [Hedin et al, 2007].

A rocket-borne mass-analysis of charged aerosol particles in the NLC layer was performed on 3 August 2007 as the first of two "MASS" (Mesospheric Aerosol Sampling Spectrometer) rockets was launched from the Andøya Rocket Range into an NLC layer, verified by the ALOMAR LiDAR site, approximately 26 minutes after an AIM satellite overpass. The rocket carried an electrostatic mass analyzer for the charged fraction of the aerosol particles. The mass-analyzer detected both positively and negatively charged particles that exist in about equal numbers for the 1 – 2 nm size range where the largest particles (>3 nm) are mostly negatively charged and the 0.5 – 1 nm particles are mostly positive. The transition of the sign of charge from positive at the smaller sizes to negative at the larger sizes is proposed to have been caused by positive ions or cluster ions being the condensation nuclei and subsequent collection of electrons after growth to a radius of 1–2 nm [Robertson et al., 2009].

2.2.2 History of NLC Research using Space-based Remote Sensing Techniques

Satellite observations over nearly three decades have provided a consistent measure of PMC occurrence, latitudinal extent, and brightness and indicate that the presence of these clouds has been increasing in frequency and extending to lower latitudes [Shettle et al., 2009; Deland et al., 2006]. American and Soviet astronauts have observed the phenomenon from space as early as 1970 and subsequent observations have been made from spaceborne platforms such as the Halogen Occultation Experiment (HALOE) and the Student Nitric Oxide Explorer (SNOE) [Merkel et al, 2003]. The most comprehensive advances to the understanding of PMCs have come from spaceborne platforms such as the Orbiting Geophysical Observatory (OGO-6), the Solar Mesospheric Explorer (SME), and most recently the AIM satellite, described briefly below:

Orbiting Geophysical Observatory

The OGO-6 satellite was launched on 5 June 1969 into a low polar orbit as the sixth of the OGO series of satellites tasked to study the Earth's magnetosphere. OGO-6 carried onboard visible airglow photometers that first scanned the atmospheric horizon throughout the summer polar mesospause region and was the first to trace the motions of PMCs across the polar cap [Donahue et al., 1972].

Solar Mesospheric Explorer

The general seasonal characteristics of PMCs were observed continuously from the Solar Mesospheric Explorer (SME) satellite over the time period 1981 to 1986. On board SME was an ultraviolet spectrometer, which mapped the distributions of PMCs and measured the altitude profile of scattering from clouds at two spectral channels of 265 nm and 296 nm [Thomas and MacKay, 1985].

Student Nitric Oxide Explorer

The Student Nitric Oxide Explorer (SNOE), a 254lb spacecraft built by the Laboratory for Atmospheric and Space Physics (LASP), carried three instruments: an ultraviolet spectrometer to measure nitric oxide altitude profiles in the terrestrial lower thermosphere (100-200 km altitude), a two-channel auroral photometer to measure auroral emissions beneath the spacecraft, and a five-channel solar soft X-ray photometer. In addition to its primary Mission Objective, SNOE successfully observed PMCs globally each day through seven PMC seasons and produced the first observations of 5-day period variations in PMC albedo [Merkel et al., 2003].

Aeronomy of Ice in the Mesosphere:

The AIM Satellite, launched in April 2007, is the first satellite to image PMCs. It has aboard it three payloads. The CIPS instrument provides a 2-D panoramic look at PMCs by collecting 360 degrees of multiple images. CIPS is supplemented by the Solar Occultation for Ice

Experiment (SOFIE), that measures the variability of cloud particles with respect to their altitude and their chemical composition, and the CDE, that records the amount of space dust entering Earth's atmosphere in order to assess whether space dust provides the foundation for the cloud condensation nuclei in the formation of NLCs. Early data acquired in 2007 indicate that PMCs form early in the spring season at high polar latitudes and travel down to lower latitudes--where they can be seen sweeping Europe and scattering over North America--as the spring and summer PMC season progresses. The Northern Hemisphere PMC season is mid-May to mid-August, the Southern Hemisphere PMC season is the southern spring and summer that falls between mid-November and mid-March [Russell et al, 2009]. It is the data from the CIPS imager that are used in this study.

2.3 The Greenland Ice Sheet

The Greenland Ice Sheet covers 1,710,000 square kilometers is the second largest ice body in the world, next to the Antarctic Ice Sheet. It has experienced record melting in recent years and is likely to contribute substantially to sea level rise as well as to possible changes in ocean circulation in the future [Meese et al., 1997]. Current climate models predict an overall temperature increase of 3 °C (5.4 °F) by 2100. The volume of ice, if melted, would correspond to a global sea level rise of 7.2 m (23.6 ft), which would inundate virtually every coastal city in the world [Zemp et al, 2001].

The mass balance of glaciers is considered a key proxy to changing climate conditions. The 2001 report from the International Panel on Climate Change (IPCC) indicates a loss of 50 to 100 Gt/yr for the years spanning 1993 to 2003 and loss at even higher rates between the years 2003 and 2005. Current estimates of the overall mass balance of the Greenland Ice Sheet vary,

though all indicate an acceleration of ice disintegration throughout the last several decades [Houghton et al., 2001]. Additionally, multiple positive feedbacks could lead to nonlinear ice sheet disintegration much faster than claimed by the IPCC. Such positive feedbacks include the enhanced meltwater effect, where enhanced surface melting causes water to penetrate to the bedrock and drive glacial sliding resulting from reduced basal friction [Zwally et al., 2002]. A second positive feedback is caused by a force imbalance at the calving front due to thinning, which causes the glacier to be more buoyant through reduced frictional back forces, and causes the glacier to become more lubricated at the calving front [Thomas et al., 2003]. Additionally, the loss of the reflective ice sheet causes an increase of the Earth's net albedo that drives overall radiative absorption [Das et al., 2008]. It is the trend of the mass balance combined with analysis of these positive feedback loops that support current projections of the mass of the Greenland Ice Sheet. As two of the three positive feedback loops result in a change of overall sliding, it is clear that a greater knowledge of the contribution of sliding to glacial dynamics will contribute to a greater understanding of the nature of these positive feedback loops.

2.3.1 Sermeq Avannarleq

Sermeq Avannarleq is a marine terminating outlet glacier located in Western Greenland just north of the town of Ilulissat and Jacobshavn Isbrae, the outlet glacier responsible for up to 7% of the total mass loss of the Greenland Ice Sheet. Sermeq Avannarleq had been quite stable for much of the last century and has only recently begun to show signs of glacial retreat.

Figure 2.7: Sermeq Avanarleq terminus

Sermeq Avannarleq was chosen as a focus of analysis in this study because it is beginning to demonstrate glacial retreat as well a change in the surface velocity profile of the surrounding ice. Also, due to the elevated interest in the study of Jacobshavn Isbrae, much data has been obtained on the glacial ice around Sermeq Avanarleq due to its proximity. The flowlines that feed Sermeq Avannarleq have extensive ground penetrating radar data, photographic data, and airborne LiDAR data from Operation Ice Bridge overpasses as well as an adequate amount of in-situ data from a series of weather and ice core stations in the vicinity.

2.4 Evolution of Remote Sensing Techniques applied to the Greenland Ice Sheet

The Greenland Ice Sheet has been studied through a variety of ways including ground-based, airborne, and space-based observations. Ground-based observations have been performed through the use of imagery (e.g. time lapse photography) and ground based meteorological sensors. Spaceborne observations have included surface elevation data from spaceborne LiDAR (e.g. ICESat) [Krabill et al., 2002], RADAR altimetry (e.g. ERS-1) [Bamber et al., 1998], surface velocity data from space-based synthetic aperture RADAR (e.g. RADARSAT-1) [Joughin et al., 2010], space-based imagery (e.g. SPOT, www.spotimage.com), and mass changes inferred from changes in the gravitational field as derived from satellite gravimetry (e.g. GRACE, http://www.csr.utexas.edu/grace/). Airborne observations, such as those currently onboard the aircraft being used in support of NASA's Operation Ice Bridge, have provided surface imagery, surface elevation data using airborne scanning LiDAR and radar altimetry, sub-glacial water concentration from use of gravimeters, and intra-glacial and bedrock data provided by ground penetrating radar systems. It is a synthesis of space-based InSAR and altimetry data, as well as the data from the airborne observations integral to Operation Ice Bridge, that are used in this study.

3. Selection and application of remote sensing techniques applied to the day-night terminator of noctilucent clouds

PMCs are the central focus of the NASA small explorer mission, Aeronomy of Ice in the Mesosphere (AIM). Russell et al. [2009] gives an overview of the AIM satellite, its mission and goals. With the successful AIM launch in April 2007, a unique opportunity arose to study detailed PMC structure and temporal development through a coordinated campaign of airborne NLC observations with AIM overpasses.

Noctilucent clouds are large heterogeneous phenomena that can effectively be observed through various remote sensing techniques, and the synthesis of these techniques can provide unique insight into the nature of the phenomena. As spacecraft clearly provide the best platform to obtain global-scale remote sensed data, the nature of orbital motion, the relative distance from observed phenomena, and the effects of the atmosphere all leave gaps in critical information that are better provided through airborne or ground-based observations.

Airborne remote sensing techniques provide an essential mix of spatial coverage and detail. In contrast to spaceborne platforms, aircraft flight trajectories can be engineered to provide more comprehensive temporal coverage or concentrate observations upon specific details of interest. The airborne platform thus has the advantage of being able to capture the temporal extent of PMC development within the time span between successive satellite overpasses, displaced in time by approximately 90 minutes and in space by 25 degrees of longitude [Rusch et al., 2009]. CIPS images over the same geographical region from successive orbits have often shown rapidly varying cloud structures. Furthermore, the non-recurring costs of an airborne flight campaign are orders of magnitude less than that of a spacecraft campaign.

Ground-based observations are a low-cost way to obtain in-situ observations of terrestrial phenomena and a steady platform from which to observe atmospheric phenomena. This study shows that there exist complementary aspects of space-based, airborne, and ground-based observations that enable large heterogeneous climatological phenomena to be studied and that coordinated observations of spaceborne, airborne, and ground-based observations can be effectively conducted.

3.1 Integrative methods applied to noctilucent clouds

This study hopes to further the understanding of noctilucent clouds by meeting three objectives: 1) validation of CIPS Processing Algorithm, 2) improved determination of the temporal evolution of NLCs, and 3) the simultaneous observations of NLCs to determine the sensitivities of CIPS and the commonality of the mutually observed features. To these objectives, various remote sensing methods were used including imagery from the CIPS imager onboard the AIM spacecraft, airborne imagery, and ground-based observations.

Existing observations from spacecraft produce data that is bounded in low latitudes by the detection threshold of the spacecraft sensors. We understand from ground-based observations (e.g. Taylor et al, 2009) that the low latitude threshold of noctilucent clouds may be observed to much lower latitudes, though ground-based observations are bounded in high latitudes by the increased background from light being scattered from the atmosphere at lower altitudes below the NLC layer. Further, previous observations from space-based platforms and ground-based observations indicate a gap of about one-degree of latitude where no NLCs are

observed [personal conversation with Taylor, M]. To obtain a synchronized observation, it is therefore necessary to be able to position a low-elevation observation near the groundtrack that the satellite is expected to overpass at an altitude that allows observations to higher latitudes. A camera, sensitive to the visible spectrum and mounted to an airborne platform, was selected for this purpose. Data provided by the CIPS imager on the AIM satellite was chosen as it provided low-latitude global coverage from a space-based platform. On the summer solstice, the day-night terminator is at the lowest latitude and synchronized observations can be observed at these low latitudes. After the solstice, this band of latitude where synchronized observations may be made migrates northward.

3.2 Space-based imagery

Spaceborne imagery has been obtained in a wide range of wavelengths from a variety of spacecraft in varying orbits. Noctilucent clouds are generally imaged in the UV spectra so that the ozone, having a concentration that peaks in the upper stratosphere, may be used as a background. At ultraviolet wavelengths, the albedo of the Earth is very small so that particulate (Mie) scattering observed above the altitude of the background can then assumed to be associated with noctilucent clouds [McClintock et al., 2008]. In the noctilucent cloud analysis detailed here, spaceborne imagery was obtained from the CIPS imager aboard the AIM satellite. Prior to the AIM satellite, PMC observations from spacecraft have been obtained using payloads dedicated to other scientific objectives. CIPS was selected to provide spaceborne data as it is the only payload dedicated to the observations of PMCs and has improved detection threshold and resolution than prior space-based experiments. More significant is the fact that the AIM satellite is currently operational, enabling synchronous observations with the airborne platform.

CIPS is a four-camera, near-nadir ultraviolet (UV) imager flying on the AIM satellite. AIM was launched on April 25, 2007 into a 600 km, sun-synchronous orbit with a noon/midnight equator crossing time. The goals of the CIPS instrument are described by Rusch et al. [2009] and the details of the instrument design and its implementation on AIM are described by McClintock et al. [2009]. Benze et al. [2009] describe initial validation of the CIPS albedo measurements. CIPS provides wide-angle UV images of the atmosphere over a broad range of scattering angles in order to determine the presence of PMCs, measure their spatial morphology, and constrain the parameters of cloud particle size distribution. The four identical CIPS cameras have a 15 nm passband centered at 265 nm, the wavelength chosen to maximize PMC contrast due to the relative weakness of the Rayleigh-scattered sky background caused by the absorption of solar radiation in the ozone Hartley bands, and are oriented near-nadir in a configuration that allows partial overlap between cameras. Each camera uses a detector with 2048 x 2048 pixels that is electronically binned in 4x8 combinations to generate a 340 (along-orbit track) x 170 (cross-orbit track) array of science pixels. Simultaneous Level 1A images from the four cameras are merged and binned to form a single display called a scene, which has a combined field-of-view (FOV) of 120 degrees along-track by 80 degrees cross-track (approximately 2000 by 1000 km when projected to PMC cloud altitude). This merged Level 1B data is mapped to a uniform spatial grid with a resolution of 25 km^2 per pixel. The large CIPS FOV, combined with a temporal sampling rate of 43 seconds between scenes, results in a significant overlap between adjacent scenes, so that a PMC in the FOV is viewed seven times at a large range of scattering angles (typically from approximately 30° to 170°) as the satellite moves along the orbit. These multiple observations at each location facilitate the removal of the

Rayleigh scattered background. Rusch et al. (2009) describe the variation of scattering angle and albedo across a CIPS image.

3.3 Airborne Imagery

Airborne photography was obtained in both the noctilucent cloud study as well as the Operation Ice Bridge campaigns, though the imagers used on the Ice Bridge campaigns were used only as a means to validate the LiDAR observations. The imagers used in both campaigns were very similar.

The noctilucent cloud experiment relied upon a single Canon EOS30D camera coupled to a 30mm focal length Sigma lens, producing images of a horizontal FOV of 41.1^{O} and vertical FOV of 28.1^{O} through a 3504 x 2336 CCD. The Canon EOS30D camera was chosen for its high resolution, proven history for NLC imagery, ease of interface with automated computer control and data acquisition, and low cost. When coupled with a Samsung Q1 tablet computer and a solid state hard drive, this camera proved to be a reliable system for the airborne photography of NLCs. The camera was rigidly mounted and set to an F-stop of f/1.4, 1/10s exposure time, and an ISO 400 speed. The focus of the camera lens was set to infinity and the autofocus was disengaged. The integration time was chosen experimentally as to maximize contrast while minimizing effects of jitter produced by the airborne platform. As scattered light from NLCs and background molecules is polarized [Witt, 1960], a Schneider linear polarizer was paired to the lens to improve overall image contrast.

The University of Colorado NLC Imager is shown in Figure 3.1 along with the schematic showing the imager integration with the flight computer and the external power sources. The imager mount is designed to adjust and fix upon an established elevation angle but rotate in azimuth so that all imagers can track the solar beta angle simultaneously. The imager is based on two Canon EOS-30D cameras connected to an external power source and mated with Sigma 30mm lenses and Schneider polarizers. The imagers were connected to a tablet computer with a solid-state hard drive via USB ports. An onboard GPS receiver (AVMAP EKP-IV) was used to record image time, longitude, and latitude.

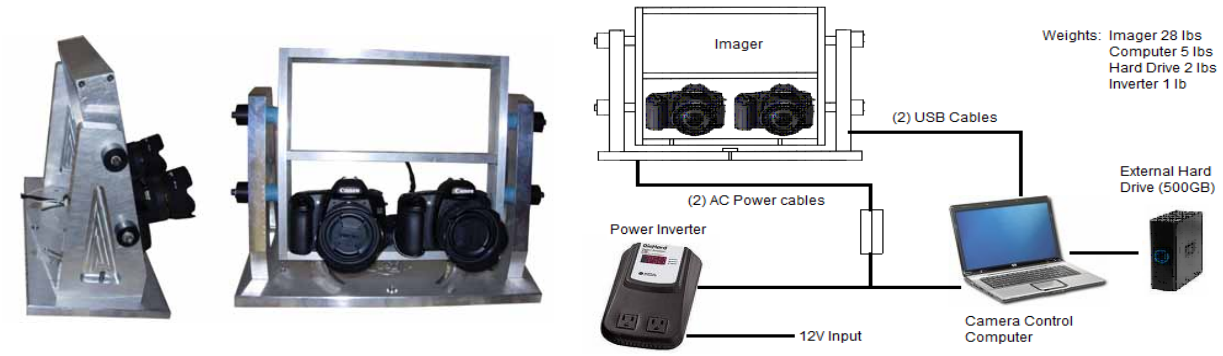

Figure 3.1: University of Colorado NLC imager and integration schematic

A 1979 Mooney M20K aircraft, registered under N231TF (Figure 3.2), was selected to conduct mission operations. This aircraft was chosen to meet mission design requirements of high cruising altitude, relatively fast cruising speed, and low operations cost. The aircraft was modified with extended range fuel tanks and the rear seat was removed to accommodate a table onto which the instrumentation was mounted. Key performance measures of N231TF are:

Horsepower: 210

Weight: Gross: 2900 lbs, Empty: 1800 lbs

Speed: Cruise: 191 kts, Max: 201 kts, Stall (dirty): 57 kts

Endurance: Fuel Capacity: 108 gal, Consumption: 12.5 gal/hr avg.

Service Ceiling: 25000 ft MSL

Figure 3.2: Mooney research aircraft N231TF

3.4 Ground Based Imagery

In visible wavelengths, NLCs scatter light more efficiently in the forward-scattering direction, which is the direction most germane to synchronous imagery with ground-based images. Ground imagery of NLCs have been consistently performed and cataloged from northward-observing ground sites since their initial observations. Critical data to the planning of the NLC experiment of this study were obtained through a coordinated ground observation campaign in Alaska during the Summer of 2007. It has been determined through repeated ground observations that NLCs are visible from range of SDA from 6 to 16 degrees [Gadsden and Schroder, 1989], and these results were confirmed by a 2007 ground observation campaign where common volume mesospheric measurements were made over central Alaska on 10–11 August 2007 using the Poker Flat Incoherent Scatter Radar (PFISR), a co-located Rayleigh lidar, and remote, two-station digital image observations, enabling the first detailed investigation of the horizontal and vertical structures of NLC and Polar Mesospheric Summertime Echoes (PMSE). Coincident measurements were also made of an unusual NLC display recorded that night, characterized by a broad luminous band that contained several prominent wave forms [Taylor at al., 2009].

4. Synchronized imagery of noctilucent clouds at the day-night terminator: Method

An aircraft flight experiment, equipped with low-cost optical cameras, was carried out in the summer of 2009 in the Canadian subarctic to intercept overflights of the AIM satellite and obtain common volume images with the CIPS cameras. This section describes the method through which the preliminary test flights, campaign mission planning, mission operations, and post-campaign data analysis was conducted.

4.1 Defining Jitter and Camera Settings

A flight test to characterize the effects of jitter and to optimize camera settings was conducted with the Mooney M20K research aircraft, which departed Front Range Airport (KFTG) and flew to a location approximately 20nmi NE of the Denver Very-High Frequency Omnidirectional Range (VOR) navigational facility. Flight crew consisted of Jason Reimuller and Bruce Hulley. Aircraft loitered at 12,000' MSL for 20 minutes under Visual Meteorological Conditions (VMC) and lighting conditions that spanned solar depression angles of 6 degrees through 14 degrees. During this time, a single Canon EOS 30D SLR Camera with Sigma 30mm Lens was set to take repeating images every 5 seconds. Aircraft then proceeded on a western heading for 10 minutes to take calibration imagery of star patterns before arriving at Erie Municipal Airport (KEIK). The camera had the following settings:

Setting:	Aperture Priority
Shutter Integration Time:	between 1/25s and 5 sec.
ISO:	800
F Stop:	f/1.6
Focal Length:	30mm

4.2 Campaign Planning

Campaign mission operations were conducted in a latitude band confined by the limits of CIPS sensitivity to low latitudes and the signal-to-noise ratio between the cloud scattering and the background scattering of the aircraft images. Previous CIPS images confirm that the instrument was sensitive to PMC cloud formations as low as 63 degrees latitude, as shown in Figures 4.1a and 4.1b. These images confirmed that CIPS was sensitive to five degrees below the local terminator.

a) b)

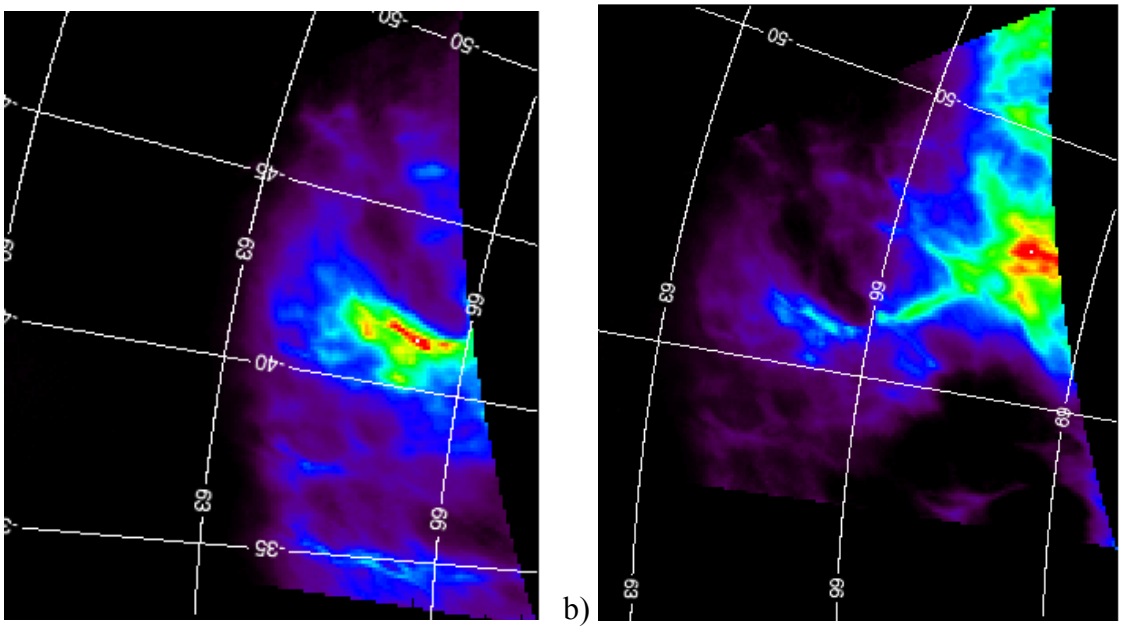

Figures 4.1: Level 1c (Rayleigh removed) CIPS Image of Orbit 1196. Sequential images of 43 second time difference**.** Terminator at 68.4 degrees Latitude.

Prior ground campaigns confirm that ground-based imagers can detect NLCs in periods when the SDA is between 6 and 16 degrees [Gadsen and Schroeder 1989]. It was calculated that the effects of the planned cruise altitude added approximately 1.2 degrees to this range as a result of the heightened 'dip' of the horizon from the higher altitude. The SDA of 8.5 was chosen to balance a desire to 1) see into the region of previously confirmed CIPS sensitivity, 2) be in a range sensitive to previously confirmed ground observations, and 3) fly with enough ambient lighting to detect the presence of towering altocumulus clouds.

High Level Airport (CYOJ) was chosen as the primary base of operations due to its near ideal latitude and the fact that the terrain is relatively flat in the surrounding areas. This is important both for obtaining clearer imagery at low elevations and also as a risk mitigation measure as sorties were flown at night in a single engine aircraft. Rainbow Lake, Alberta (CYOP) and Fort Nelson, BC (CYYE) airports are situated west of High Level and were chosen as contingency refueling locations. The elevation of High Level airport is 325 M (1,066.3 FT). Fort Smith, NWT (CYSM) and Watson Lake, YT (CYQH) airports were also selected as a possible airport in the event the campaign was extended and operations needed to migrate north to compensate for the decreasing post-solstice solar declination.

Airport	ID	Location	Runway	ILS
High Level, AB	CYOJ	58.37N, 117.15W	5000’ Asphalt	Yes
Rainbow Lake, AB	CYOP	58.29N, 119.24W	4500’ Asphalt	Yes
Fort Nelson, BC	CYYE	58.80N, 122.47W	6400’ Asphalt	Yes
Fort Smith, NWT	CYSM	60.01N, 111.53W`	6000’ Asphalt	No
Watson Lake, YT	CYQH	60.07N, 128.80W	5500’ Asphalt	No

Table 4.1: Campaign Airstrips

4.3 Validation of CIPS Algorithm

At the time of the campaign, CIPS imagery was being processed by version 3 algorithms. The imagery obtained in the campaign was focused on low latitude regions where the CIPS thresholds are the weakest. The next version of the CIPS processing algorithm, version 4.1, was designed to better remove the background of the imagery. Since low latitudes are the most sensitive to background noise, an increase in SNR would permit an improved ability to image clouds to lower latitudes. Thus, a main objective of the synchronized imagery is to better validate the CIPS images by verifying the cloud formations perceived by both imagers (aircraft and CIPS) are similar. The aircraft images can then be better applied in validating subsequent revisions of the CIPS processing algorithm in low latitude regions.

4.4 Synchronized Observations of NLCs

Though practical matters of aircraft operations, performance, and the limited presence of NLCs impacted the scope of the 2009 summer airborne campaign, a synchronized observation of a NLC by the airborne platform and PMC by the CIPS instrument on the AIM satellite was recorded on 6 July 2009 at 06:49:24 UT from an altitude of 18000 ft (5486m). The coordinated observations enabled investigation of CIPS performance at the day-to-night terminator and made it possible to relate the different resolutions of the two types of imagery to identify PMC features.

Figure 4.2 illustrates the geometry of this problem as applied to the CIPS imager and the aircraft positioned at a SDA of 8.5 degrees and a flight altitude of 5486 m. The geometry shown

is independent of solar declination, though the solar declination of the July 6, 2009 overpass was 22.7 degrees. The red arc shows the range of latitudes through which CIPS has identified PMC features with a spatial resolution of 5km x 5 km. CIPS is theoretically sensitive poleward of a latitude approximately 5.8 degrees (~1088 km) south of the terminator as depicted by the red curved line, if an ozone background height of 48 km is assumed. Though previous versions of CIPS retrieval algorithms limited PMC observations to latitudes poleward of approximately 68 degrees, current retrieval algorithms (e.g. v4.20) have been found to detect PMCs, on an individual basis, to latitudes of about five degrees south of the terminator. In this particular overpass, PMC features were observed in areas extending to about 5.1 degrees of latitude south of the terminator. The aircraft, supporting an imager at an altitude of 5486 m (Flight Level 180), is theoretically sensitive to a range spanning from a latitude 7.6 degrees south of the terminator to a latitude 4.3 degrees north of the terminator as shown by the light blue line, neglecting atmospheric diffraction effects. NLC features, however, were only detected to a latitude 4.0 degrees south of the terminator, as denoted by the thick blue line. Areas north of this threshold have residual Rayleigh-scattered sunlight that produces too much background to effectively detect NLCs. Thus, we see that a zonal range of approximately 1.1 degrees of latitude (~122 km) shows features observable from both platforms.

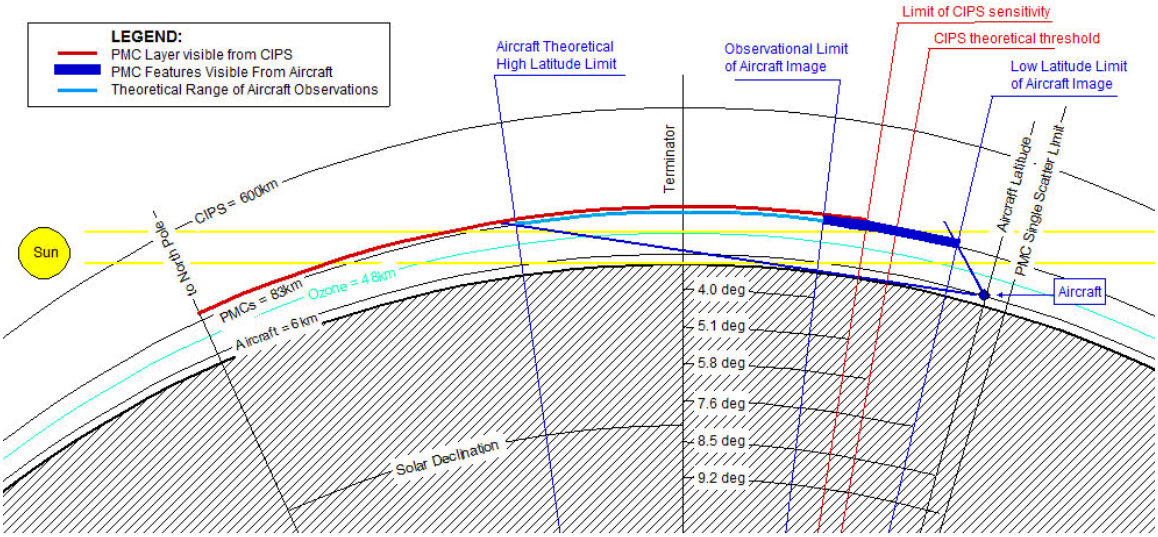

Figure 4.2: CIPS and aircraft imagery sensitivity. The blue arc indicates projection of aircraft imager upon cloud base and the red arc indicates projection of the CIPS image upon the cloud tops.

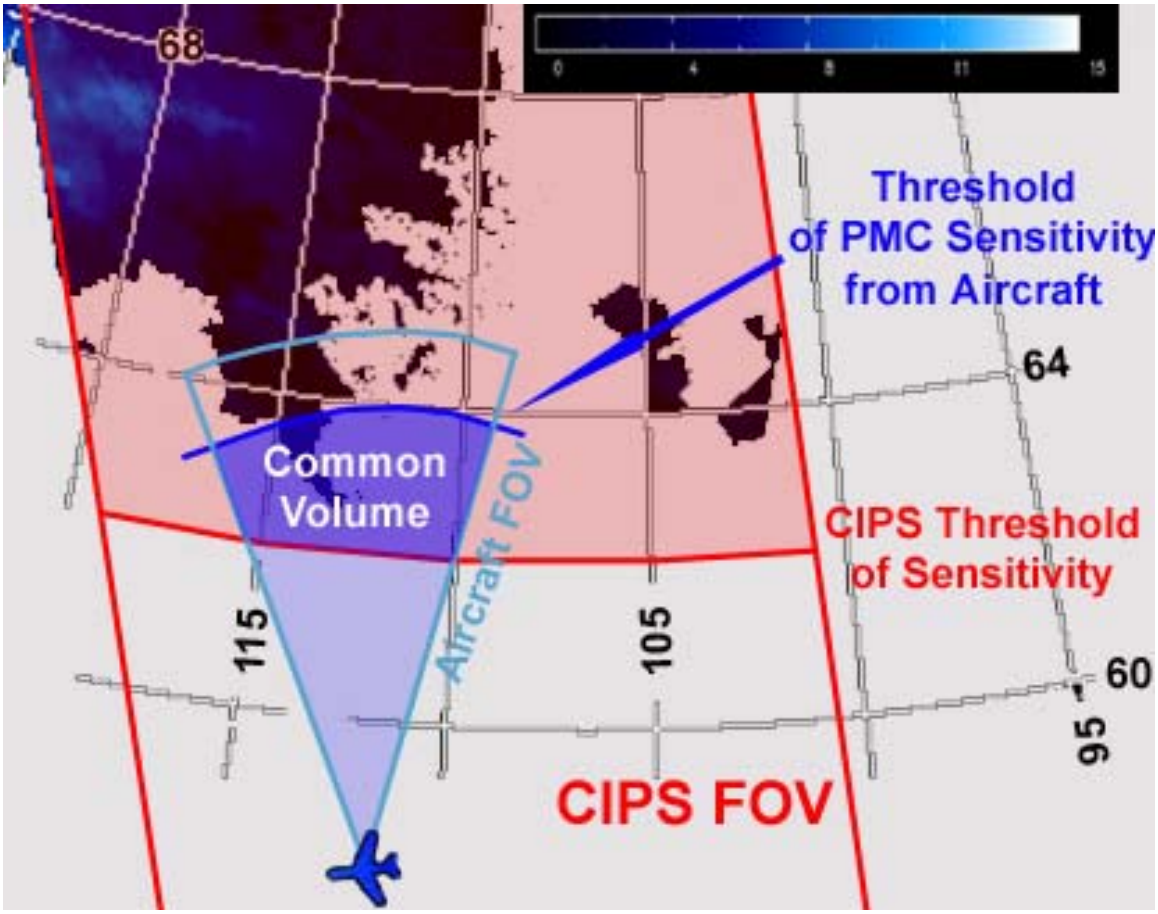

Figure 4.3: Overlay of CIPS and aircraft FOV. The color table gives the PMC albedo values x 10-6 sr-1

The relationship between the FOV and the threshold sensitivities of both the CIPS camera and the aircraft camera is shown in Figure 4.5. The CIPS FOV across the orbit track is approximately 1000 km [Rusch et al., 2009] and the sensitivity is constrained by the UV terminator, identifying PMC features north of approximately 62.3^{O}N latitude. On the other hand, the aircraft camera is constrained by the background illumination of higher latitudes and can discriminate NLC features south of approximately 63.5^{O}N latitude.

Four flights were conducted in July 2009, though only during the flight of 6 July were NLCs detected. However, this flight was successful in intercepting the AIM satellite at 06:49:24 UT and then proceeded to obtain 1.5 hours of observation data maintaining a constant SDA of 8.5 degrees while flying along a parabolic trajectory at 165 knots, as shown in Figure 4.6. This parabolic trajectory sought to address the additional objective of the campaign of investigating the temporal evolution of NLCs, though this discussion focuses exclusively upon the common volume result. The value for SDA was chosen based on a history of ground-based NLC observations, corrected for altitude, and the operational desire to fly far enough North to maintain enough ambient lighting to discriminate altocumulus clouds, which could pose an icing risk for the aircraft. An altitude of 5486 m was chosen in order to get above the majority of scattering species in the lower atmosphere and optimize aircraft cruise performance. Results from this flight also showed unanticipated effects of jitter and off-optimized focus, which were addressed by modifying the camera mount, adjusting the integration time to 1/15s, and recalibrating the focus and polarizer positioning.

Airborne imagery complements satellite imagery by providing focused areas of significantly enhanced spatial resolution. The CIPS imagery is of significantly reduced resolution compared to aircraft imagery though band structures and other features are clearly identifiable. The spatial resolution for the CIPS science pixels is 1-2 km in the nadir, increasing to 5 km near the edge of the fore and aft camera fields. In contrast, the spatial resolution of the airborne cameras when projected onto the NLC cloud base is highly dependent upon elevation. Pixels projected to an NLC base vary from 75 x 75 m near the high elevation (low latitude) threshold to approximately 700 x 700 m near the horizon, where identifiable band and billow structures were observable to a distance approximately 500 km north of the aircraft. On average, the aircraft, when equipped with a Canon EOS-30D camera, can provide an 8 to 50X improvement in spatial resolution.

4.5 Temporal Evolution of NLCs

An aircraft is able to track a prominent cloud that is detected by the AIM spacecraft, a capability that does not exist with ground-based or space-based imagery, and produce imagery of the PMCs lifespan, from formation to dissipation. In this campaign a carefully planned flight plan was developed to offset the apparent solar motion so that the imager would be able to receive a near-constant signal to noise ratio throughout the imaging period. This is a capability that is not available when using ground-based observation methods. Figure 4.4 illustrates the mission plan that was executed during the sortie of July 6, 2009. Nodes 1-11 were established so that the sun was forced into a constant depression angle where the northern component of the velocity vector balances the sun's increasing depression angle before local midnight and the southern component of the westernmost nodes compensate for the sun's decreasing depression

angle after local midnight. The flight profile assumes a cruise speed of 165 kts, adjusted for the winds aloft forecast obtained before each sortie was flown. The parabola of nodes maintains roughly the same form for all sorties planned through the campaign, though the latitudes increase exponentially as more days elapse from the summer solstice.

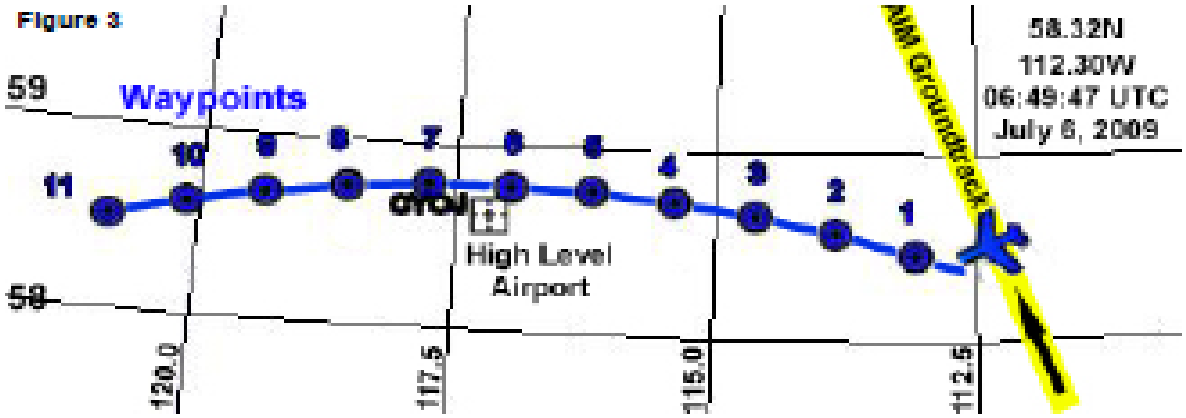

Figure 4.4: Flight trajectory for 6 July 2009. The AIM groundtrack was intercepted at 06:49:47 UTC, July 6, 2009. Waypoints 1-11 were subsequently flown to maintain a constant solar depression angle while observing NLC temporal evolution.

4.6 Image Processing and Analysis

The data retrieved from the CIPS imager was processed using the version 4.1 algorithm, which geolocates the pixels and removes the Rayleigh background. Bailey et al. [2009] describe the CIPS Version 3 technique for removing the Rayleigh background and determining mode radii of the PMC ice particle distributions. In Version 3, the Rayleigh background was isolated from the PMC radiance at each location using the six or more observations at that location. Absorption by atmospheric ozone modulates the observed Rayleigh brightness, and must be taken into account in the retrieval algorithm. Although the version 3 retrieval handles this on a pixel by pixel basis, the ozone column abundance can be constrained by taking advantage of the fact that it does not change significantly over small intervals of solar zenith angle (the primary spatial parameter controlling the Rayleigh brightness). Thus, a new version of the CIPS algorithms has been developed which solves for PMC parameters at each CIPS pixel and Rayleigh parameters over regions with similar solar zenith angles. This has resulted in significant improvements in the separation of Rayleigh scattering from the PMC scattering. A comprehensive evaluation of the new retrievals is in preparation, but it is this version of the CIPS data processing, Version 4.1, that is used in the present work.

The lower latitudinal boundary for cloud detection in the high solar zenith angle (near terminator) portion of the orbit is determined by the solar zenith angle at which the cloud deck is no longer illuminated by incoming UV radiation. As the sun sets below the horizon, the solar UV rays pass through increasingly larger columns of ozone to reach the cloud deck. Eventually, the ozone optical depth along this path is large enough to prohibit any UV illumination of the clouds. Assuming a cloud deck altitude of 83 km and a nominal ozone profile, this occurs at a solar

zenith angle of ~94°, which corresponds to a latitude of ~63°N for the AIM orbit used in this study. In general, the cut-off solar zenith angle depends on the local ozone conditions and no clouds are detected past 95°. Note that this only pertains to observations on the night side of the orbit, which are of interest for this study; the low-latitude limit for CIPS PMC observations on the sunlit side of the orbit is in theory defined only by the latitude at which the PMC brightness does not rise significantly above the background.

The aircraft image was geolocated by ray-tracing as described in Baumgarten et al., 2009b. A comparative analysis was then performed on the locations, orientations, and wavelengths of the observed features. The geolocation of the airborne image was performed given knowledge of the aircraft position and altitude, image time, the FOV of the camera CCD in both vertical and horizontal axes, and the elevation and azimuth of the camera. After geolocation, Rayleigh removal was performed by subtracting a sixth-order polynomial averaging through all rows and all columns. The aircraft position has error +/- 0.01^{o} of longitude and latitude (1.1 km) and the altitude has error of +/- 100 ft (30 m). The aircraft altitude error, combined with an error of 1000 ft (305 m) that is associated with the assumption that cloud tops at the horizon are at the same altitude as cloud top heights estimated by the flight crew during ascent, contribute to the elevation error, which sums to +/- 0.07^{o}. Camera FOV was tested in order to validate the published specifications and error associated with FOV is not considered. The most significant source of error is the azimuth, which relies upon the compass heading recorded by the flight crew, compensated for the estimate of magnetic declination at the observation point. Azimuth error is inclusive of both compass error and pilot error and is estimated to be +/- 5^{o}.

5. Synchronized imagery of noctilucent clouds at the day-night terminator: Results and Sensitivity Analysis

Results from the vibrational analysis and camera setting flight test as well as the results supporting the mission objectives of the flight campaign are detailed in the sections that follow.

5.1 Defining Jitter and Camera Settings

The results of the initial calibration flight tests are summarized in Table 5.1:

Variable	Value
aircraft motion effect on pixel resolution	No effect less than 1/10s shutter speed
Aircraft roll/yaw effect on ground/sky ratio	+/- 3.35% variation
Engine vibration frequency	35Hz
Engine RPM setting	2100 RPM

Table 5.1: Vibrational analysis flight test results

From the star calibration imagery, aircraft motion (roll, yaw) in steady air was found to not affect the pixel resolution for exposure times less than 1/10 sec, which is larger than we are currently using. The amplitude of engine vibrations show about a three pixel-width variation in vertical FOV. To compensate with shutter speed, we would need about 1/70s, or an ISO of at least 4800. Figure 5.1 shows the track of Venus under a time exposure of 4.0s in twilight conditions. The illustration shows a periodicity of 35Hz, which is equivalent to the engine RPM setting of 2100.

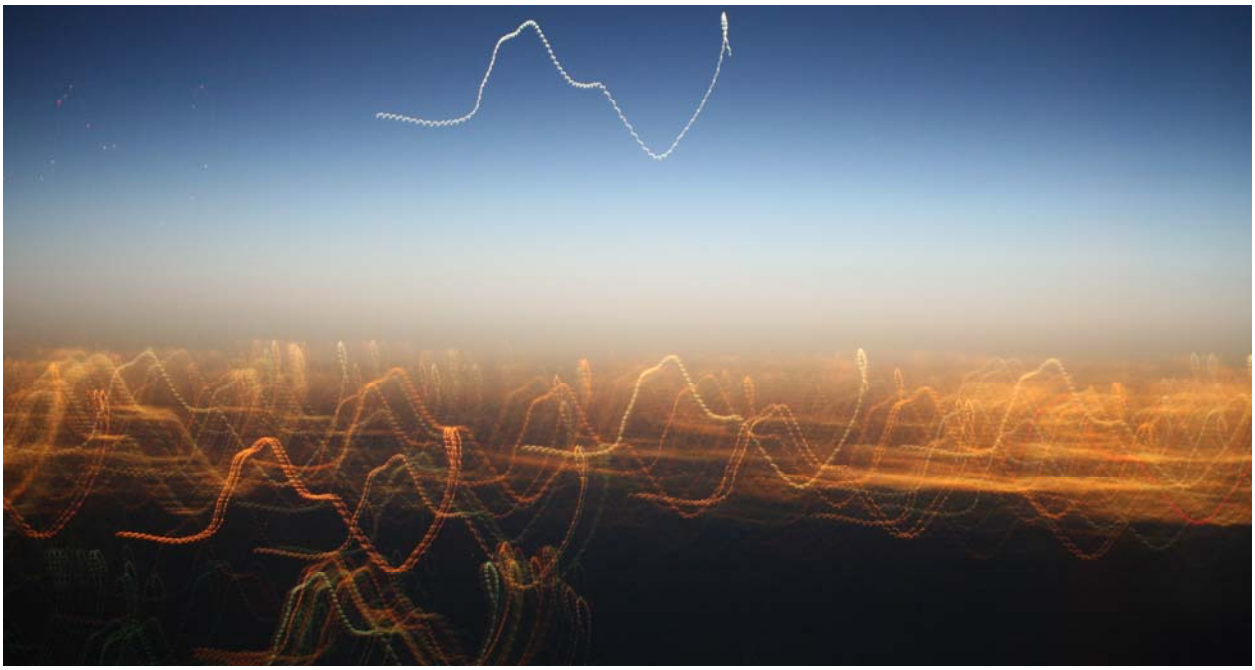

Figure 5.1: Jitter assessment with SDA = 12.34 degrees, Exposure = 5.0s, f/1.6, ISO 800

In Figure 5.2a, we can see that the vibration pattern produced by the horizontally-opposed, six cylinder Continental TSIO 360LB engine has a vertical oscillation succeeded by a horizontal oscillation. Figure 5.2b shows a star pattern under nighttime lighting conditions through an exposure of 20.0s. This figure shows that the aircraft, under fairly calm conditions as might be expected for NLC observations, will produce up to about a 2 degree vertical change in FOV and up to a 1 degree change in horizontal FOV. This corresponds to about a 7% variation of the vertical range on the CCD.

a)  **b)** 

Figure 5.2: a) Engine vibrations, **b)** Close-up of star calibration over a period of 20 seconds (f/1.6, ISO 800)

5.2 Synchronized Observations of NLCs

The raw airborne image of the July 6 overpass is shown in Figure 5.3. The Rayleigh background was subtracted from this image using a sixth-order polynomial approximation but this product revealed no additional discernable features. The Rayleigh removed image is presented in Figure 5.4. The smaller, higher elevation image was taken 20 seconds after the larger, lower elevation image. NLC features in the airborne imagery were identifiable south of 63.5^{O}N. Analysis of the geolocated airborne imagery show two distinct bands, oriented at 330^{O} +/- 5^{O}, spanning a range of latitude from 63.5^{O} to 59.0^{O}N. By performing a linear fit to the two observed prominent bands and measuring the mean perpendicular distance, the separation distances were determined to average about 82 +/- 2 km and suggest that they could be part of a structure of this wavelength. Furthermore, an additional series of clouds were observed approximately orthogonal to the band structures, with an orientation of 45 +/- 5^{O}, lying approximately 75^{O} relative to the prominent band structures. In the same manner, this structure was determined to have a wavelength of 52 +/- 5 km and was observed between latitudes of 60.5^{O}N and 62.7^{O} N.

Figure 5.3: Imagery taken of NLCs from the aircraft at 00:48 MDT, 6 July 2009

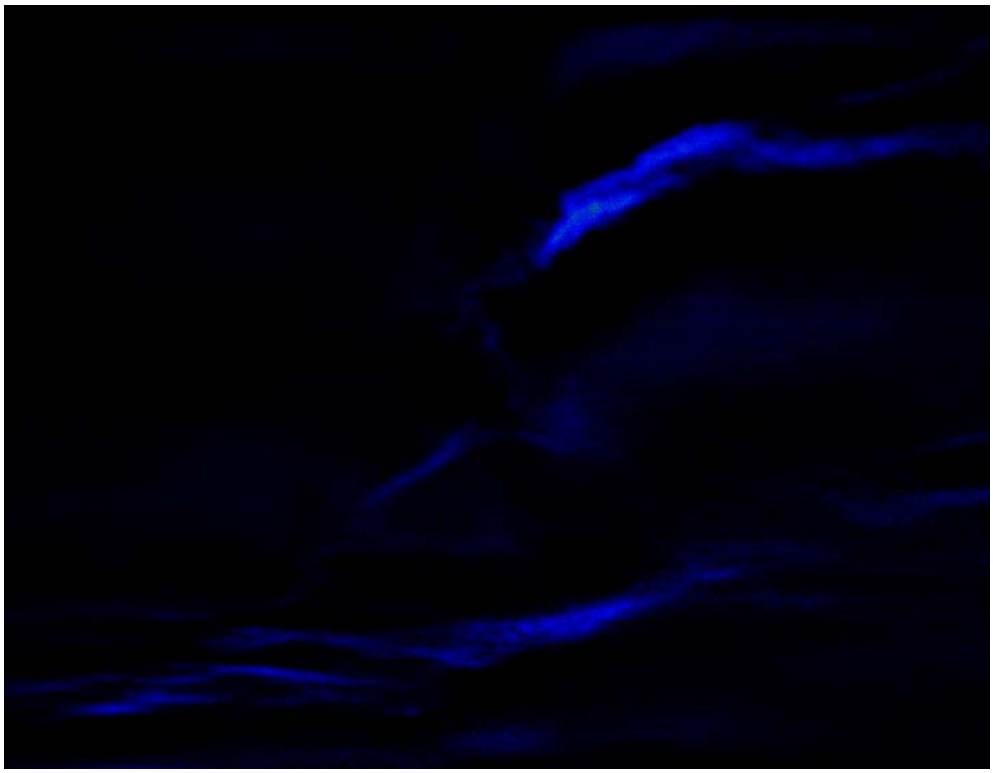

Figure 5.4: Imagery taken of NLCs from the aircraft at 00:48 MDT, 6 July 2009 with Rayleigh background removed using a 6^{th} order polynomial approximation.

Subsequent analysis of the CIPS imagery, as shown in Figure 5.5, confirms that a PMC was detected at this range of longitudes, though the CIPS camera was only sensitive north of approximately 62.5^{O}N and the signatures of PMC activity identified are near their threshold of sensitivity. The CIPS imagery also shows two band structures that extend to lower latitudes, oriented about 314 +/- 5^{O}. These bands are approximately separated by 100 km. The westernmost band of the CIPS image appears to be collinear with the most prominent band identified in the airborne image. The apparent similarity in band orientation lead us to believe that the observations of the airborne camera and the CIPS imager are of the same cloud structure.

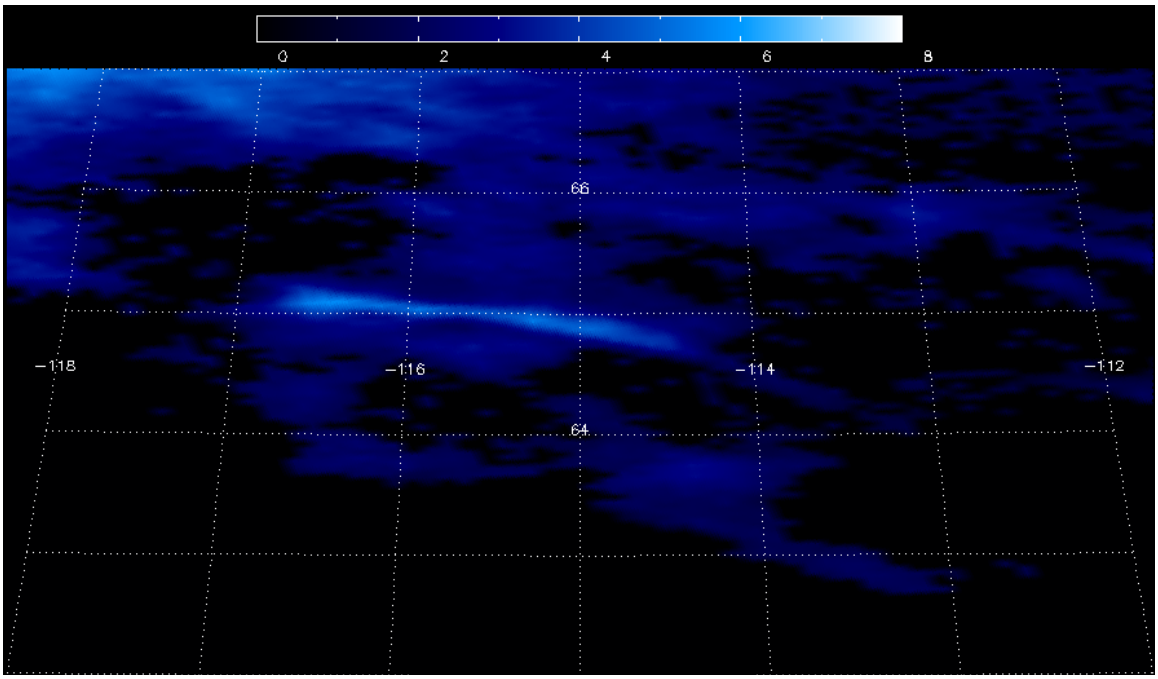

Figure 5.5: Imagery taken of PMCs from the CIPS imager at 00:48 MDT, 6 July 2009. The latitude-longitude grid is over-plotted on the CIPS image. The color table gives the PMC albedo values x 10-6 sr-1

To illustrate this point, the images were plotted together. Figure 5.6a shows the airborne imagery geolocated and Figure 5.6b shows the same imagery with the spaceborne imagery mutually geolocated. The image obtained from the aircraft shows band structures along the same orientation and geographic area as the CIPS image. Both CIPS and the airborne image show distinct, extended band structures but only the airborne camera is able to identify fainter orthogonal features, which are finer structures but clearly discernable features oriented at an azimuth of 045 +/- 5^{O} transverse to the band structures. Thus, the band structures are mutually identifiable features while finer structures are confined to aircraft camera images. As CIPS can resolve wavelengths no less than 10 km [Chandran et al. 2009], the airborne cameras can resolve wavelengths as low as 150 m. Thus, the orthogonal structures extend within the CIPS region of possible detection but due to their fine and relatively weak signals cannot be detected in the 5 km resolution of the CIPS images used for this analysis.

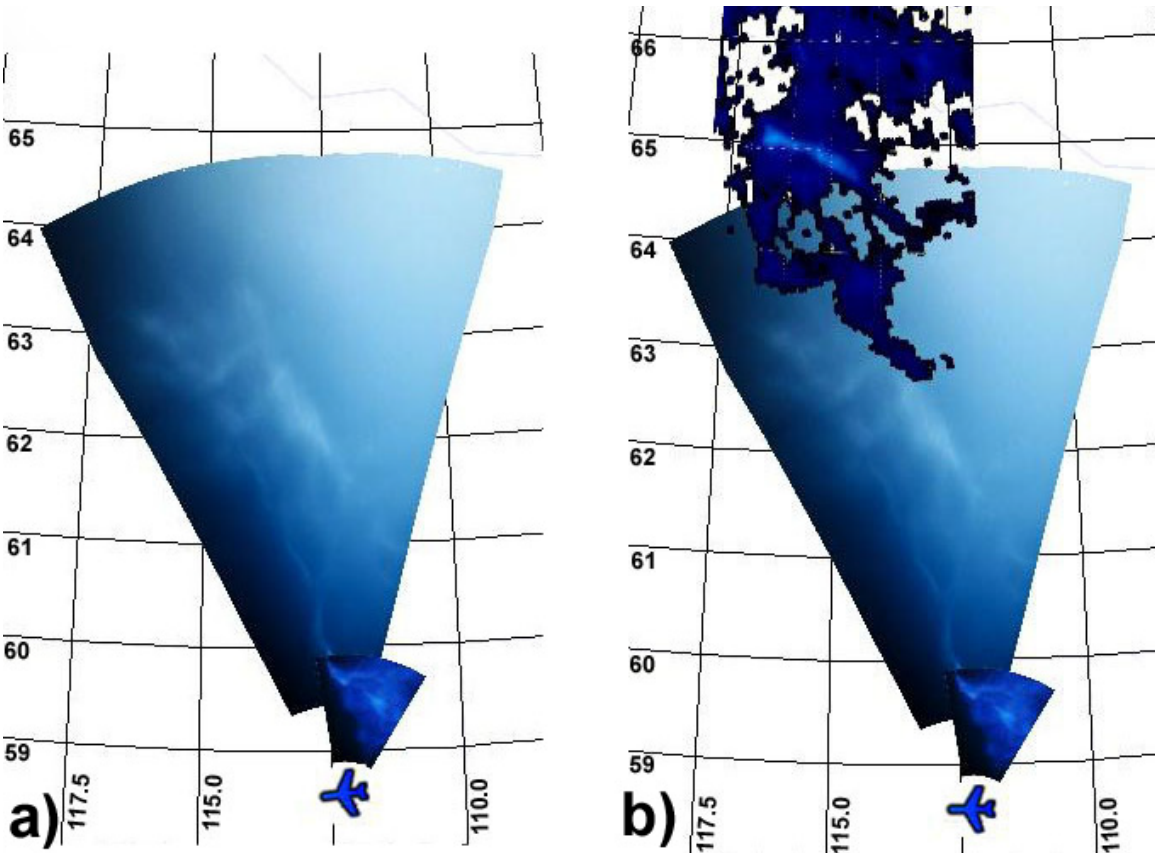

Figure 5.6: **a)** Geolocated projections of imagery obtained from only the airborne camera, and **b.** geolocated projections of imagery from both airborne and spaceborne platforms.

5.3 Temporal Evolution of Noctilucent Clouds

No useful data was obtained that could address the question of temporal evolution of NLCs. During the campaign the flight profile was fully flown in three sorties, though in only one sortie were NLC formations visible. The second sortie was successful in intercepting the AIM satellite and obtaining two hours of observation data maintaining a constant SDA of 8.5 degrees, though the prominent NLC formations formed more to the east than was possible for the imagers to image while the aircraft was on its planned trajectory.

5.4 Validation of CIPS Algorithms

The airborne observations were able to improve the ability of the CIPS processing algorithm to extract data near the day-night terminator. These improvements were important as the low-latitude clouds are the clouds that are most sensitive to minute fluctuations in the surrounding environment and are thus presumably the best indicators of climate change. As CIPS detects the effect of solar terminator illumination, the clouds perceived by CIPS are not necessarily the low-latitude 'edge' of the clouds. The identification of the common bands observed by the aircraft that extended to lower latitudes than the band observed by CIPS was used to increase confidence in accepting a lower signal threshold in the CIPS processing algorithm and to identify how far, to lower latitudes, NLC structures could exist beyond what is observed by CIPS. The version 4.1 signal threshold is currently several Garys (One Gary (G) is defined as an albedo of $1x10^{-6}$ sr^{-1}). The airborne observations were also useful in better determining the size and albedo threshold of cloud formations that would be observable from

CIPS as many of the meridional band structures observed by the aircraft cameras were, and many of the finer transverse, zonal band structures were not, observed by CIPS.

The increase of CIPS ability to discriminate cloud presence further helped to infer cloud particle sizes as a wider range of scattering angles better characterizes the azimuthal dependency of the scattering geometry. The CIPS cloud detection sensitivity varies with solar zenith angle for two reasons: as the solar zenith angle increases the Rayleigh background signal decreases, while at the same time the CIPS sunward (PX) camera samples more forward-peaked scattering angles [Lumpe et al, 2009].

5.5 Sensitivity Analysis

Aircraft Position and Altitude:

Error associated with aircraft position was determined by the greater of either 1) the precision the pilot could intercept the predetermined waypoint at the time of AIM overpass, or 2) the error of the calculated longitude and latitude values assigned to the waypoints was 0.01 degrees, or roughly 1.1km in latitude or 0.6km on longitude. The GPS instrument error was considered negligible. It was deemed that the error intrinsic to the positional coordinates sufficiently bounds position error.

As the aircraft altitude was maintained by the autopilot system slaved to the altimeter, the error in altitude was determined by the accuracy in which the altimeter was set to the local

pressure settings. As real-time weather is rare due to the remoteness of the campaign, it was estimated that altitude error was +/- 100ft (30.5m).

Satellite Position and Altitude:

Satellite position and altitude was provided by satellite orbital prediction and determination tools that are maintained by two-line element (TLE) orbital ephemeris data provided by NORAD. Satellite position and altitude data were provided by the Laboratory of Atmospheric and Space Physics (LASP) in Boulder CO. Error associated with satellite position and altitude was considered negligible for this study.

Camera azimuth and elevation:

Camera azimuth error was bound by pilot precision as there were no ground reference points from which to calculate the azimuth. As the camera was mounted so that the line-of-sight was normal to the longitudinal axis of the aircraft, the azimuthal error contained components attributable to aircraft heading error and aircraft yaw. At time of satellite intercept, the flight crew attempted to maintain a heading perpendicular to the projected AIM groundtrack so that the boresight of the imager was parallel to the satellite groundtrack. It was estimated that pilot precision, heading indicator error, and yaw combined to contribute to an overall error in the azimuth of the images of +/- five degrees. Future campaigns would benefit by the use of a geotagger.

Camera elevation was determined post-campaign through knowledge of the vertical FOV (28.1 degrees) and the horizon. Elevation angle was set at +12 degrees of the roll axis of the aircraft so the horizon could be visible provided that roll was maintained within two degrees of error. Elevation error was introduced by error in our knowledge of the cloud deck height that provided the horizon reference.

Geolocation Error:

It was assumed that the CIPS projections were accurate and contained no error. Error was then assessed for the aircraft image projection for five variables: latitude, longitude, altitude, camera elevation, and camera azimuth. These variables are tabulated in Table 5.2. Aircraft image geolocations were performed under numerous permutations of these variables and it was found that aircraft position error produced no noticeable effect upon the image geolocation. Altitude was paired with camera elevation to frame the limits of geolocation error; the low altitude limit was paired with the low elevation limit and the high altitude limit was paired with the high elevation limit. It was found that the effects of the altitude error also produced no noticeable effect on image geolocation.

As azimuth was bounded by error bars of +/- 5 degrees and elevation was bounded by error bars of 0.5 degrees, these two variables were considered the driving sources of error in the geolocation of the images. The extremum values of these variables were used to produce a geolocated image with the CIPS projection. These are shown in Figure 5.7a for the variation in elevation and Figure 5.7b for the variation in azimuth. It was decided that the use of a geotagger in future experimentation would reduce this error greatly.

Variable	Tolerance	Projection Error
Latitude	+/- 1km	No noticeable effect
Longitude	+/- 0.4km	No noticeable effect
Altitude	+/- 100ft (31m)	No noticeable effect
Camera Elevation (relative to horizon)	+/- 0.5 degrees	Shown in Figure 5.7a
Camera Azimuth	+/- 5 degrees	Shown in Figure 5.7b

Table 5.2: Error ranges for camera projection

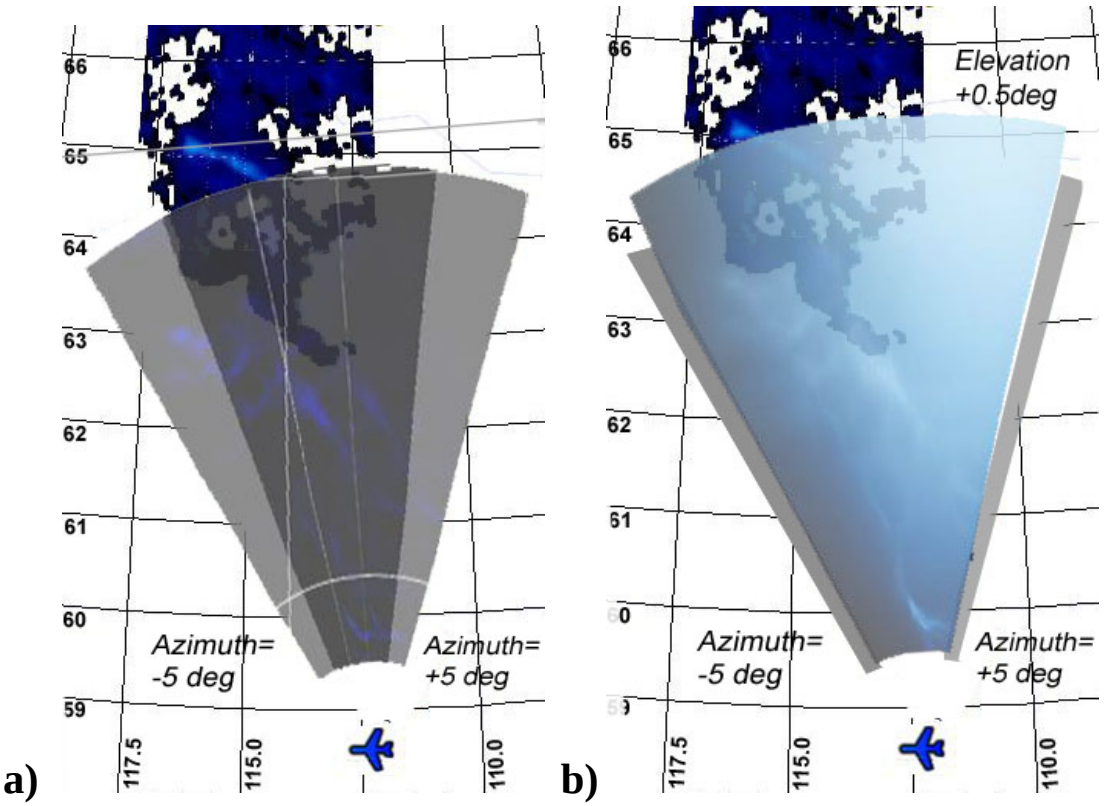

Figures 5.7: a) error range in azimuth (=/- 5 deg), **b)** Error range in elevation (+/- 0.5deg)

6. Synchronized imagery of noctilucent clouds at the day-night terminator: Conclusions and future research

6.1 Conclusions

NLC structures in a common observing volume were observed from a synchronized airborne and spaceborne platform on 6 July 2009. The aircraft imagery obtained from an altitude of 5486 m clearly identifies the orientation and wavelengths of NLC structures south of 63.5^{O}N latitude. The spacecraft imagery obtained from the CIPS imager identifies structures residing north of 62.5^{O}N latitude. NLC bands separated by about 82 km and weak NLCs orthogonal to the bands with 52 km separation are observed in the airborne imagery. The coincident CIPS image indicates similarly aligned band structure, although the orthogonal cloud structure appears to be too weak to be identified in the CIPS image. This spatial similarity in band structure, combined with the apparent similarity of band orientation, lead us to believe that the observations of the airborne camera and the CIPS imager are of the same cloud structure. To our knowledge, this represents the first such coincident measurement of NLCs from airborne and spaceborne instruments. This experiment also verified that synchronous imagery of NLC structures could be obtained through use of airborne and spaceborne imagers with about 100 km of overlap if the aircraft is flown at least 18000 feet altitude.

The results of this experiment were limited as we 1) did not have the opportunity to conduct extensive pre-campaign flight testing. This was a result of delays incurred by the company we had entrusted to overhaul the engine and annual the aircraft before the campaign, and 2) the meteorological conditions in and about the campaign area created more icing risks

than were anticipated. The use of an aircraft with known-ice capabilities available for a full flight test regime prior to an NLC campaign should produce significantly better results.

6.2 Future research

In future campaigns it is hoped that through more coincident observations of NLCs from the airborne camera and PMCs from successive AIM orbits, we can gain a deeper insight into the temporal evolution of NLC structures. This could partly address the questions regarding the rapid change in PMC structures seen in successive AIM orbits and give insight into the effect of GWs in PMC formation and evolution. In addition, additional experiments are proposed using improved camera control systems incorporating a geotagger to record camera positioning with greater accuracy.

Additional testing is proposed to determine the variation of sky/ground ratio upon shutter speed, refine the vibration mitigation methods, and to characterize the polarization of the background sky as a function of SDA. Additional flight tests would 1) assess the variation of sky/ground ratio upon shutter speed by setting the cameras to the 'Aperture Priority' setting and taking images at times of several SDA values, 2) assess the ISO Settings of the cameras and further refine the vibration mitigation methods by using two cameras fitted with linear polarizers oriented orthogonal to each other, and 3) characterize the polarization. An accurate assessment of polarization will help future campaigns optimize the signal to noise ratio of NLC imagery as both the Rayleigh background and the cloud scattering are polarized. Further, magnitude of polarization is a factor that can be used to infer particle size.

In future campaigns it is hoped that through more coincident observations of NLCs from polarized and geo-tagged airborne cameras and PMCs from successive AIM orbits, we can gain a deeper insight into the temporal evolution of NLC structures and their magnitudes of polarization.

7. Selection and application of remote sensing techniques to determine the glacial sliding distribution at Sermeq Avannarleq

The study of volumetric trends of the Greenland Ice Sheet has long been a topic of importance towards understanding the effects of a changing global climate due to its implications on sea level rise. Many methods to measure ice dynamics and volume have been employed over the last half-century, though the early methods using photometric surface velocity measurements and in-situ ice-flow observations have produced models of limited accuracy. The tools that would enable a comprehensive study of ice sheet changes, such as airborne and spaceborne radar, space-based gravimetry (e.g. GRACE), and LiDAR systems, have only been in place throughout the last two decades. These tools have produced precise current volumetric measurements of the Greenland Ice Sheet as well as short-term observations of the volumetric change, though the projections of observed trends are still highly speculative and rely on a number of assumptions. Large uncertainty exists in any future projections of the evolution of the ice sheet resulting from a relative lack of knowledge of the mechanisms that control the mass balance and could thus drive an accelerated disintegration of the ice sheet through a positive feedback cycle. As introduced in Chapter Three, these positive feedbacks are anticipated from the effects of both the melt-induced acceleration when enhanced surface melting causes water to penetrate to the bedrock and reduce basal friction, as well as the force imbalance that occurs at the calving front when floating ice thins. Thinning at the calving front also causes an increase in sliding velocity as the glacier becomes more buoyant, reducing frictional back forces as the net normal force is reduced and permitting salt-water intrusion that further drives the buoyancy of the glacier. The reduced resistive force at the calving front is then propagated up glacier via longitudinal extension because of the backforce reduction [Thomas et al., 2003]. Therefore, it is clear that a greater understanding of the contribution of sliding to glacial dynamics will help

support future efforts to project glacial mass balance trends as profiles of sliding ratio can help us estimate the degree of lubrication that is transpiring at the glacial base via meltwater penetration and/or saltwater intrusion. This is the non-linear characteristic that could lead to rapid collapse of the Greenland Ice Sheet.

The different applications of integrative remote sensing methods in this study demonstrate how similar techniques may be used in very different ways. The Greenland Ice Sheet is of similar geospatial scale to noctilucent clouds, and can also effectively be observed through integrative methods of remotely-sensed data. This study seeks to further the understanding of the Greenland Ice Sheet by determining the relative role of sliding versus deformational motion to better assess the effects of sliding in a changing climate that could be driven by increased water penetration and lubrication of ice or increased salt water penetration near the termini of outlet glaciers. Due to the complex nature of the problem, various sources of data were employed in the development of the supporting models.

7.1 Selection of data sources and region of interest

The following data sources are employed in this study: 1) imagery from the SPOT-5 satellite, 2) surface velocity data obtained through interferometric techniques using the RADARSAT-1 satellite, 3) surface elevation data from the ICESat satellite, 4) surface elevation data via the Airborne Topographic Mapper (ATM) airborne scanning LiDAR onboard the NASA P-3 Orion research aircraft, 5) ground penetrating radar data from the Multichannel Coherent Radar Depth Sounder (MCoRDS) onboard the NASA P-3 Orion research aircraft, and 6) ground-based temperature and mass balance observations at various locations within the region of

interest (ROI). The roles of each of these data sources will be explained in the following sections.

The ROI was defined by the availability of data about the Sermeq Avannarleq glacier terminus and is bounded by 69.16N to 69.70N degrees of latitude and 50.50W to 48.00W degrees of longitude. The Central Greenland region is shown in Figure 7.1 along with the groundtracks from ICESat and Operation Ice Bridge overpasses, shown as the red and blue tracks respectively. The extent of data available within this region is large due to its proximity to the highly-studied Jacobshavn Isbrae and was thus a major factor in its selection.

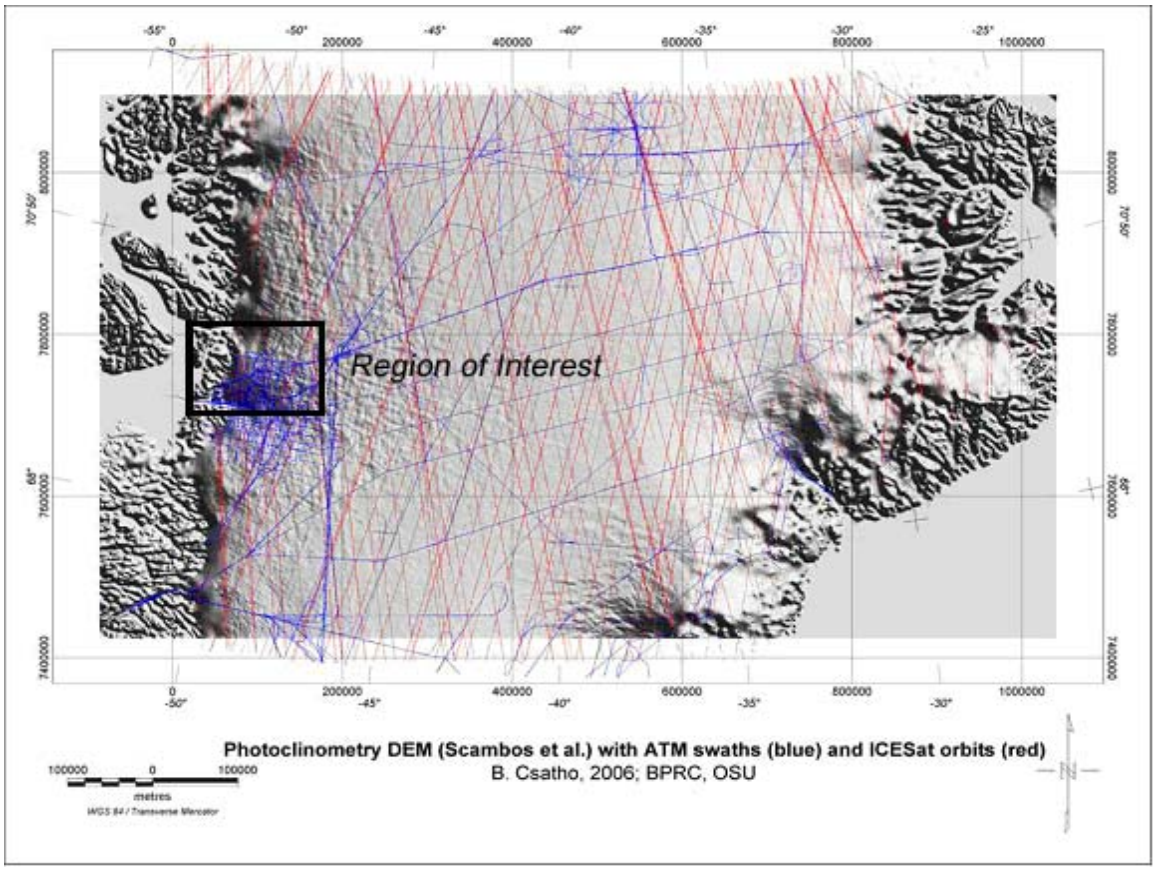

Figure 7.1: Region of Interest with Ice Bridge and ICESat groundtracks

7.2 Space-based LiDAR

Spaceborne LiDAR was first implemented with the Lidar In-Space Technology Experiment (LITE), which flew onboard STS-64 in September 1994. LITE was successful in demonstrating that laser remote sensing was possible from space at 1064, 532, and 355nm [Gu et al., 1997]. Following the success of LITE, the Geoscience Laser Altimeter System (GLAS), a space-based LiDAR, was developed. The Ice, Cloud, and land Elevation Satellite (ICESat) was launched on 13 January 2003 into a 600km near-circular, near-polar orbit, to support the GLAS instrument, from which polar-specific coverage of the Greenland Ice Sheet was obtained [Abshire et al., 2005].

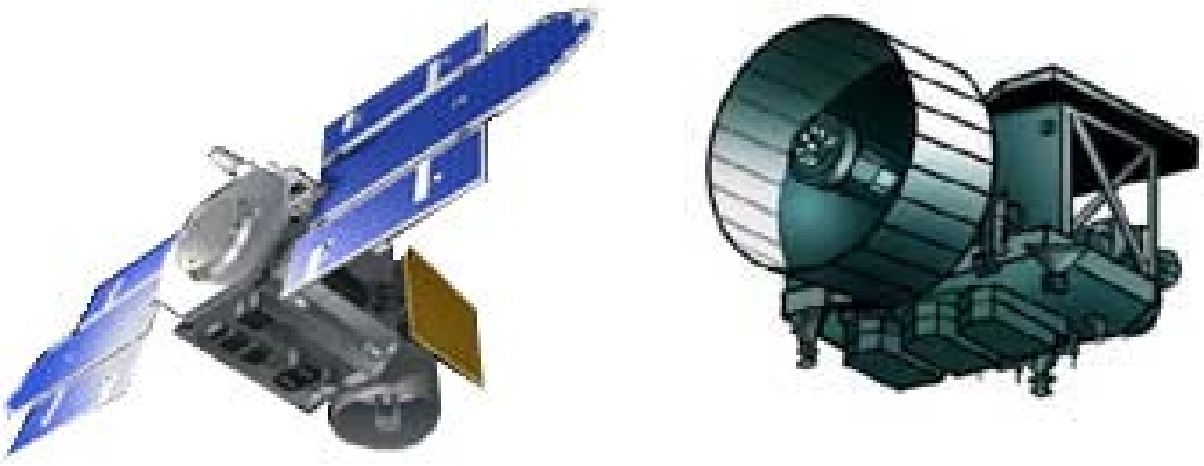

Figure 7.2: ICESat and the GLAS instrument

Like LITE, the GLAS lasers emitted infrared and visible laser pulses at 1064 and 532 nm wavelength producing a series of approximately 70 m diameter laser spots separated by an along-track distance of 170m. ICESat was initially placed into an 8-day repeating orbit and maneuvered in 2004 into a 91-day repeating ground track. Nearly two months into its 91-day operation, premature laser failure resulted into the operation of ICESat in a sequence of 33-day seasonal campaign modes until the end of its mission in 2009. The primary mission of the GLAS payload aboard ICESat was to determine the range from the spacecraft to the ice surface, data that was later processed to measure changes in the ice mass balance over time by comparing the changes of surface elevation over a time series of sequential groundtracks [Abshire et al., 2005]. In 2009, a digital elevation model (DEM) was produced from the GLAS/ICESat laser altimetry profile data consolidated in 2007 [DiMarzio et al., 2007]. In this analysis, these data were used to provide ice elevation and time rate-of-change data.

7.3 Space-based synthetic aperture RADAR

Ice-flow velocity controls the rate at which ice is transported from regions of accumulation to regions of ablation. A major factor regulating the ice mass balance is discharge through outlet glaciers, and this discharge generally exhibits a non-linear response to the calving of icebergs that significantly affect the ice mass balance. Thus, knowledge of the velocity and strain rate (i.e., velocity gradient) are important in assessing mass balance and in understanding the flow dynamics of ice sheets. Ground-based measurements of ice-sheet velocities are scarce because of logistical difficulties in collecting such data. In contrast, interferometric synthetic aperture RADAR (InSAR) provides a means to measure both detailed topography and flow velocity over large, featureless areas of ice that comprise much of the ice sheets. To date, the most comprehensive data set has been produced by RADARSAT-1 [Joughin et al., 2002].

Surface velocity observations were obtained from the InSAR radar onboard the RADARSAT-1 satellite in the form of a 500m x 500m grid. In 2005 and 2006, RADARSAT-1 imaged most of Greenland four consecutive times, producing three InSAR pairs from which surface velocity values were given at each gridpoint [Joughin et al., 2010]. Data were expressed in terms of in meters per year in the x and y directions as defined by the polar stereographic grid. The velocities are determined using a combination of conventional InSAR techniques, that are true values and not subject to the distance distortions present in a polar stereographic grid, and speckle tracking techniques that determine the displacements between scenes in an interferometric pair using the cross-correlation function of the speckle patterns rather than of visible features [Joughin et al., 2002].

RADARSAT was chosen as a key data source as it provided the most comprehensive spatial coverage surface velocity data that was also highly accurate. Though similar mappings by RADARSAT have occurred annually through the 2008/09 season, the 2005/2006 surface velocity data set was selected as it is the most comprehensive data set available.

7.4 Space-based imagery

In contrast to the CIPS camera, the spaceborne imagery used to study glaciers can not effectively be performed in the UV and is instead performed in visible and infrared wavelengths, where the lower atmosphere appears transparent (in the absence of cloud cover) and space can be used as an effective background. SPOT-5 (Figure 5.2) is a commercial imagery satellite launched on May 4, 2002 and was used as the source of space-based imagery in this study. SPOT-5 resides in a polar, sun-synchronous orbit that effectively images the surface of the Earth every 26 days and supports a High-Resolution Geometric (HRG) instrument and a High

Resolution Stereoscopic instrument (HRS). The 90kg HRG cameras produce imagery of a resolution of 2.5 to 5 meters in panchromatic mode, 10 meters in multispectral mode, and 20 meters in short wave infrared 1.58 - 1.75 μm that is used to create DEMs with no use of ground control points. These cameras have a resolution higher than that of previous SPOT satellites due to an onboard stellar location unit that uses both a star tracker and gyroscopic data to compute the absolute orientation of the satellite (source: www.spotimage.com).

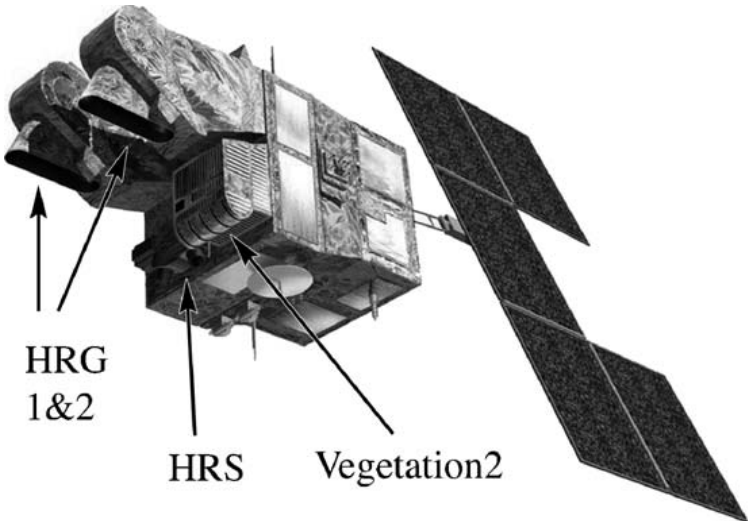

Figure 7.3: The SPOT 5 Satellite. Payloads include two High-Resolution Geometric (HRG) instruments, the High Resolution Stereoscopic instrument (HRS), and two vegetation imagers.

The HRS instrument consists of two telescopes allowing along-track stereoscopy with a 20° fore view and a 20° aft view. The two cameras allow a stereo pair to be acquired within an interval of only 90 s following the satellite track and covering an area of 120 km wide by up to 600 km long. The DEM used is generated by first determining the relative orientation of each HRS pair, correlating each stereo-pair, and then processing the absolute geometry globally through bundle block adjustment over large areas. A summary of the resolution and spectral bands are provided in Table 5.1. The camera pairs have a horizontal circular absolute accuracy of 15 m at 90% of all data points and a vertical accuracy dependent upon surface slope (www.spotimage.com):

- 10 m at 90% for slopes lower than 20%;
- 18 m at 90% for slopes between 20% and 40%;
- 30 m at 90% for slopes greater than 40%.

Electromagnetic Spectrum	**Pixel Size**	**Spectral Bands**
P: panchromatic	2.5 m or 5 m	0.48 - 0.71 μm
B1 : green	10 m	0.50 - 0.59 μm
B2 : red	10 m	0.61 - 0.68 μm
B3 : near infrared	10 m	0.78 - 0.89 μm
B4 : mid infrared (MIR)	20 m	1.58 - 1.75 μm

Table 7.1: SPOT-5 HRS sensor resolution and sensitivity (source: www.spotimage.com)

7.5 NASA's Operation Ice Bridge

Operation Ice Bridge is a NASA mission that aims to monitor changes in polar ice from a P-3 Orion or a DC-8 research aircraft. The airborne missions aim to supply vital observations of the polar ice in the years between the decommissioning of the ICESat satellite in 2010 and the launch of ICESat II in 2016. The aircraft carries many payloads dedicated to the study of the polar ice including the Airborne Topographic Mapper, which is a scanning LiDAR that measures the surface elevation of the ice, a gravimeter capable of measuring the shape of cavities in the ice, a Laser Vegetation Imaging Sensor (LVIS), the MCoRDS depth sounder that measures the thickness of the ice, a Snow Radar, and the Ku-Band Radar Altimeter. Flights over the Greenland Ice Sheet are conducted in the spring months. Flightlines are generally planned in all regions of the island, with high resolution grids over more active outlet glaciers. When possible, flightlines from ICESat or previous Ice Bridge campaigns are repeated to determine changes of ice elevation in those locations. (source: www.espo.nasa.gov/oib/)

7.5.1 Airborne imagery

Airborne photography was obtained onboard the P3 Orion aircraft in the Operation Ice Bridge campaigns through the Digital Mapping System (DMS) in a manner very similar to the noctilucent cloud study, though the imagers used on the Ice Bridge campaigns were used only as a means to validate the LiDAR observations. The DMS is based around a Canon EOS 5D Mark II digital camera that acquires high resolution natural color and panchromatic imagery from low and medium altitude research aircraft. The EOS 5D is very similar to but more sensitive than the EOS30D used for the noctilucent cloud experiment as it has a 36 x 24 mm CMOS sensor with

21.1 million effective pixels. The camera is coupled with a Canon F1.8 28mm lens that has a 70° FOV. At a flight altitude of 1500ft AGL, the camera produces a cross-track and along-track FOV of 64.0^{o} and 45.2^{o} respectively. The resolution is 0.1m at this altitude (source: www.espo.nasa.gov/oib/). As the airborne imagery obtained by the DMS was used as a means to validate LiDAR observations, the data were not used as an input to the glacial sliding models of this study.

7.5.2 Airborne LiDAR

Airborne LiDAR is a powerful capability used in the Operation Ice Bridge campaigns. The Airborne Topographic Mapper (ATM), shown in figure 7.4, is a scanning laser altimeter developed to measure topography below the aircraft to accuracies typically <15cm RMS vertically and <50cm horizontally. The system consists of an aircraft laser instrument rack, and optical transceiver, an aircraft GPS/navigation instrument rack and a small Litton 100G Inertial Navigation System (INS). The laser transmitter emits a short (~5ns) green (523nm) optical pulse 5000 times per second that produces an ~1-meter diameter footprint on the ground below the aircraft. Processing of the transmit and return waveforms and the measured time delay between the outgoing laser pulse and received signal allows calculation of the time of flight range with an accuracy of <5cm RMS. The outgoing laser beam and receiver field of view are swept in a conical pattern by a nutating scan mirror to produce a swath width of 30 or 45 degrees, depending on which transceiver is used. A Litton LN-100 INS logs aircraft attitude (pitch roll and heading). Aircraft position is determined post-mission using kinematic differential techniques applied to the GPS carrier phase data logged during the flight by airborne and ground-based receivers. The processed product consists of latitude, longitude, and elevation

coordinates for each laser footprint geolocated within the ITRF (international terrestrial reference frame) ellipsoidal coordinate system. ATM data obtained over Greenland have a reported accuracy of ±10 cm [Krabill et al., 2002].

The ATM data was used in this analysis to validate the surface elevation data provided by the SPOT DEM and to provide fixes where a 2005 surface elevation model may be extrapolated.

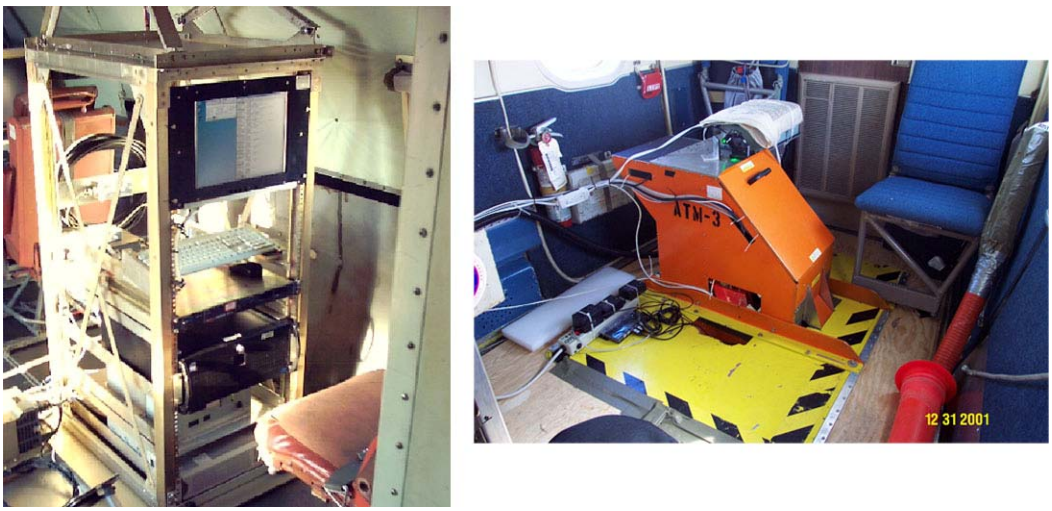

Figure 7.4: Airborne Topographic Mapper (ATM)

7.5.3 Airborne ice-penetrating RADAR

The MCoRDS system was developed by the Center for Remote Sensing of Ice Sheets (CReSIS) to map the thickness of ice sheets. This radar system is a nadir-looking, five channel, monostatic radar system and was integrated onboard the NASA P3 Orion aircraft and used in Greenland as one of the primary sensors for NASA's Operation Ice Bridge (OIB). The MCoRDS data set includes measurements for echograms, time, latitude, longitude, elevation, and surface, as well as flight path charts and echograms images [Shi et al., 2010]. Basic parameters of MCoRDS are listed in Table 7.2.

The MCoRDS data was used in this analysis to determine the bedrock elevation along the nodes of analysis. Inter-annual variation of bedrock elevation was considered negligible.

Variable	Value
PRF	9000 Hz
Tx Signal Type	Linear up chirp
Signal Duration	1 and 10 μs
Center Freq	193.9 MHz
Bandwidth	10 MHz
Sampling Freq	111 MSPS
Transmit Power	500 W
Rx Noise Figure	5 dB

Table 7.2: Basic MCoRDS radar parameters [Shi et al., 2010]

7.6 Ground-based meterological sensors

The Greenland Climate Network (GC-NET) currently consists of 18 stations with a distributed coverage over the Greenland Ice Sheet that are equipped with instruments to measure surface energy and mass balance. Instrumentation integrated to each GC-NET station is described briefly in Table 7.3 and the locations of GC-NET stations and locations of individual instruments on each station are listed in Figure 7.5. The analysis herein relies on data from JAR 1, 2, and 3, Swiss Camp, and Crawford Point 1 and 2. Temperature and accumulation/ablation rate data is used to support models of mass balance and flow parameter in the ROI. The largest potential errors for temperature are in absolute temperature caused by radiative heating when wind speeds are small and solar radiation is great. Accumulation rate measurements based on surface height change only will be underestimates due to compaction [Steffen et al., 1996].

Parameter	Instrument	Instrument Accuracy	Sample Interval	# per station
Air Temperature	Campbell Sci. CS-500	0.1 °C	60 sec	2
Air Temperature	Type-E Thermocouple	0.1 °C	60 sec	2
Relative humidity	Campbell Sci. CS-500	5% < 90% RH 10% > 90% RH	60 sec	2
Wind Speed*	RM Young propeller-type vane	0.1 m s-1	60 sec	2
Wind Direction	RM Young propeller-type vane	5 °	60 sec	2
Station Pressure	Vaisala PTB101B	0.1 mb	60 min	1
Surface Height Change	Campbell SR-50	1 mm	10 min	2
Snow Temperature	Type-T Special Limits of Error Thermocouple	0.1 °	15 sec	10
Net Radiation	REBS Q* 7	5-50%	15 sec	1

Table 7.3: Locations of GC-NET stations

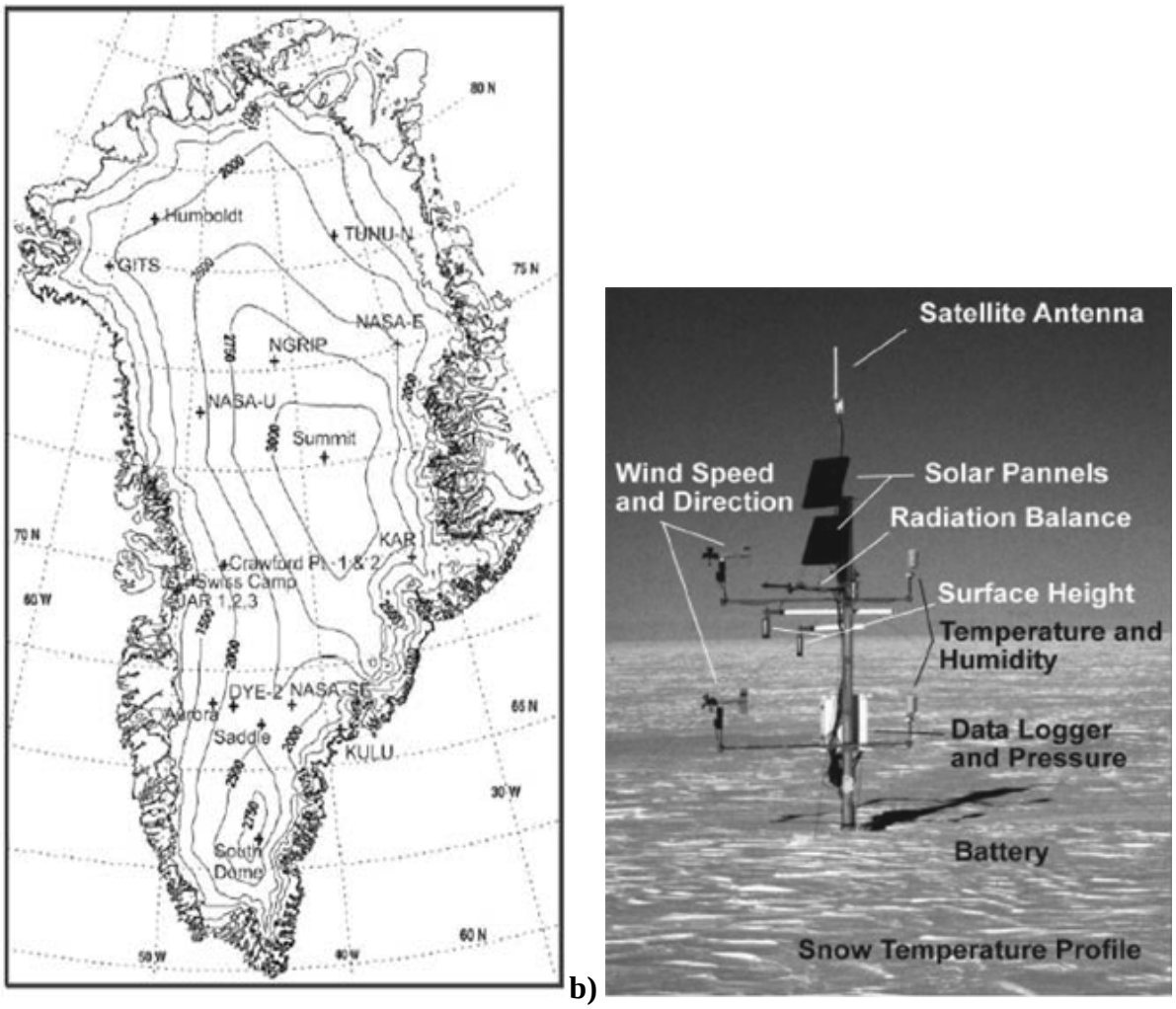

Figure 7.5: a) Locations of GC-NET stations in Greenland and **b)** individual instruments on each station.

8. Determining the relative contributions of glacial sliding in Sermeq Avannarleq, Greenland: Method and Source Data

The principle purpose of this analysis is to determine the contribution of sliding relative to deformation in the ablation zone near Sermeq Avannarleq and in doing so, establish a method from which sliding ratios could be inferred at other outlet glaciers, thus establishing a framework for assessing one of the largest uncertainties of climate change studies. A secondary purpose of this study is to identify where the greatest improvements can be made to observational and modeling techniques, which is enabled as a result of the integration of a wide range of observations and models.

8.1 Method

The relative contribution of glacial sliding was determined through the following procedure:

1) Defining the region of interest about a glacier possessing a sufficient amount of data to support the development of an integrative model.

2) Interpolating the 2005/2006 surface velocity data from RADARSAT-1 onto a standardized grid from which flowlines leading to the terminus of the glacier in the region of interest could be modeled.

3) Identifying the limits of the flowlines that discharge through Sermeq Avannarleq and that define the northernmost and southernmost limits of the flowtube and termed the bounding flowlines. Nodes of analysis are established along the central flowline.

4) Determining the width of the flowtube at each node of analysis. This is done by first determining the direction of the central flowline at each node, then creating a perpendicular bisector at each node, identifying the two locations where each bisector intersects the associated bounding flowlines, and finally calculating the distances between these two points for each node.

5) Interpolating the surface elevation data from the DEM produced from the SPOT-5 satellite for the year 2009 onto the nodes of analysis.

6) Adjusting the 2009 surface elevation data to the 2005 reference year through use of the annual change of surface elevation data produced by the ICESat satellite at locations where the satellite groundtracks intersect the central flowline. Interpolation of these surface elevation change data to all nodes was performed through a polynomial fit.

7) Interpolating the basal elevation data from the bedrock map produced from the MCoRDS radar data onto the nodes of analysis.

8) Identifying for each node of analysis the data points along the flowline used by Phillips et al. (2011) possessing equivalent surface elevation and assigning values for accumulation, ablation, and flow parameter.

9) Calculating flux along all nodes by using the continuity equation along the flowtube and assuming steady state conditions. The upstream initial condition for flux is then set (at the

10) Defining the accumulation zone and the ablation zone based on assumptions of the equilibrium line (ELA) elevation currently defined by Swiss Camp elevation of 1150m above mean sea level. Swiss Camp has been maintained at the best approximation of ELA location [Reeh, 1989].

11) Calculating ice thickness using the shallow ice approximation, which vertically averages ice deformation, in the accumulation zone using both a method that is weighted heavily on surface velocity observations and also a second method that relies heavily upon surface slope observations, both methods assuming that cold-bed conditions do not permit sliding.

12) Calculating ice thickness in the ablation zone using the same shallow ice approximation over averaged distances along the central flowline. Through averaging sections of the ablation zone, the observed distances were always less than or equal to the calculated distances, thus supporting the assumption that the difference between measured and observed ice thickness is attributable to basal sliding.

13) Determining the relative percentage of basal sliding along nodes of analysis within the ablation zone.

14) Assessing the relationships between the magnitude of basal slope and the relative contribution of sliding in areas where the basal slope was both increasing and decreasing.

15) Performing a randomized, Monte Carlo-type analysis to account for the error intrinsic in the various instruments used in this analysis. Fifty randomized iterations were used to effectively provide a reasonable bound of the error distributions. After bounding the analysis by running the two extreme cases, it was determined that a greater number of iterations would have simply broadened the distribution but change the results little. A sensitivity analysis is performed to determine the effects of small variations in the assumed values of mass balance, basal elevation, and flow parameter.

MacAyeal (1992) used a least squares approach using control points and a numerical model in lieu of a direct algebraic inversion, as is performed in this analysis. MacAyeal reasoned that a direct algebraic inversion was prone to error because the interpolation methods could affect the distribution of the coefficient of the basal friction and that there might be velocity gradients that cannot be explained by any distribution of basal friction, leading to complex results. The availability in this analysis of more accurate surface velocity measurements than the LANDSAT data that MacAyeal used allowed us to sidestep the dependency on the flow parameter and the surface slope and solve for ice thickness using only the surface mass balance and surface velocity data.

8.2 Source data

Source data were derived from a variety of spaceborne, airborne, and ground-based instrument sources. Spaceborne platforms provided surface velocity profiles and coarse surface elevation data, the latter used to determine the distribution of surface slope. Airborne platforms

provided bedrock elevation data throughout the ROI. The glacial elevation data as used in this model were first provided through spaceborne laser altimetry and then refined through the use of airborne laser altimetry. Finally, ground-based in-situ observations from GC-NET automated weather stations provided mass balance data as well as temperature distribution data instrumental in determining a profile of the flow parameter.

Surface velocity field:

Surface velocities of the ice within the ROI were obtained by interpolating the surface velocity data from RADARSAT-1 onto a standardized grid from which flowlines leading to the terminus of the glacier in the region of interest could be modeled [Joughin et al, 2010]. Data were collected for the years 2005-2006 and provided in the form of a gridded velocity format in terms of orthogonal components, where the +u component corresponds to the northward component of velocity and +v corresponds to the eastward component of velocity. The magnitudes of surface velocity as produced by RADARSAT are shown in Figure 8.1.

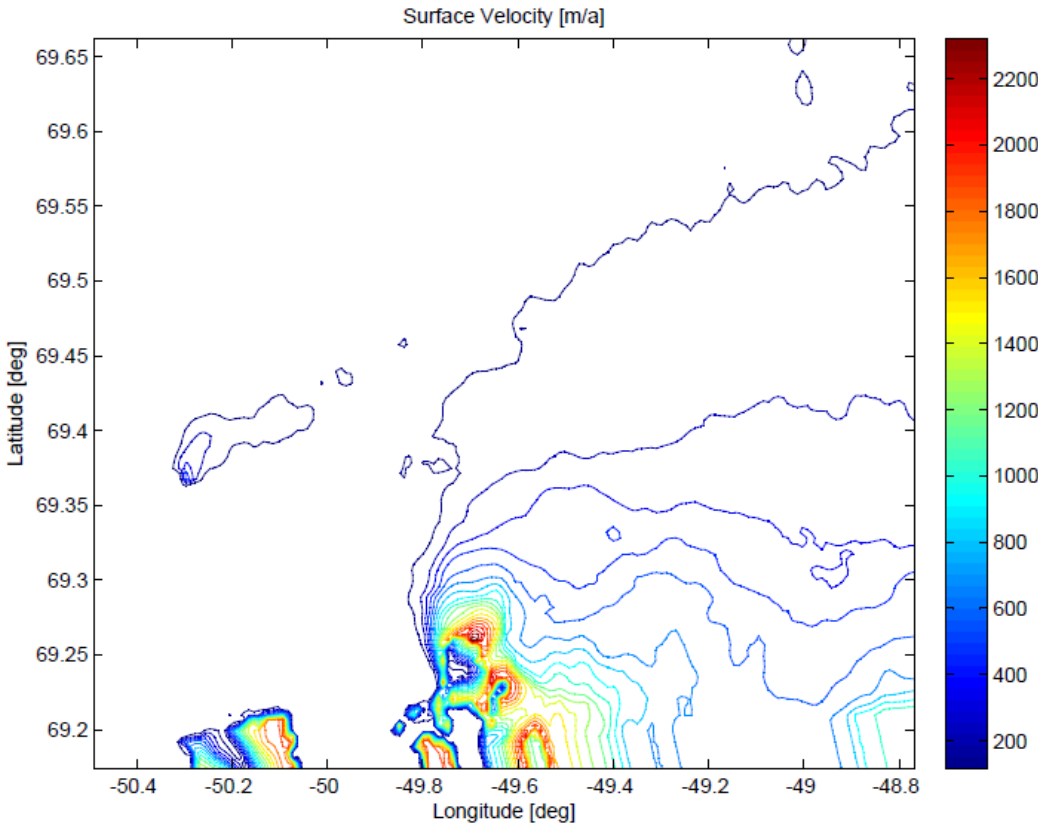

Figure 8.1: Magnitude of surface velocity derived from InSAR

The flowtube bounding the Sermeq Avannarleq terminus was determined by first bounding the border of the ROI with initial points and extracting flowlines through use of MATLAB's 'stream2' function. Once it was verified that some of the flowlines trace to the Sermeq Avanarleq terminus, the region encompassing the terminus was then gridded with initial points and flowlines were backtracked eastward from the terminus region. Seven bounding flowlines were then chosen whose starting points were equidistantly distributed along a line perpendicular to the central flowline. The central flowline was chosen as the flowline along which 401 equidistant nodes of analysis were selected. Node 1 was chosen as the easternmost node (near the boundary of the ROI) and node 401 was chosen as the node closest to the terminus of Sermeq Avanarleq.

As the effects of continuity need to be considered, the InSAR surface velocities were used to determine the width of the flowtube at each node. This was accomplished by first determining the azimuth of the central flowline at each node based upon a linear fit with the neighboring nodes. A trace bisector was extended perpendicular to this azimuth from each node and the locations at which this trace line intersects the bounding northernmost and southernmost flowlines were identified. The width at each node of analysis was then determined by calculating the distance between these two points of intersection. Thus, the analysis was conducted along flowline #4 whereas the width was determined from the range between flowlines 1 and 7 that define the bounds of the flowtube. A method of using perpendicular bisectors at each node was chosen as it could best account for curvature of the central flowline and thus determine the relative width of the flowtube more consistently than other methods. Figure 8.2 shows the seven flowlines extending from the terminus, the nodes spaced along the central flowline, and the trace bisectors extending from every ten nodes projected over a glacial terrain image (figure 8.3) and the surface velocity profile. Note the distortion is caused by the transformation of Lon/Lat coordinates to UTM Zone 22 coordinates.

The error in the width calculation is driven by several components including 1) error associated with the InSAR velocity measurements u and v, which were provided in the data given, 2) error associated with InSAR data interpolation, 3) the resolution of the grid from which the initial flowlines were backtracked, 4) the model error associated with the determination of intersection points between the bounding flowlines and the trace bisector. The error associated with InSAR velocity measurements and the interpolation of those measurements were assumed to be random and thus cancel out throughout the region of interest, so the only source of error for

the width calculation along the flowtube was the resolution of the model that produced the two points of intersection from which the width was calculated. The error associated with the measurements of the intersections of the perpendicular trace bisectors and the bounding flowlines was established at 30m, due to the resolution of the model being used. Dividing the sum of the error at the two intersecting points by the total distance between them showed the total error associated with the width calculations to be 1.7%.

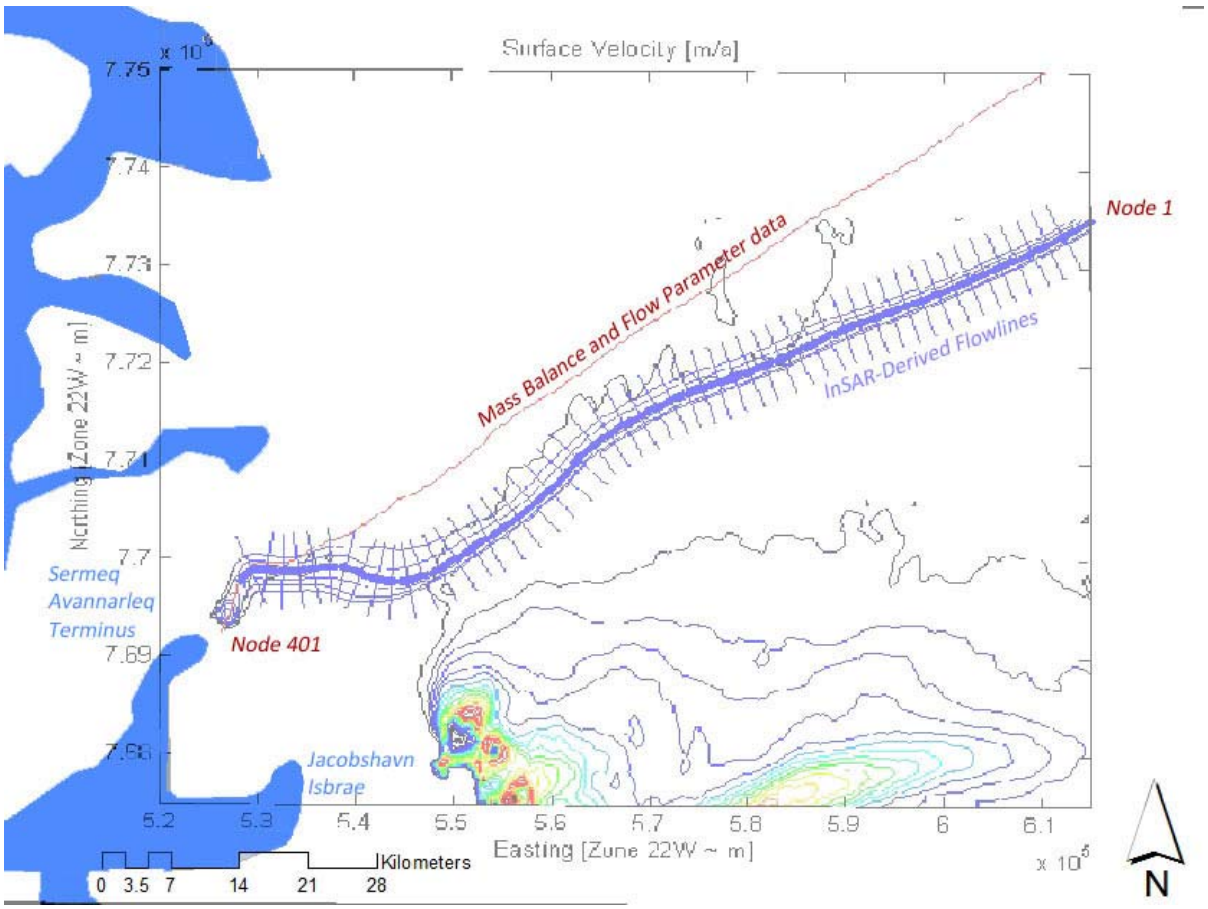

Figure 8.2: Surface velocity gradients about the Region of Interest

Surface Elevation

The surface elevation data assigned to each node of analysis was obtained by interpolating the surface elevation data from the DEM produced from the SPOT-5 satellite for the year 2009 onto the nodes of analysis. The DEM data of which the ROI is a subset is shown in Figure 8.3 and the same elevation data interpolated to a standard grid bounded by the limits of the ROI is shown in Figure 8.4 (The prominent outlet glacier in Figure 6.4 is Jacobshavn Isbrae). As introduced in Section Five, the SPOT-5 camera pairs used to generate the DEM have a horizontal circular absolute accuracy of 15 m at 90% of all data points and a vertical accuracy of 10 m at 90% for slopes lower than 20%. The vertical resolution of the DEM was enhanced through use of airborne LiDAR data so that the total elevation error, accounting for both measurement error in z as well as errors associated with the geolocation of the pixel, is +/- 0.7 m.

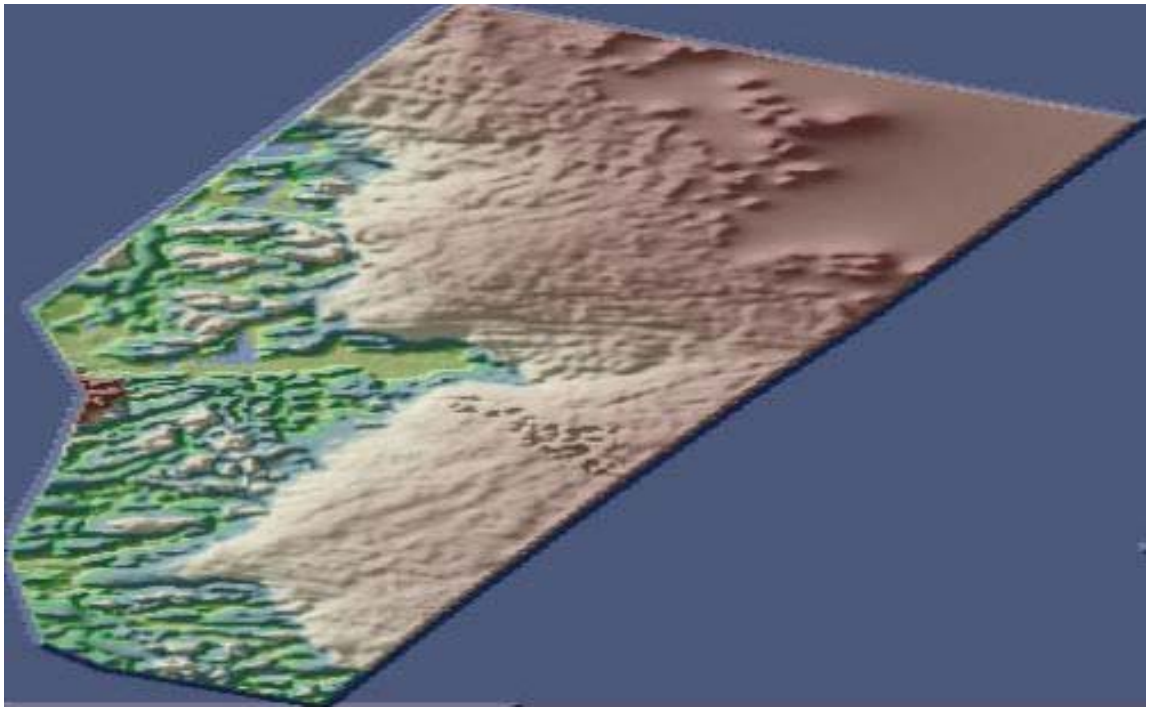

Figure 8.3: SPOT-5 data projection

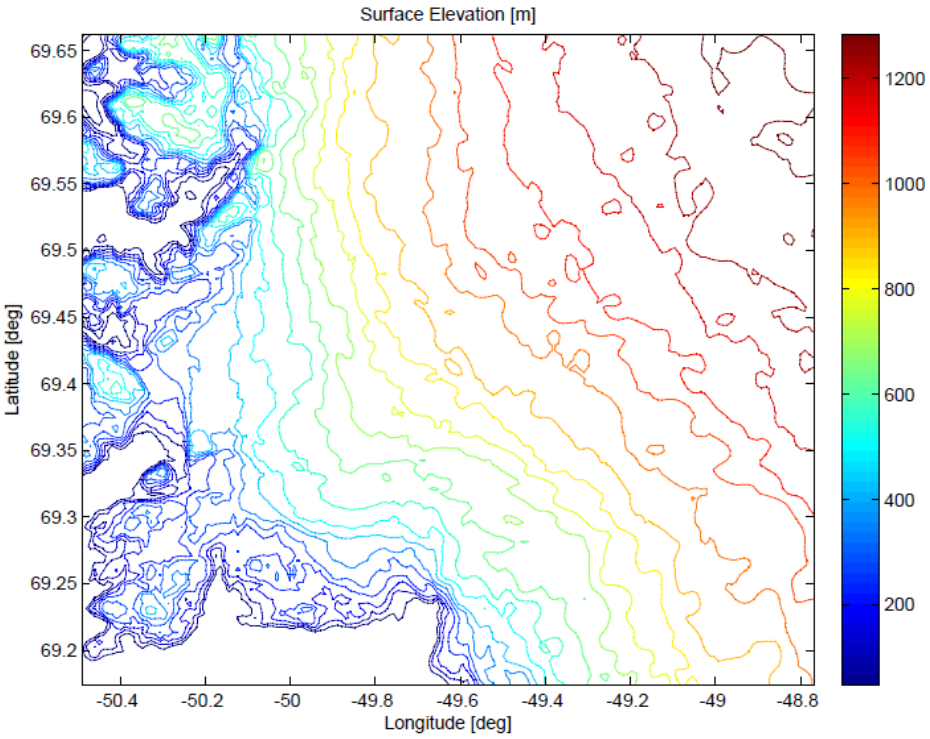

Figure 8.4: Surface elevation from SPOT 5 DEM

Normalization of observation years to a reference year

Because the surface velocity data were only available for the years 2000/2001 and 2005/2006, it was sensible to define one of these time periods as a standard reference year. As 2005 was most recent, it was chosen as the reference year. Though surface elevation data was produced consistently by the SPOT-5 satellite since its launch in 2003, it was not until 2009 when a comprehensive DEM was produced. Data from this DEM were adjusted for the change in surface height (dH/dt) between the observation year of 2009 and the reference year of 2005 using dH/dt data provided by the ICESat satellite overpasses [Zwally et al., 2010].

The ICESat estimated dH/dt data spans from campaign L2A (fall 2003) trough L2D (fall 2008). ICESat was unable to measure any appreciable change in dH/dt over shorter time spans, so it was assumed that the total dH/dt for the timespan between 2009 and 2005 is simply four times the annual change. The inability of ICESat to identify trends on shorter time scale results from the inability of the ranging laser beam to obtain a range at the same point for each overpass. Thus, many data points are needed over numerous overpasses so that an adequate data set exists to solve for both the elevation and the time rate of change of elevation [Zwally, H.J., 2011]. The ICESat overpasses in the ROI were plotted along with the central flowline, as shown in Figure 8.5, and the points of intersection where multiple year data exist. Table 8.1 lists all the points where data exists within the flowtube to Sermeq Avannarleq where multiple year data exists, from which data at other nodes and time periods could be extrapolated, and only lists the nodes closest to each place where flight lines of different years intersect. A polynomial fit was then made to these data to interpolate annual values for dH/dt to the entire set of nodes. Next, these values were multiplied by a scaling factor (4, if only the change between subsequent years was measured) so that the total dH/dt values could be summed to the 2009 DEM values previously assigned to the nodes [Zwally, H.J., 2011].

The accumulation and ablation data that comprise the surface mass balance were taken from the datasets of Burgess (2010) and Fausto (2009) for the years 2002 through 2008. It is assumed that the averaging of these seven years is representative of the accumulation and ablation values for the 2005 reference year. Though data were collected on basal elevation since 1993, the basal elevation is assumed to be constant and the data were used as provided by the University of Kansas. The data sets are summed and tabulated in Table 8.2.

Figure 8.6 illustrates the groundtracks of all the Operation Ice Bridge overpasses and ICESat overpasses within the ROI along with the points of intersection with the central flowline where there exists data. ICESat intersections are denoted with red circles while Ice Bridge intersections are denoted with blue circles. Figure 6.8 shows the raw data produced by ICESat overpasses in the ROI and averaged over each year. These data were used to determine the change of surface elevation between the 2009 observational year and the 2005 reference year.

Node	**0** (boundary)	**61**	**115**	**236**	**250**	**325**	**401** (terminus)
dH/dt (m/a)	-6.9199	-6.9199	-3.3862	-2.9624	-1.9353	-2.4042	-2.4042

Table 8.1: Annual dH/dt data along nodes of analysis

Data	**Source**	**Year of Observation**	**Adjustment to 2005 Reference Year**
Surface Velocity	InSAR	2005-2006	No change
Surface Elevation	SPOT-5 DEM	2009	Adjusted to 2005
Surface Elevation	ICESat Overpasses	2003-2008	Used to adjust 2009 DEM to 2005
Surface Elevation	ATM overpasses	2006-2008	Used to adjust 2009 DEM to 2005
Surface Temperature	Thomas (2010)	2002-2008	Sensitivity
Annual Accumulation	Burgess (2010)	2002-2008	Averaged
Annual Ablation	Fausto (2009)	2002-2008	Averaged
Bedrock Elevation	MCoRDS	1993-2010	Assumed Constant

Table 8.2: Source data projections to reference year

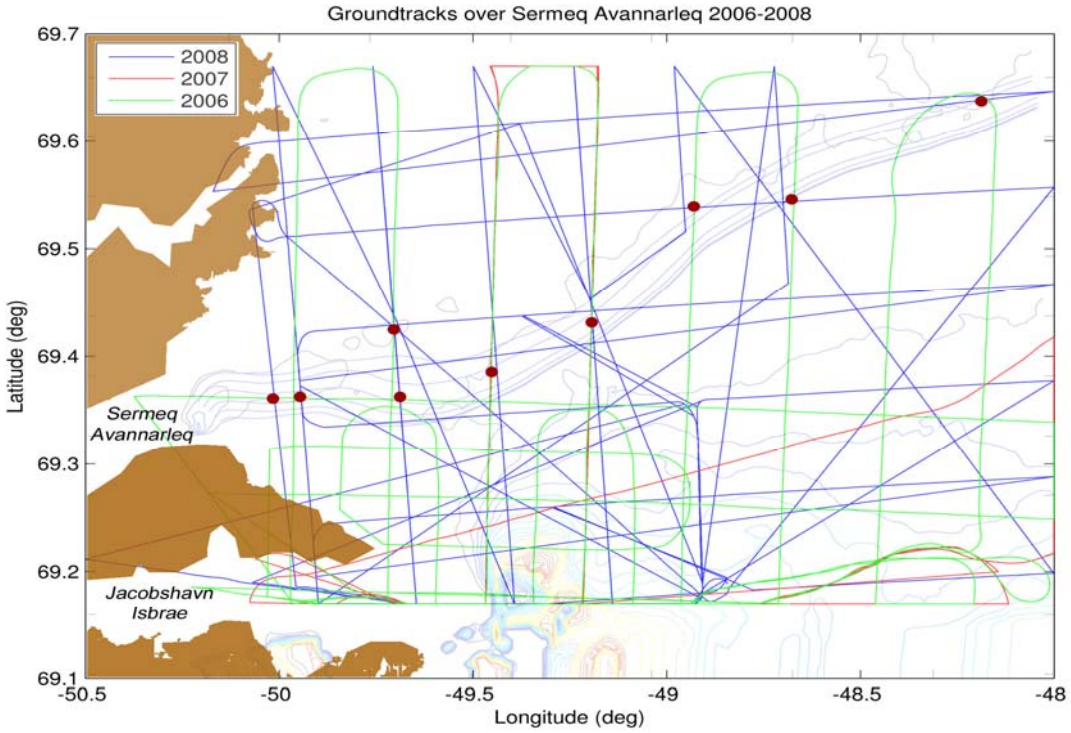

Figure 8.5: ATM groundtracks over Sermeq Avanarleq from 2006-2008. Dots represent intersections of subsequent campaign flightlines with the flowtube region [Krabill et al., 2002]

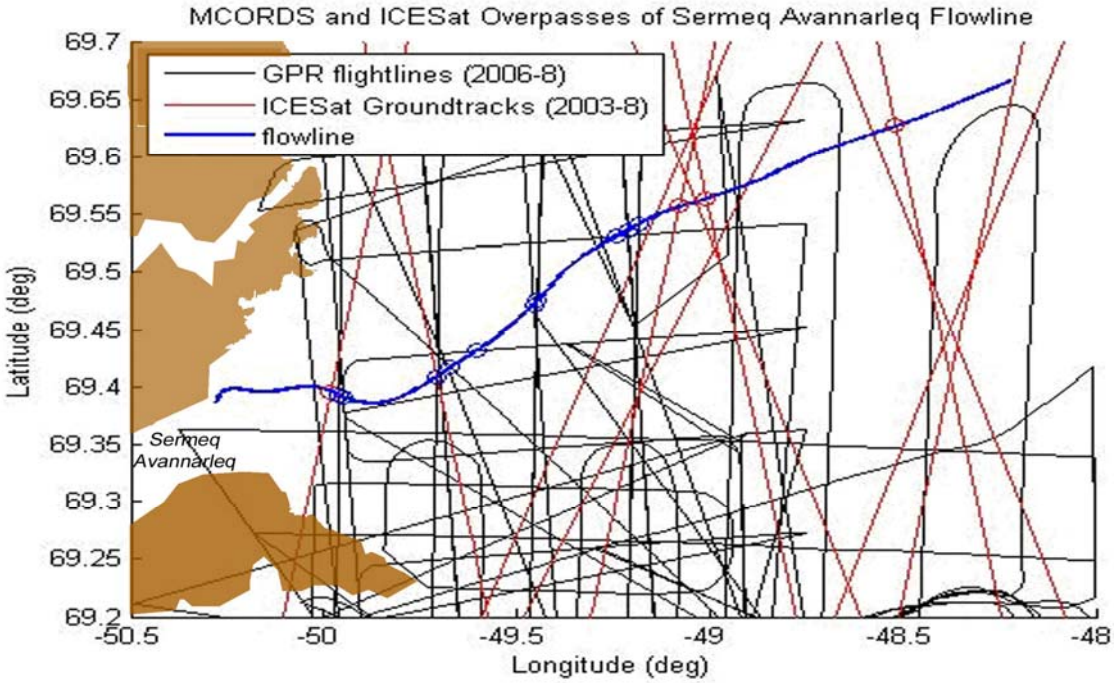

Figure 8.6: MCoRDS and ICESat overpasses of the Sermeq Avannarleq flowline [Krabill et al., 2002]

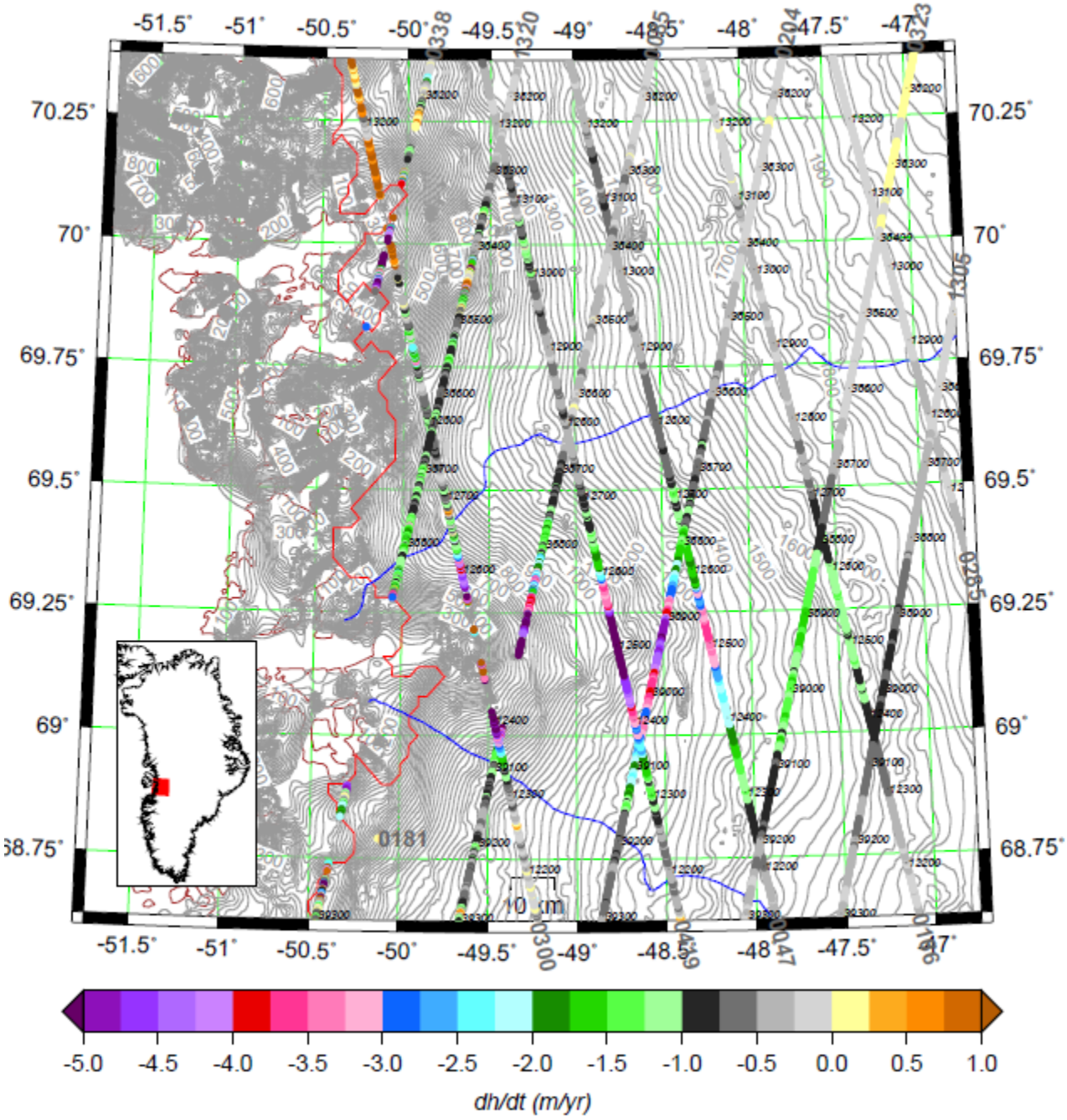

Figure 8.7: ICESat derived dH/dt data [Zwally et al., 2010]

Derivation of surface slope data from surface elevation observations

Surface slopes were derived from the 2009 DEM after it was adjusted to the 2005 reference year. A span of roughly ten times the ice thickness was used to determine the horizontal span through which surface slopes were calculated using MATLAB's 'polyfit' function of order one, which is in agreement with the recommendations made by Blatter [Blatter 1998]. As DEM horizontal resolution is approximately 20m, surface slopes were calculated through a linear fit centered at each DEM pixel location and spanning up to 300 pixels (~6 km) both plus and minus in northing and plus and minus in easting. This produced a sampling range of approximately 12km, which is roughly ten times the elevation of the glacier at the equilibrium line. Data were trimmed near the exposed terrain in the western portion of the ROI. Figure 8.8 shows the magnitudes of surface slope within the ROI.

Next, the 401 nodes of analysis along the central flowline were used to refine the determinations of slope along the flowline through a linear fit. Nodes within the ROI are spaced roughly every 225m and a span of 40 nodes (9000m) was chosen to determine slope along the flowline as the surface heights between node 21 and node 481 range from 600m to 1200m. Thus, each slope determination along the flowline was made on average over a span of roughly five to ten times the ice thickness. The 20 nodes closest to the easternmost limit (nodes 1-20) and the 20 nodes closest to the terminus (nodes 381-401) were interpolated from the comprehensive surface slope model described in the preceding paragraph. The slopes assigned to each node therefore derive from both an 'along-flowline' span and a two-dimensional slope model on the order of 10 ice thicknesses. As one of the methods used to determine ice thickness and thus sliding is highly dependent upon slope determination, it was important to make sure that

an accurate method was used to determine slope. The models used calculated the slope at each node by performing a series of trials that assumed spans ranging from one ice thickness to ten ice thicknesses. A horizontal distance of five ice thicknesses smoothed the distribution of slopes and produced a model not affected by the distribution of crevasses and other irregularities on the ice surface, confirming the conclusions of Blatter [1998]. In regions further inland, horizontal averaging distances of ten ice thicknesses could be performed since the slope calculations would not be affected by the exposed terrain near the coastal regions. This increased the precision of the slope measurements by making it more resilient to small undulations in the ice surface. The use of surface slopes derived from surface observations thus conforms to previous efforts to calculate basal elevation from surface observations [Blatter 1998].

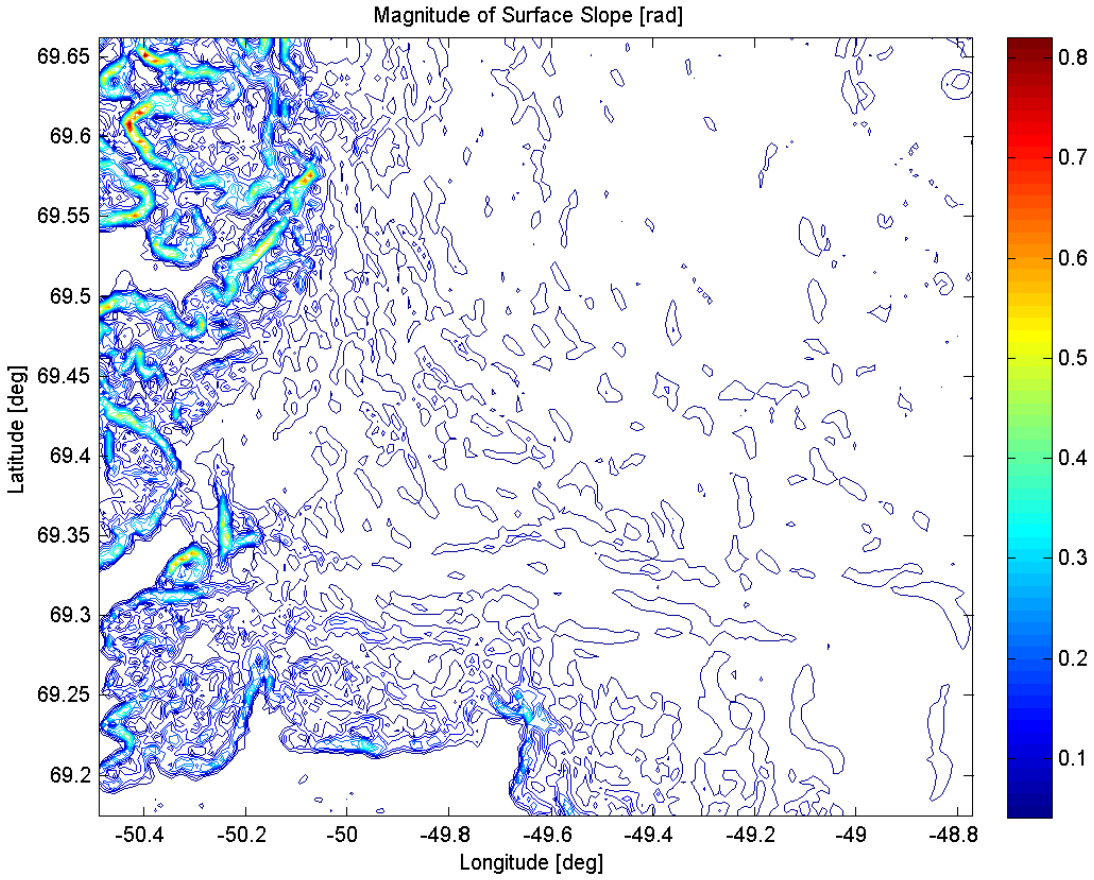

Figure 8.8: Surface slope magnitude

Basal Elevation:

Basal elevation data was obtained from the bedrock map produced from the MCoRDS ground penetrating radar data onto the nodes of analysis. Ice thickness data were provided in the format of a 500m x 500m grid and interpolated onto the nodes of analysis, as shown in Figure 8.9. If the assumption is made that the basal elevation is confined to six degrees of slope, as observed by the majority of the sub-glacial terrain using ice-penetrating radar, then the interpolation error is bounded by 10%. This is as observed in the results along the flowline and supports the assumption that the interpolation error associated with the basal elevation values assigned to the nodes is 62m [personal communication with Colgan]. The instrument error is 6.8m [Gogineni 2010]. Combined, the interpolation error and the instrument error contribute to an error of roughly 7% of the ice thickness. This figure does not account for model error that was produced when the bedrock map was created from the raw overpass data. It has been proposed that this model error can contribute an additional 12% error [Phillips et al., 2011]. Thus, the sensitivity analysis is designed to look at variations of basal error from 7% to 20%.

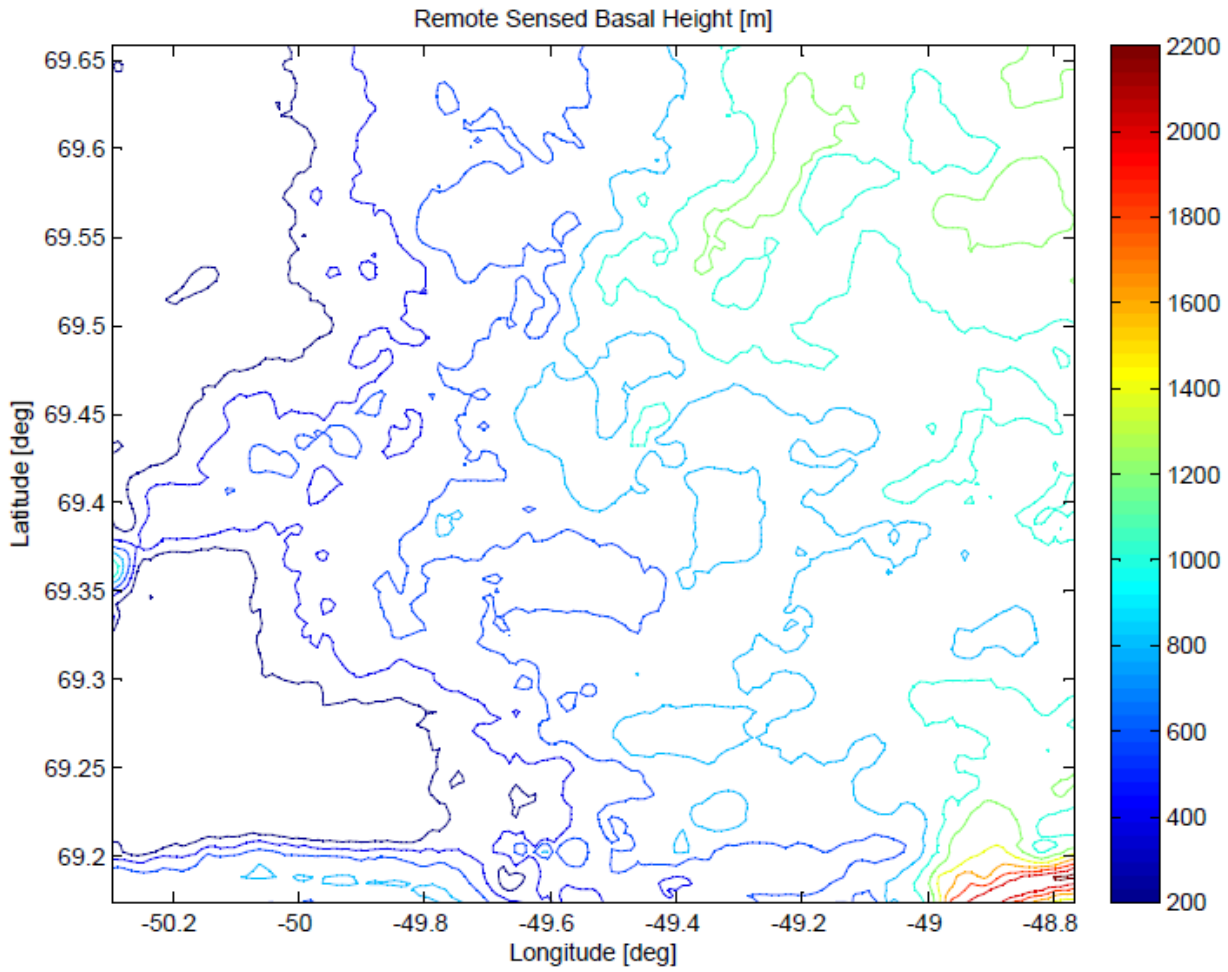

Figure 8.9: Ice thickness derived from MCoRDS

Surface Mass Balance and Flow Parameter:

The surface mass balance was determined along the central flowline through an analog analysis using the results presented by Phillips et. al (2011). The flowline used by Phillips et al. is shown in red in Figure 8.2 and deviates from the velocities observed with InSAR in this analysis. As the Thomas flowline has been used to generate a thorough and up-to-date analysis of surface mass balance and flow parameter, it is used as an analog flowline where surface elevation is the proxy. Thus, values of flow parameter and surface mass balance produced along the flowline of Thomas et al. were paired with the nodes of analysis in this study having the same surface elevation. A graphic representation of the flow parameter is illustrated in Figure 8.10.

The Phillips flowline derives the surface mass balance along its nodes by using a combination of both the accumulation data provided by Burgess et al. [2010] and the ablation data provided by Fausto et al. [2009]. Ice temperatures were calculated at varying depths to support a model of the flow parameter where temperature is variable over ice depth. Generally accepted values of the flow parameter exponent 'n' and the Wisconsan ice factor were used [Phillips et al., 2011].

Model iterations were performed for a range of perturbations, including flow parameter, basal elevation, and surface mass balance. Results were generated first using the standard constant value of the flow parameter of 3.0E-16, subsequently adjusted to incorporate the models of Phillips et al. (2011). Ranges of error spanning from 0 to 40% were used to determine the sensitivities of the assumptions of the flow parameter variable.

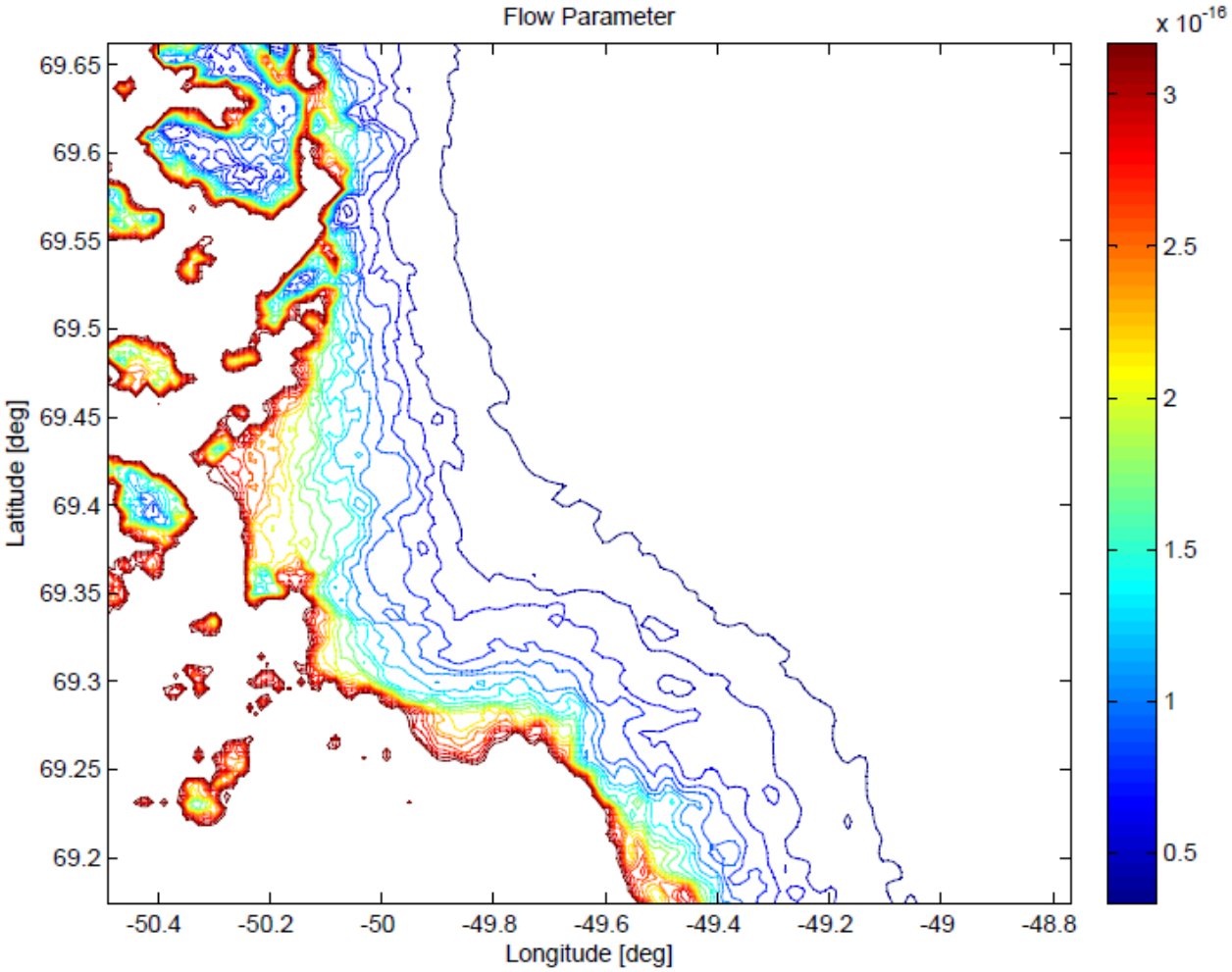

Figure 8.10: Flow parameter variability [Phillips et al, 2011]

Determination of the flux (q):

Where ξ represents the index of a node along the central flowline, the mass balance equation along the flowtube in steady-state can be expressed as:

$$\frac{d}{d\xi}\left(w(\xi)q(\xi)\right) = w(\xi)b(\xi) \qquad \text{(eq 8.1)}$$

where q(ξ) is the ice discharge per unit width at node ξ, w(ξ) is the width at node ξ, and b(ξ) is the surface mass balance at node ξ. This can be expressed as

$$\frac{dq}{d\xi} = b - \frac{q}{w}\frac{dw}{d\xi} \qquad \text{(eq 8.2)}$$

The rightmost term of equation 8.2 is the correction for convergence and divergence in a typical flowline model. If we express equation 8.2 in a finite difference form assign i as the index of nodes along the flowline, we get:

$$\frac{w_i q_i - w_i q_{i-1}}{\Delta\xi} = \frac{w_i + w_{i-1}}{2}\frac{b_i + b_{i-1}}{2} \qquad \text{(eq 8.3)}$$

Assuming that the surface mass balance data is reliable the flux along the flowline may be calculated from:

$$q_i^{MB} = \left(\frac{w_i q_i - w_i q_{i-1}}{2w_i} \right) \left(\frac{b_i + b_{i-1}}{2} \right) \Delta\xi + \frac{w_{i-1} q_{i-1}}{w_i} \qquad \text{(eq 8.4)}$$

The above relation provides one constraint on ice discharge based upon surface mass balance data. The ice discharge that is transported through flowline nodes via ice deformation may also be calculated through the shallow ice approximation. The upstream initial condition for flux is then set (at the upstream limit of the region of interest, designated node 1) so that the calculated basal elevation equals the observed basal elevation.

The shallow ice approximation, which assumes that the normal stress deviators and the sheer stress in the vertical planes may be neglected, may be employed to describe the vertically averaged ice deformation:

$$u = \frac{2A(z)}{5} (\rho g \sin\alpha)^n (z_s - z)^{n+1}$$

Assuming the common value of n=3, which has been a commonly accepted value following numerous empirical analyses on ice dynamics (Paterson, 1994), we may rewrite as:

$$u_{si} = u_{bi} + 2\int_{zbi}^{zsi} (\rho g \sin\alpha_i)^3 A(z)(z_{si} - z)^3 \, dz \qquad \text{(eq 8.5)}$$

Where the ice thickness at each node is defined by $(H_i) = z_{si} - z_{bi}$ and

u_{si} is the surface velocity (m/a),

$\sin\alpha$ is the local surface slope (in radians),

u_{bi} is the basal sliding velocity in (m/a),

z_{si} is the surface elevation (in meters above the WGS84 reference ellipsoid),

z_{bi} is the bedrock elevation (in meters above the WGS84 reference ellipsoid).

If we integrate equation 8.5 along the z-axis from the bedrock to the surface, we get:

$$q_i = \int_{z_{bi}}^{z_{si}} u_i(z)dz = u_{bi}H_i + \int_{z_{bi}}^{z_{si}} u_{di}(z)dz \qquad \text{(eq 8.6)}$$

Where u_{di} is the deformational velocity of the ice and may be expressed as:

$$u_{di} = \int_{z_{bi}}^{z} (2\rho g \sin\alpha)^3 A(z)(z_{si} - z)^3 \qquad \text{(eq 8.7)}$$

The integrals in equations 8.6 may be simplified if the assumption of a constant value for the Glen's Flow Law (Paterson, 1994) parameter is made at each node along the flowline. This value is representative of the lower third of the ice column where the shear forces would be strongest and we assume that all deformation occurs within this section of the ice [Paterson, 1994]. Thus, we can define the value for A as a function of both ice temperature and the presence of Wisconsan Ice.

$$u_{si} = u_{bi} + \frac{2\overline{A}_i}{4}(\rho g \sin\alpha)^3 {H_i}^4 \qquad \text{(eq 8.8)}$$

$$q_i^{MB} = u_{bi} H_i + \frac{2\bar{A}i}{5} (\rho g \sin \alpha_i)^3 H_i^5 \qquad \text{(eq 8.9)}$$

Defining the Accumulation Zone and Ablation Zone:

The surface elevation of the glacier increases steadily from the terminus to the divide. The equilibrium line was assumed to be at an elevation of 1150m, based upon surface climate data from Swiss Camp along the central flowline [Steffen et al., 1996]. The ELA is determined each year based on the surface mass balance data obtained at Swiss Camp. Along the central flowline, the location where the surface elevation passes 1150m corresponds to the location of node 220. The accumulation zone therefore encompasses nodes 1-219 and the ablation zone encompasses nodes 220-401. For the purpose of analysis, the accumulation zone is divided into two regions. The first region contains nodes 1-139 and surface slope is less than 0.4 degrees. The small slope values of this region causes equation 8.8 to "blow up", rendering the equation ineffective. The second region contains nodes 140-219 and has a surface slope of greater than 0.4 degrees.

Ice Thickness in the Accumulation Zone:

The accumulation zone is assumed to have a 'cold bed', or a basal temperature significantly below the pressure melting point. As such, we assume that the basal velocity is negligible. If we assume $u_{bi} = 0$ and that the surface mass balance data to be reliable, we can perform a numerical calculation down from the eastern boundary of the flowline to get a value of

flux derived from equation 8.4 that we call q^{MB}. We may then estimate the ice thickness through the following equation:

$$H_i = \frac{5}{4}\frac{q_i^{MB}}{u_{si}} \qquad \text{(eq 8.10)}$$

It then follows that the bed elevation may be obtained directly from known surface elevations

$$z_{bi} = z_{si} - H_i \qquad \text{(eq 8.11)}$$

Bedrock elevation data is obtained directly through ground penetrating RADAR data or it may be estimated in the accumulation zone through the analytical means presented in equation 8.10 if no such data is available.

Ice Thickness in the Ablation Zone:

The ablation zone is characterized by a negative mass balance and a basal ice temperature at or near the melting point. It can therefore no longer be assumed that the sliding velocity is negligible.

$$u_{si} = u_{bi} + \frac{2\overline{A}_i}{4}(\rho g \sin\alpha_i)^3 H_i^4 \qquad \text{(eq 8.8)}$$

$$q_i^{MB} = u_{bi} H_i + \frac{2\overline{A}i}{5} (\rho g \sin \alpha_i)^3 H_i^5 \qquad \text{(eq 8.9)}$$

If we recognize that $q_i^{MB} = u_{si} H_i$, we may use our observed values for α, derived from the previous discussion, and solve the above two equations for the two unknowns u_{bi} and H_i, to get:

$$q_i^{MB} = u_{si} H_i - \frac{\overline{A}_i}{10} (\rho g \sin \alpha_i)^3 H_i^5 \qquad \text{(eq 8.12)}$$

By solving this equation for H, this relation may be used to estimate the bedrock elevation and the sliding velocity in the ablation zone or more generally wherever there exists a temperate bed.

Determination of basal sliding:

It is assumed that there is no basal sliding in the accumulation zone. The relative percentage of basal sliding along nodes of analysis within the ablation zone is calculated and expressed in terms of meters per year. A fifth-order fit was made to the ablation zone data to better interpret the relative contribution of sliding. A fifth-order polynomial fit was chosen after comparing polynomial fits up to the tenth-order. The boundary condition was set so that the slope of the polynomial fit was negative at the upstream boundary (node 200), so only odd-order polynomials were considered. The linear (1st order) fit was not considered since the r-squared fit was too small and it did not seem to capture the general form of the data. A fit was then sought where the fluctuations attributable to variations in basal slope were smoothed over, and he 7th

and 9th order fits seemed to be affected by basal slope changes on the order of 1km. The 5th order fit was chosen as it provided a better r-squared fit than the 3rd order fit, did not seem to be affected by variations in basal slope on the order of 1km, and upheld the assumption that the glacier behaves in a way that the relative sliding percentage is introduced as the static friction is overcome near the ELA and increases towards the terminus. After the polynomial fit was made, fluctuations in the calculated sliding ratios were then correlated with basal slope by calculating the magnitude of basal slope in several areas and determining the relative effects upon the percentage of sliding to overall observed surface velocity.

Error and Sensitivity Analysis:

A Monte Carlo-like analysis of 50 iterations was then performed to account for the error intrinsic in the various instruments used in this analysis. A sensitivity analysis was then performed to determine the effects of small variations in the assumed values of mass balance, basal elevation, and flow parameter.

9. Determining the relative contributions of glacial sliding in Sermeq Avannarleq, Greenland: Results and Sensitivity Analysis

9.1. Results

Values for basal elevation (z_b), surface elevation (h_s), surface slope (deltam), mass balance (b_i), surface velocity (v), width (w), and flow parameter (A) were interpolated to each of the 401 nodes of this analysis. Figure 9.1 shows the relative relationship between each variable. In the interests of presenting the data in a way so that it could fit on the same graph and be observed in a comparative manner, multipliers were applied to several variables as listed below.

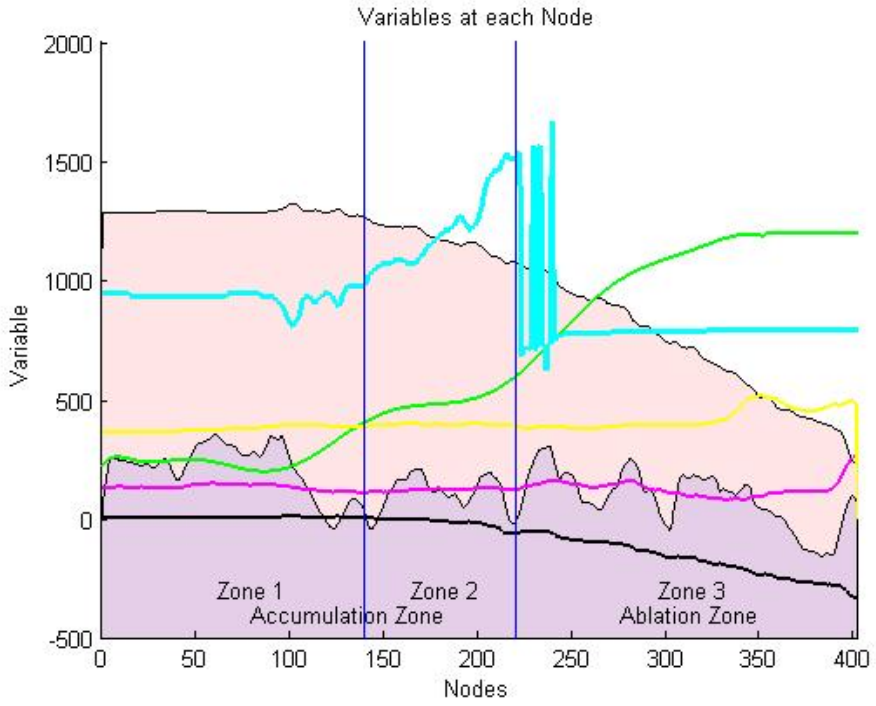

Color	Variable	Units	Multiplier
Blue	Basal Elevation	m (MSL)	1
Red	Surface Elevation	M (MSL)	1
Green	Surface Slope	rad	50000
Black	Mass Balance	m/a	100
Magenta	Surface Velocity	m/a	1
Yellow	Width	m	0.1
Cyan	Flow Parameter	m^{-3}	5.0E18

Figure 9.1: Model variables

Figure 9.2 graphically shows the values of the remotely-sensed ice thickness combined with various methods of ice thickness calculation given surface observations. The calculated thickness values in this figure assume no sliding (u_b=0) and also that the flux q^{MB} , obtained by employing a numerical method from the eastern bound using the continuity relation, assumed the ice to be incompressible (a standard assumption in glaciology). In the accumulation zone, the ice thickness as calculated from equation 8.10 and illustrated in green conforms well to the remotely-sensed data since sliding is assumed to be negligible. The ice thickness as calculated from equation 8.8 also conforms well provided that the surface slope is greater than 0.40 degrees (as shown in region two). This equation has an advantage in that it relies largely on spaceborne surface velocity measurements and thus takes greater advantage of the relatively higher accuracy of these data. However, the equation becomes unreliable when the surface slope becomes less than 0.40 degrees (as shown in region one) as a result of the exponential dependence of $(\rho g \sin\alpha)$ that quickly approaches zero as α is minimized. To maintain the equality, the ice thickness term 'blows up'. However equation 8.10, being independent of surface slope, provides consistent results as it is independent of surface slope.

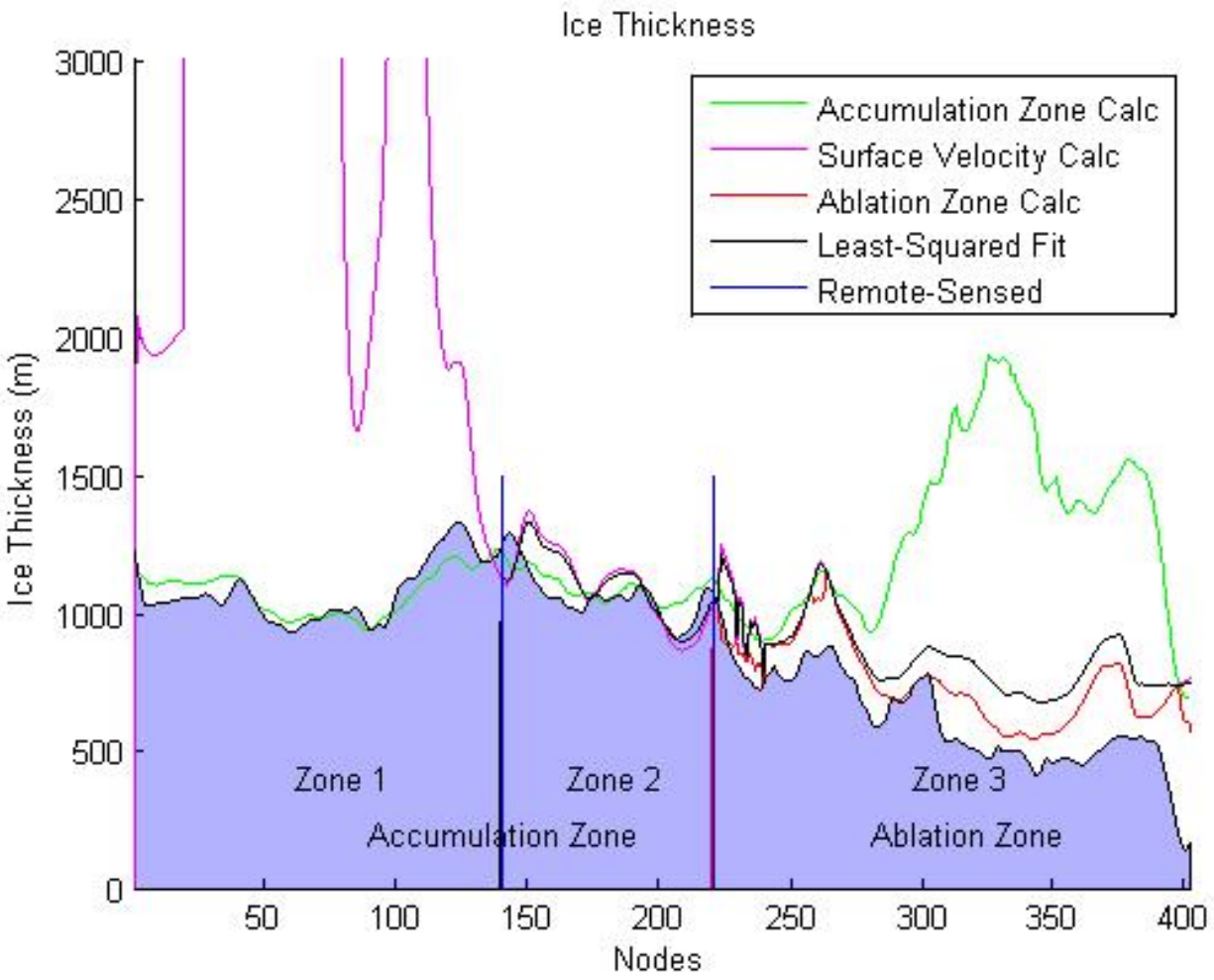

Figure 9.2: Ice thickness calculations assuming no sliding

As expected, these equations do not converge to the remotely-sensed observational data provided that the sliding is neglected. We see in region three that both solutions begin to diverge as a result of the ignored sliding component at the ELA. In this region, equation 8.12 is used to calculate ice thickness where the difference can be considered attributable to basal sliding. Thus, we have developed a way to derive the basal sliding velocity and bedrock elevation wherever we have a temperate bed.

Figure 9.3 plots the difference between the calculated ice thickness (using Figure 9.2) and the remotely-sensed data within the ablation zone (nodes 220-401). The noise was smoothed using a fifth-order polynomial fit, as described previously. Figure 9.4 shows the remotely-sensed ice thickness data plotted with the best calculated fit derived from a least-squares fit. Though a least-squares fit was performed, it was found that the accumulation zone equation (equation 8.10) uniformly conformed better to the remotely-sensed solution. Likewise, the ablation zone equation (equation 8.12) fit best in the ablation zone. Again, the solutions diverge in the ablation zone since sliding is assumed to be zero.

By looking at equations 8.8 and 8.9, the discrepancy of the calculated solutions from the remotely-sensed solutions is assumed to be attributable to sliding, since the additive sliding velocity term, u_{bi}, was set to zero. As sliding is introduced, the calculated ice thickness, H, will decrease in order to maintain constant surface velocity. Thus, it is reasonable to see an overestimate for the value of ice thickness if sliding velocity is forced to zero in the ablation zone. As the discrepancy increases, the relative fraction of sliding to deformational velocity increases. In other words, if the surface velocity of the ice is viewed to move greater than the

threshold of deformational velocity, the remaining velocity component is assumed to be attributable to sliding.

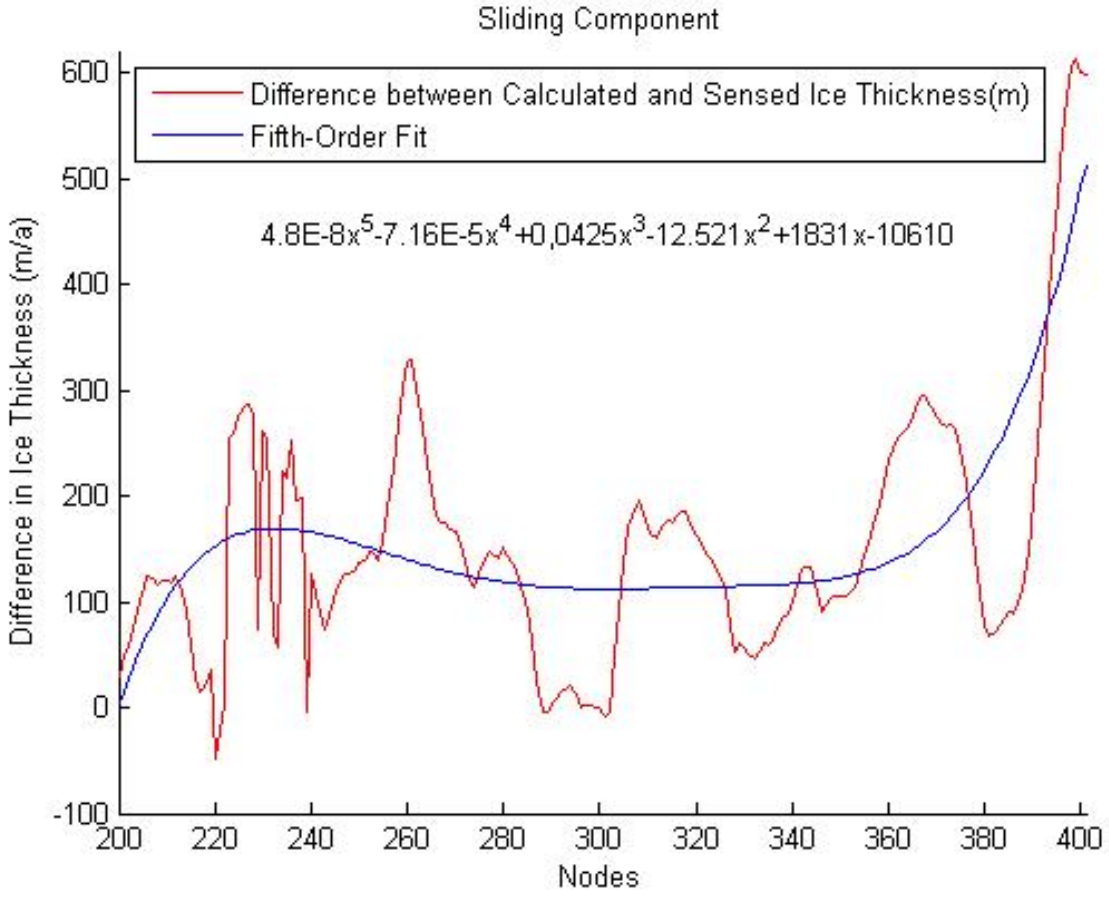

Figure 9.3: Difference between calculated and remotely-sensed ice thickness in the ablation zone. The relative difference is shown in Figure 9.4. The red line shows the difference between the calculated ice thickness (using equation 8.12) and the remotely-sensed ice thickness provided by MCoRDS. The blue line shows the fifth-order polynomial fit over these data from node 200 to the terminus.

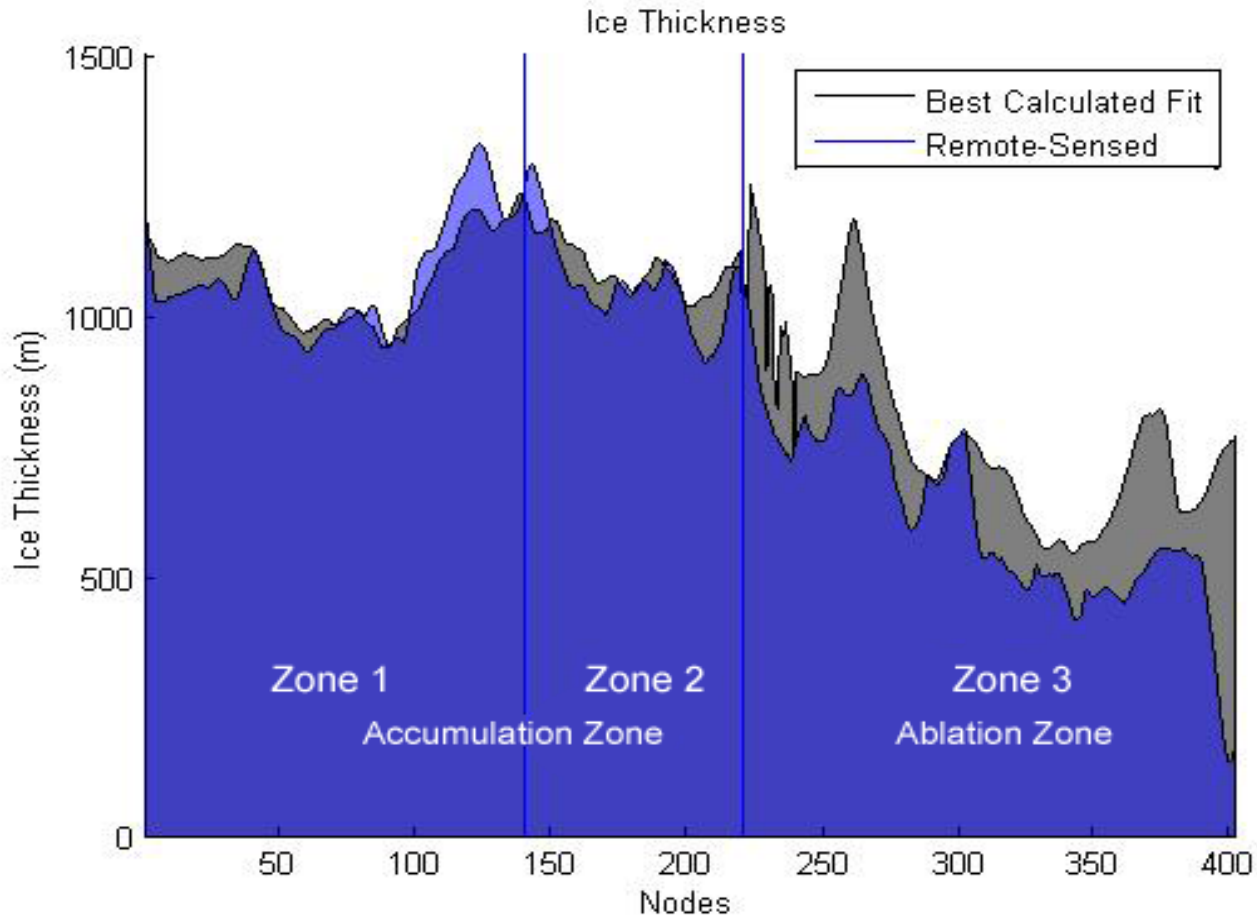

Figure 9.4: Best calculated fit versus remotely-sensed ice thickness data

The magnitude of basal sliding velocity is shown in Figure 9.5 and plotted in relation with the magnitude of velocity attributable to deformation and expressed in terms of meters per year. Data were smoothed with a fifth order polynomial fit. The results expressed in this figure show that a sliding component of velocity quickly arises to about 50% of total glacial motion at the ELA and becomes relatively more dominant closer to the terminus, where sliding contributes nearly all of the glacial motion. The figure also reveals a deformity occurring between nodes 285 and 305 that, as described later, is attributable to a basal topographic feature. Figure 9.6 shows the relative contribution of sliding as a percentage of total glacial velocity in the ablation zone.

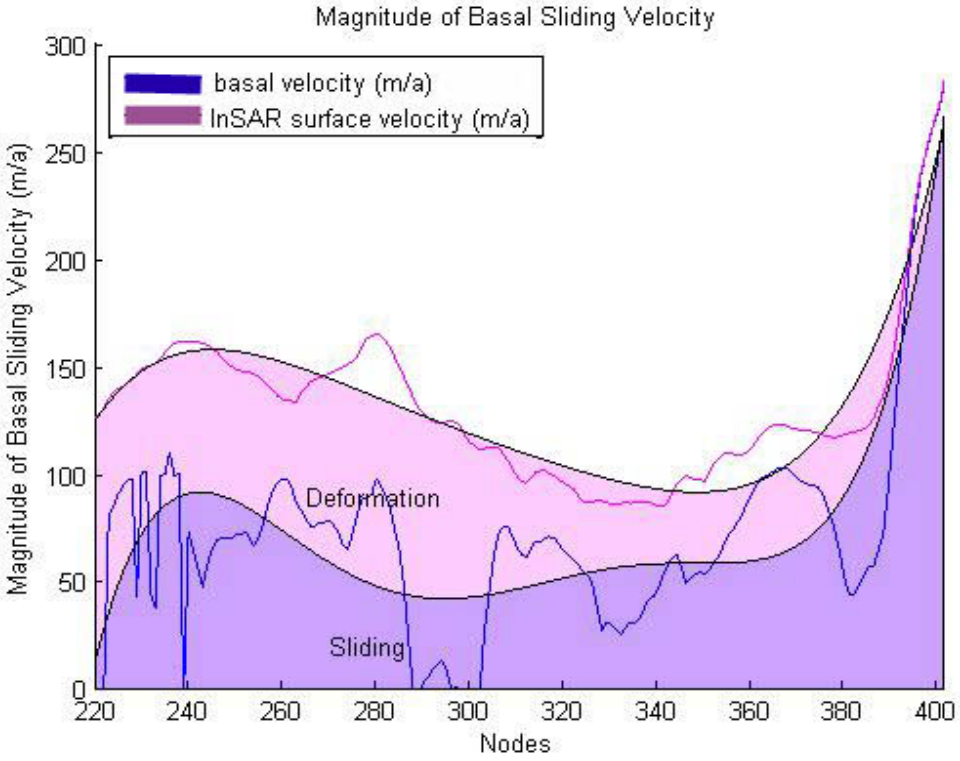

Figure 9.5: Magnitude of basal sliding velocity in ablation zone

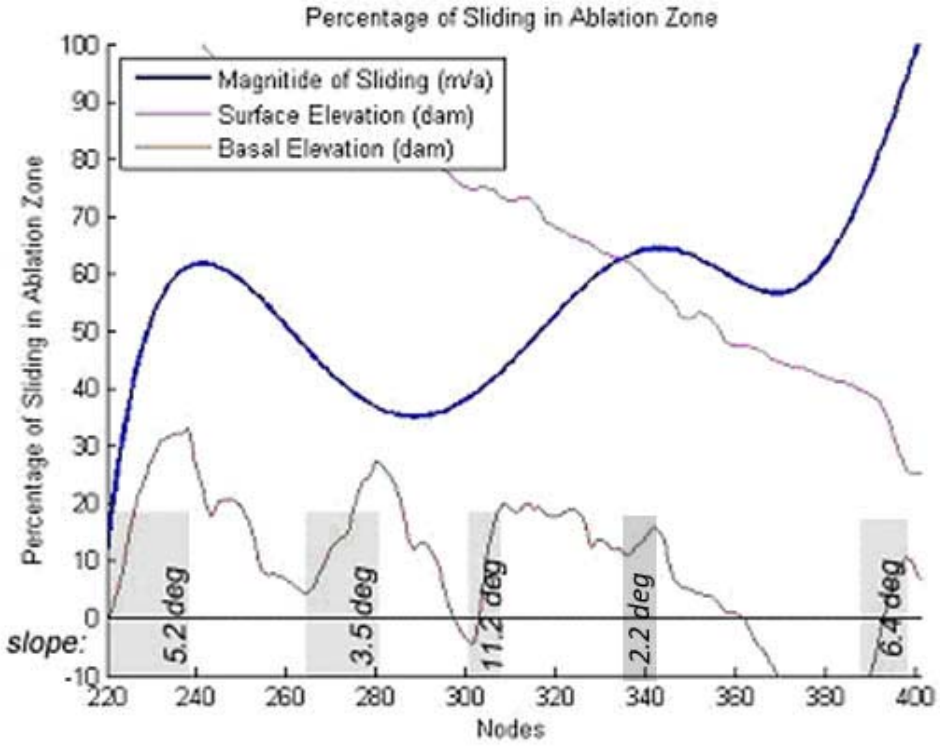

Figure 9.6: Percentage of sliding in ablation zone

Four regions near bedrock topography of increasing slope were analyzed in detail to better quantify the relative effects of bedrock slope on basal sliding. These regions included areas of an increasing basal slope of 3.5 degrees between nodes 242 and 265, 11.6 degrees between nodes 302 and 307, 2.2 degrees between nodes 336 and 342, and 8.2 degrees between nodes 389 and 395. As the span of these regions extends from at least five nodes, this analysis is best applied to spatial scales of at least one kilometer. The variation of width along the flowtube was calculated for each region to see if, by the continuity equation, variations in the width of the flowtube would account for fluctuations in the surface velocity. Since the variation of width between the bounding flowlines in each of the four regions was approximately 0.1%, they were considered negligible. Next, as the analysis is on a flowline, it is assumed that there is no component of transverse velocity and that all velocity is longitudinal. The variation in longitudinal surface velocity was also observed to be about 1.5% and was considered negligible. As an example, the data values of region two for the relevant variables throughout the nodes of interest are summed in Table 9.1.

Node	**301**	**302**	**303**	**304**	**305**	**306**	**307**	**308**
slope (deg)	0	2	29	21	24	19	9	7
v (m/a)	117	115	115	115	115	115	115	115
dist (m)	222	220	220	219	217	216	215	215
W (m)	4014	4012	4009	4012	4014	4009	4010	4010
h_s (m)	749	749	751	751	749	746	737	732
h_b (m)	-45	-40	25	72	125	167	187	201
T (m)	794	789	726	679	624	579	550	530
Percent	100%	99%	91%	86%	79%	73%	69%	67%

Table 9.1: Analysis of basal slope increase region between nodes 301 and 308.

As ice is, of course, considered incompressible and there is no observable expansion or surface velocity increment, it must be assumed that:

1. basal slope drives variance in local stress gradients,
2. local stress gradients drive the relative translation of ice through deformational velocity,
3. the percentage of ice thickness change along the flowline that results from an increase of bedrock elevation is proportional to the relative change of the percent contribution of sliding velocity to the overall glacial velocity. This likely results from an increase in normal force (impeding sliding) that drives an increase in longitudinal stress that drives deformational velocity). Thus, areas of increased compression cause a degree of sliding velocity to be exchanged for a corresponding degree of deformational velocity.

This correlation between the percentage of sliding in the ablation zone and the bedrock slope is shown in Figure 9.7, where both surface and basal elevations are plotted with the calculated magnitude of sliding, and in Figure 9.8, where basal slope is platted with total surface velocity and sliding velocity.

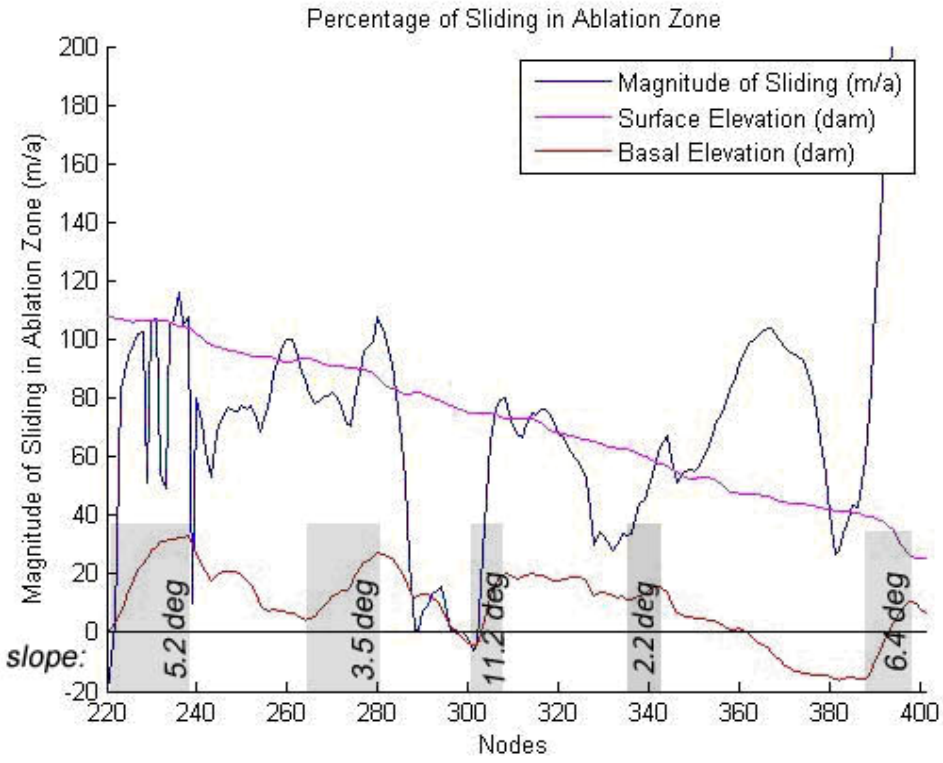

Figure 9.7: Percentage of sliding in ablation zone relative to basal slope

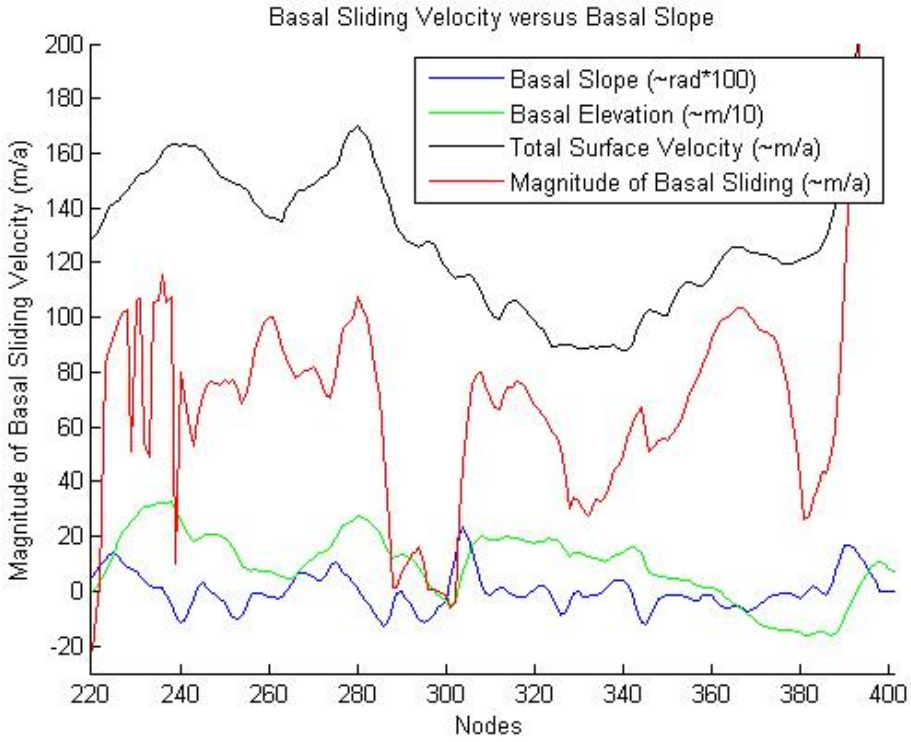

Figure 9.8: Surface velocity and percentage of sliding in ablation zone.

The regions of increasing basal slope were analyzed separately. The first region spanned nodes 242 through 265 where an increase of terrain of approximately 3.5 degrees was observed immediately downstream from node 265 through 280. If the calculated magnitude of sliding was averaged as to smooth out the effects of the basal roughness, then sliding would be estimated to contribute about 90 m/a of the observed surface velocity of 140 m/a. The local topography, however, appears to reduce the relative contribution of sliding from 62% to 55% of total observed surface velocity, or by 11%. The second region spanned nodes 289 through 304 where an increase of terrain of approximately 11.6 degrees was observed from node 302 through 307 and sliding was estimated to contribute about 100 m/a of the observed surface velocity of 120 m/a. The local topography of the second region appears to reduce the relative contribution of sliding from 83% to 4% of total velocity, or by 95%. The third region spanned nodes 329 through 337 where an increase of terrain of approximately 2.2 degrees was observed from node 336 through 342 and sliding was estimated to contribute about 70 m/a of the observed surface velocity of 90 m/a. The local topography of the third region appears to reduce the relative contribution of sliding from 78% to 33% of total velocity, or by 55%. The fourth region spanned nodes 381 through 387 where an increase of terrain of approximately 8.2 degrees was observed from node 389 through 395. Here, sliding was estimated to contribute about 90 m/a of the observed surface velocity of 120 m/a. The local topography of the fourth region appears to reduce the relative contribution of sliding from 75% to 30% of total velocity, or by 60%. These results are tabulated in Table 9.2.

Region	Range of Analysis (Nodes)	Local Magnitude of Basal Sliding (m/a)	Averaged Magnitude of Basal Sliding (m/a)	Averaged Magnitude of Surface Vel. (m/a)	Range of Increasing Slope (nodes)	Slope Magnitude (deg)	Relative Decrease of Sliding Velocity
1	242 to 265	80.0	~ 90	~ 145	265 to 280	3.5	11%
2	289 to 304	5.5	~ 100	~ 120	302 to 307	11.6	95%
3	329 to 337	31.7	~ 70	~ 90	336 to 342	2.2	55%
4	381 to 387	36.3	~ 90	~120	389 to 395	8.2	60%

Table 9.2: Relative decrease of sliding velocity at analysis areas of increasing basal slope.

It is assumed that the relative decrease of sliding velocity in each of these four regions results from the effects of ice compression upstream of the basal elevation increase that drive internal stresses and thus deformational motion. The increase of stresses normal to the bedrock impedes sliding motion while the increase of internal stresses drives deformational velocity. Thus the total ice velocity appears constant at the surface, though the variations of internal stresses create changes of the relative contributions of deformational and sliding velocity components. This implies that internal stress may vary significantly within the glacier due to variations of bedrock topography without creating much variation in the observable surface velocity. Figure 9.9 shows the relation of bedrock slope and the relative decrease of sliding velocity for each of the three regions where bedrock slope was in excess of 2.5 degrees. The datapoint derived from the area of basal slope of 2.2 degrees appeared as an outlier and was not considered, since it was assumed that there would be a threshold value where basal slope begins to drive the internal stresses that drive deformational velocity in lieu of sliding velocity. Thus, we assume that a threshold exists below which sliding velocity remains generally unaffected. Though the data points are too few to draw a strong correlation, there appears to be a positive correlation relating the relative decrease of sliding velocity to bedrock slope up to a twelve-degree bedrock slope, where deformational velocity constitutes nearly 100% of all observed surface velocity. From these limited data points observed, there seems to be a ten-percentage decrease of sliding velocity for every degree of basal slope increase past a threshold bedrock slope of approximately 2.5 degrees. This observation seems to indicate that at shallow slopes (less than 2.5 degrees), the flow rates may be dominated by upstream or downstream processes and associated longitudinal coupling, and at greater slopes (greater than 2.5 degrees), sliding velocity becomes strongly influenced by basal slope. This is speculation as more data points would be required to draw a more definitive conclusion.

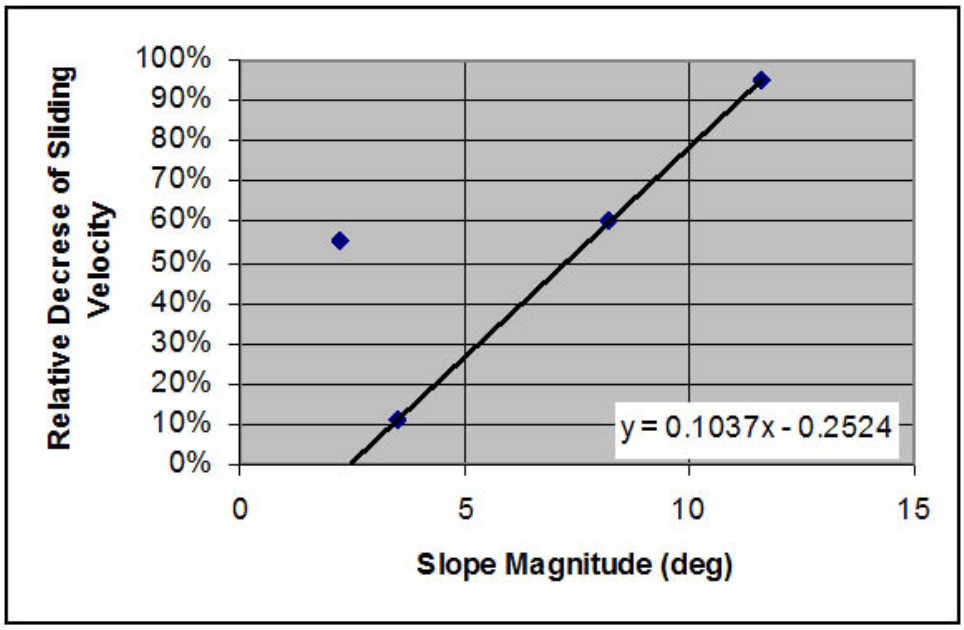

Figure 9.9: Relative decrease of sliding velocity versus bedrock slope magnitude (the datapoint derived from the area of basal slope of 2.2 degrees was considered in the trending as it was considered 'below the threshold' of slope magnitude)

9.2 Sliding Fraction Sensitivity Analysis

An analysis was performed to determine the sensitivity of the ratio of sliding to deformational velocities to various dependent parameters. First, the ranges of instrument error, model error, and interpolation error were identified. Instrument error was present in all data sets used in this study including measurements of surface and basal elevation, surface velocity, and mass balance. Model error is present in all variables including the above listed variables and width. Interpolation error was introduced when fitting all variables to the nodes of analysis along the flowline.

Next, bounds were placed upon the variables where the error was not well defined and a sensitivity analysis was performed. Such variables included the flow parameter, surface mass balance, and the basal elevation. The flow parameter has been based on models and laboratory analogs and as such is still defined with significant uncertainty. The surface mass balance has significant error resulting from a sparse distribution of weather stations with snow accumulation sensors. The basal elevation also contains a lot of error because many assumptions were made in interpolating the ice-penetrating radar data from the grid of Operation Ice Bridge overpasses.

For each of these three sensitivities, a reasonable range of error was first chosen. Values of up to a 40% variation were modeled for the flow parameter, a 30% variation for the surface mass balance, and up to a 20% variation for the basal elevation [Phillips, personal conversation 2011]. Though error values for basal elevation and mass balance were provided, the confidence of these values was low, so the sensitivity analysis was extended beyond the published error of these data sets. After the ranges of sensitivities were identified, a Monte Carlo-like simulation

was performed where the model was run using 50 randomly chosen values of each variable. Linear distributions of randomized numbers were used that were bounded by the range of error chosen for each variable in the sensitivity analysis. The results of these iterations were plotted together to see if the natural dispersion of the sensitive variables significantly affected the results and if so, which variables would influence this the most.

Error data for surface elevation and surface velocity were well documented and summarized in sections 9.2.1 and 9.2.2. Bedrock elevation error data along the flightlines are summarized in section 9.2.3, though the interpolation of these data onto the nodes of analysis introduces a large amount of interpolation error, so bedrock elevation is treated as a sensitivity bounded by 20%. Surface mass balance error and width error is described in section 9.2.4 and 9.2.5 respectively. The flow parameter is considered a sensitivity as described in section 9.2.6.

9.2.1 Surface Elevation

Surface elevation (h_s) was derived through data obtained from both the SPOT and ICESat satellites. Data from the 2009 DEM derived from the SPOT 5 satellite were used to obtain the 2009 surface elevation, which was then scaled to the 2005 reference year using the change of surface height data provided by successive overpasses of the ICESat satellite. For both SPOT 5 and ICESat, error at each node along the flowline was calculated through an understanding of the instrument error, model error, and interpolation error. The instrument error derives from knowledge of the vertical accuracy and the position error of the instrument. The interpolation error is the error associated with the averaging of observations with the standard grid. The model error is the error associated with the averaging of data values assigned to gridpoints to flowline nodes.

SPOT 5:

The SPOT 5 instrument error consists of an absolute elevation accuracy of 10 m for 90% of data points for a slope of less than 20°. Surface slopes in excess of 20° incur greater magnitude of error in surface elevation observations, though it has been assumed that surface slopes in the region of interest are less than 20°. In addition to the absolute elevation accuracy, the absolute location error was used to determine the component of error that is attributable to the spacecraft's ability to accurately geolocate the observation. SPOT 5 has an absolute location error of 30m to one sigma (source: www.spotimage.com). This absolute location error affects the surface elevation depending on the surface slope at the observation and was calculated from the surface slopes at each node of analysis. For sections of ice with little visible contrast, we assume the magnitude of error to be greater than the values of Table 9.3. But we assume the values to be valid in the area of analysis due to the visible contrast of the exposed terrain.

Parameter	**Values**
Absolute elevation accuracy	10 m @ 90% for a slope < 20°
Absolute planimetric accuracy	15 m @ 90%
spatial footprint	65m
along track resolution	170m
Absolute location error	30m to one sigma
Relative internal distance accuracy	0.5 x 10^-3 to one sigma
Resolution:	2 panchromatic at 5m used to generate a 2.5m product. 3 multispectral used to generate 10m product 1 SWIR at 20m
Sampling step	1 second of arc (~ 30 m at the equator, varying according to latitude)

Table 9.3: SPOT Satellite Technical Data (source: www.spotimage.com)

ICESat and ATM:

ICESat and ATM data were used to approximate the surface elevations along the flowline for the period of analysis of 2005-2006. As ICESat obtains laser altimetry data from a spaceborne platform, the data is more comprehensive across the Greenland Ice Sheet and also more equally distributed. ATM obtains data from an airborne platform and is more concentrated in application but benefits from greater range resolution.

Since the DEM generated from the SPOT 5 data was derived from 2009 surface elevation data, the expected change of surface elevation (dH/dt) between the 2009 DEM observation year and the 2005 analysis year was calculated from ICESat and ATM data [Zwally et al., 2010] and the SPOT DEM was then adjusted for these changes, assuming a linear trend. The ICESat and ATM overpasses in the ROI were then plotted along with the central flowline (Figure 8.5) and the dH/dt data were identified at the points of intersection where multiple year data exist. The ATM data was further used to validate the ICESat dH/dt data.

As ICESat provides laser altimetry, the ICESat error data is derived from error in the ability of space-based LiDAR to discern the surface elevation accurately. The absolute elevation accuracy derives from changes in the laser path length resulting from factors such as beam spreading and surface roughness as well as the instruments ability to bin backscattered photons. The absolute location error derives from inaccuracies in pointing from the nadir. The surface elevation error is a summation of the absolute elevation accuracy and the product of the location error and the surface slope:

$$SurfaceElevationError = AbsoluteElevationError + (LocationError * Slope)$$

Based on analysis of surface topography data, we assume the slope to be confined to less than ten degrees [personal communication with Phillips, 2011] and we assume the total surface elevation error of ICESat to be +/- 5.40 m.

The ATM data over Greenland have a reported accuracy of ±10 cm after the DEM data providers [DiMarzio et al., 2007] evaluated the ICESat DEM data set by comparing it to airborne laser altimetry data at intersecting points. A comparison of ATM data in northwestern Greenland indicated that ATM elevations are generally lower than the elevations produced by ICESat with the overall mean difference between the ATM and ICESat-derived DEM data determined to be -41 cm with an error range of ±44 cm, though this mean difference varies with slope as regions with <0.1° slopes, the mean difference is -32 ±43 cm. For regions with 0.1° to 1.0° slopes, the mean difference is -66 ±61 cm [Krabill et al., 2002]. Because of the low error of the ATM data relative to the ICESat data, the ATM data was preferred wherever data from both sources were available.

9.2.2 Surface Velocity

Error estimates for all non-interpolated radar-derived velocity vectors (v_x, v_y) include the statistical uncertainty associated with the phase and speckle tracking error and were provided along with the velocity measurements [Joughin et al., 2010]. Calculated errors are generally small (<5 m/yr) but can be larger in interior areas away control points derived from rock on the coast or balance velocities near the divides and overstated near shear margins and other areas with strong velocity gradients. It is important to recognize that velocity estimates are only relative and are subject to tilt errors, which is the uncertainty of the slope of each pixel and produced by uncertainties associated with both spacecraft attitude and ice surface roughness, since no anchor points are available and InSAR approximates surface slope as a means to better

refine surface velocity measurements. To make absolute velocity estimates and improve accuracy, ground control points are needed to accurately determine the baseline and unknown phase constant. In Greenland the ice sheet is surrounded by mountains and it was possible to estimate the baseline using ground-control points from stationary ice-free areas [Joughin, et al, 2002].

The total velocity error associated at each node of analysis contains components of instrument error (ε_{inst}), model error $(\varepsilon_{\mathrm{mod}})$, and interpolation error $(\varepsilon_{\mathrm{int}})$. Model error estimates were provided at each gridpoint through the National Snow and Ice Data Center (NSIDC) for all non-interpolated radar-derived velocity vectors. These estimates include the statistical uncertainty associated with the phase and speckle tracking error. Formal errors agree reasonably well with errors determined by comparison with GPS data but underestimate the true uncertainty in several ways [Joughin et al., 2002]. Interpolation error is introduced as surface velocity values are interpolated to the nodes along the flowline. As surface velocities are provided in a grid format of 500m x 500m spacing, interpolation error is present at up to 70.7% the difference between the values of the adjacent data points. The total velocity error is treated randomly and summed as a root mean square:

$$TotalError = \sqrt{\varepsilon_{inst}^{\ 2} + \varepsilon_{\mathrm{mod}}^{\ 2} + \varepsilon_{\mathrm{int}}^{\ 2}}$$

9.2.3 Bedrock Elevation

Error in bedrock elevation (z_b) plays a direct role in the determination of the contribution of sliding in the glacial dynamics. If the bedrock elevation is reduced, sliding will be increased since there is less ice to deform. Sliding is also a function of the roughness of the bedrock. If the surface is flat, the ice will move faster. Total error associated with the MCoRDS depth sounder derives from both the depth resolution and the dielectric error. The depth resolution for a flat surface is determined by the bandwidth of the system:

$$\frac{k_t c}{2B\sqrt{3.15}} = 6.8 \text{ meters} \qquad \text{(eq 9.7)}$$

where $B = 20$ MHz is the bandwidth (140 to 160 MHz), 3.15 is the dielectric constant of ice, c is the speed of light in a vacuum, and $k_t = 1.6$ is due to the application of a hanning time-domain window to reduce the range sidelobes of the chirped transmit waveform.

The dielectric error is expected to be on the order of 1% for typical dry ice and no compensation has been done for a firn layer in SAR processing. The dielectric error associated with the ice thickness measurements can be expressed using the first term of the Taylor series [personal communication with Paden, 2011].

$$\Delta T = \frac{-T}{2}\varepsilon_{\%\text{error}} = \frac{-T}{200} \qquad \text{(eq 9.8)}$$

For an ice thickness of T = 2000, a 1% dielectric error creates a 10 m thickness error.

The actual error observed through crossover analysis is significantly greater than the sum of these two error components due largely to the effects of the rough surface. The actual target location is ambiguous for a rough surface since the off-nadir returns in the antenna footprint can hide the nadir return. Thus, the accuracy was best determined through a crossover analysis using intersecting flight paths within the region of interest [Krabill et al., 2007]. Based on a large set of data accumulated in both Greenland and Antarctica, the MCoRDS root mean square cross-over thickness error was determined to be 27.380499 m and the root mean square cross-over thickness error was determined to be 12.614580 m, based on the 2009 Operation Ice Bridge Antarctic campaign.

Parameter	**Values**
Frequency	150MHz (compressed pulse length = 60ns)
Sensitivity	>3km of cold ice
depth resolution	6.8m
along-track resolution	25 m
sample spacing	14 m
cross-track resolution (smooth)	395 m
cross-track resolution (rough)	434 m
dielectric error	10 m at 2000m ice thickness

Table 9.4: MCoRDS Technical Data

From 2006 through 2008, there occurred eight crossover locations of the flowline of this analysis, as shown in Figure 8.5. Interpolation error affects nodes closer to intersecting flightlines less than those farther.

9.2.4 Surface Mass Balance

The surface mass balance distribution (b) of the Greenland Ice Sheet was proposed by several authors using various means. Notable results include Fausto et al (2009), Box et al. (2004), Box and Steffen (2001), and Ohmura (1990). In this analysis, mass balance data was obtained from summing the accumulation data from Burgess [Burgess et al, in press] with the ablation data from Fausto [Fausto et al, 2009] and given in terms of meters per year. The data from Burgess and Fausto were obtained from analytical models that were updated and validated through in-situ data obtained through a network of weather stations and were chosen because of the relative higher resolution compared to the 24km resolution of the data set produced by Box. Further, due to the higher resolution of the Burgess data set, we neglect the interpolation error and assume the error associated with the surface mass balance data at the nodes to be produced exclusively by instrument error and interpolation error. The surface mass balance was treated as a sensitivity to this analysis with a range of +/- 15%, per recommendation of Phillips.

9.2.5 Width

Width (W) at each node was determined by selecting the bounding flowlines along with the central flowline. The local azimuth of the flowline at each node was calculated and a track orthogonal to the flowline was calculated. The locations of the intersections of these tracks and the bounding flowlines were calculated. Error in width was calculated from the resolution of the grid of points surrounding the terminus of Sermeq Avannarleq from where the flowlines were backtracked. The error associated with accurately geolocating the intersections of the orthogonal tracks and the bounding flowlines was calculated to be 35m, leading to a total error associated with the local determination of flowtube width to be 70m. As the flowtube ranges in width from 3655m to 5194m closer to the terminus, the relative percentage of error ranges from 1.348% to 1.915%. The median width is 3948m, or 1.773%. Error associated with the direction of the flowline was considered random and was thus neglected.

9.2.6 Flow Parameter

The flow parameter (A) is considered a sensitivity rather than a source of error in this analysis and a function of the local ice temperature and the presence of Wisconsan ice. Wisconsan ice is a term used to describe the lowest level of ice that was deposited during the ice advance of the Wisconsan Ice Age. This ice has a different chemical and structural composition leading to a reduced viscosity due to the colder climate in which the ice was created and a corresponding increase in the deformation of the ice. Ice temperatures were depth-averaged at each node of this analysis. It is assumed that the viscosity exponent, n, is 3.0 [Nye, 1953].

The flow parameters assigned to the flowline nodes were derived from the flow parameters used in the analysis presented by Phillips et al. [2011] along a flowline from the divide to the terminus of Sermeq Avannarleq. As this flowline differs from the flowline of this analysis, the assumption was made that the flow parameter at each node is identical to the flow parameter calculated along ice of equal surface elevation. Since the flow parameter is a function of ice temperature, the presence of Wisconsan Ice, and the experimentally determined 'n-value', and is considered to contain assumptions that lead its value to be treated with a significant degree of uncertainty, the depth-dependent temperature profile and the Wisconsan Ice model was assumed from the models of Phillips et al. [2011] and the generally accepted 'n-value' of 3.0 was assumed. If Wisconsan ice is present in the lower part of the glacial ice, the flow parameter is generally depth-averaged to values spanning between 2.0E-16 and 4.0E-16, with 3.0E-16 being commonly accepted [Blatter, 1998; Patterson 1994], and in accordance with Phillips et al. [2011]. The flow parameter was then bounded conservatively by +/- 30% and considered a sensitivity in this analysis.

9.3 Sensitivity Analysis Summary

The variables of equations 8.8, 8.10, and 8.12 are listed below in Table 9.5 along with the source of the data and the error that was provided or calculated. The absolute surface elevation error from SPOT 5 was given to be 10m. By geolocating these data with data provided by ICESat and ATM overpasses, the DEM surface elevation error was reduced to 0.5m for the 2009 observation year. An additional error of +/- 0.20m was introduced as the surface elevation data for the 2005 reference year was backtracked, yielding a total error of 0.7m. For comparison, established measurement requirements are tabulated in Table 9.6.

The flow parameter (A), surface mass balance (b_i), and the basal elevation (h_z) were chosen as the dominant uncertainties because the associated errors of each were not nearly as quantified as the errors associated with the other sources of data, and it was upon these variables that the sensitivity analysis was performed. The flow parameter carries large uncertainty in the distribution of temperature and ice composition and its role in affecting the viscosity of the ice. The surface mass balance data is prone to significant model and interpolation errors associated with sparse and irregular distribution of data collection sources, and the basal elevation data carries interpolation error resulting from the inability of the flightlines to cover all areas of the ROI. As attention was focused on areas of greatest uncertainty, the error of known data sources was fixed and reasonable bounds were established for the three parameters of greater uncertainty.

Parameter	Source	Error
Surface Elevation (hs) DEM Absolute error	SPOT Satellite	10.39m (source: www.spotimage.com)
Surface Elevation (hs) Laser Altimeter	ICESat/ / ATM	0.5 m (as explained in text)
Surface Elevation Correction (delta hs)	ICESat	+/- 0.20 m [Zwally et al., 2011]
Combined Surface Elevation (hs)	Combined form SPOT and ICESat	**+/- 0.7 m** (not random) Sigma=1.645(90%)
Basal Elevation (hb)	MCORDS	**6.7m** [Krabill et al., 2007] 7% to 20% assumed
Surface Velocity (vx, vy)	InSAR Satellite	**0.66% to 4.37%** [Joughin et al., 2010]
Width (w)	Calculation from InSAR data	70m or **1.773%** (model error)
Flow Parameter – Temperature	Phillips et al, in press	Assumed Fixed
Flow Parameter – Wisconsan ice	Phillips et al, in press	Assumed Fixed
Flow Parameter – 'n'	Assumed 3.0	None assumed
Mass Balance - Accumulation	Burgess et al, in press	**15% assumed**
Mass Balance - Ablation	Fausto et al, 2009	**15% assumed**

Table 9.5: Sources and errors associated with key variables

Measured ice parameter	Required accuracy	Spatial sampling	Sensor
Ice thickness	5 m	100 m survey 10 m hi-res	Wideband VHF Sounder
Wet or frozen base	95% confidence	100 m pixel	Monostatic and bistatic VHF SAR
Basal water Layer thickness	50% or better 4 mm to 0.5 m	100 m survey 10 m hi-res	Monostatic and bistatic VHF SAR
Internal layer depth and geometry	10 cm at surface 5 m at base	100 m survey 10 m hi-res	Wideband VHF depth Sounder and UHF radar
Bottom topography	5 m	100 m survey 10 m hi-res	Wideband VHF depth Sounder
Surface topography	0.5 m	100 m survey 10 m hi-res	In SAR, Radar/Laser Altimeter, GPS
Surface velocity	5% in speed 5° in direction	500 m grid	Interferometric SAR (RADARSAT-1)

Table 9.6: Science measurement requirements.

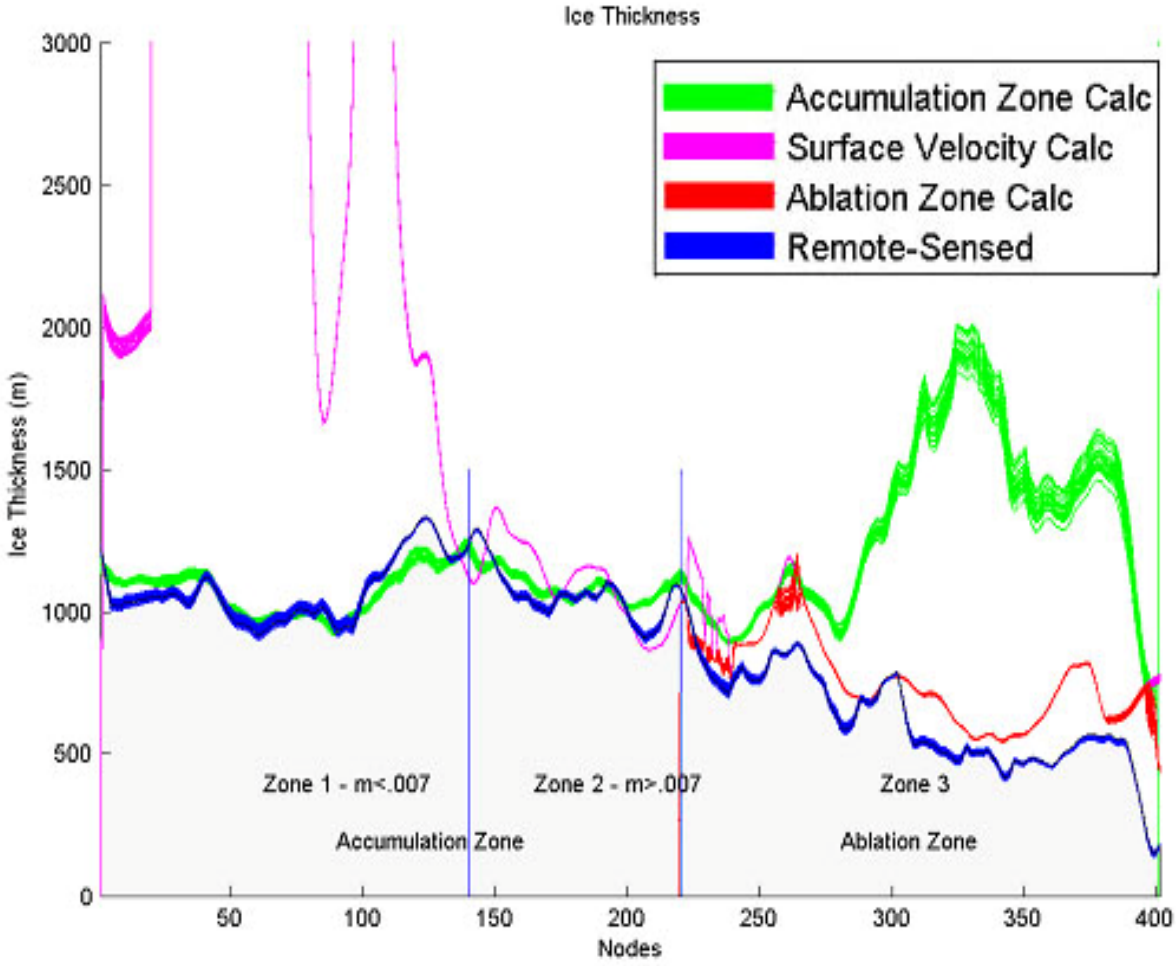

Figure 9.10: Monte Carlo Distribution: z_b error = 7%, A error = 0%, b_i error = 15%. This figure is the same as Figure 9.4 but shows the distribution of fifty randomized Monte-Carlo-like iterations calculating the ice thickness derived from the accumulation zone equation (eq. 8.10), the surface velocity equation (eq. 8.8), and the ablation zone equation (eq 8.12). The accumulation zone spans zone one and two where zone one is characterized by surface slopes less than 0.07 degrees while zone two is characterized by surface slopes greater than 0.007 degrees.

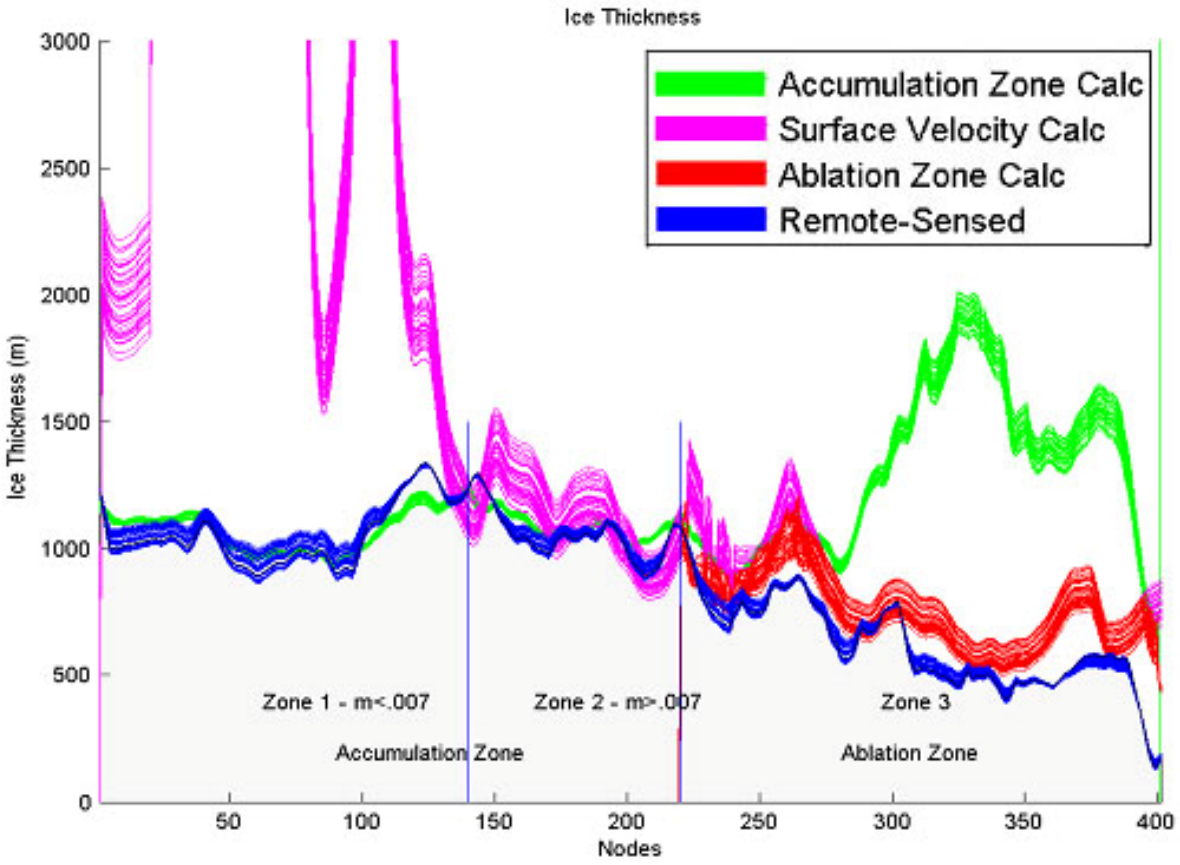

Figure 9.11: Monte Carlo Distribution: z_b error = 20%, A error = 40%, b_i error = 15%. This figure is the same as Figure 9.4 but shows the distribution of fifty randomized Monte-Carlo-like iterations calculating the ice thickness derived from the accumulation zone equation (eq. 8.10), the surface velocity equation (eq. 8.8), and the ablation zone equation (eq 8.12). The accumulation zone spans zone one and two where zone one is characterized by surface slopes less than 0.07 degrees while zone two is characterized by surface slopes greater than 0.007 degrees.

A quantitative summary of the sensitivity analysis is shown below in Table 9.7. Various permutations of error multipliers are listed along with the Monte Carlo results within both the accumulation zone and the ablation zone. Error multipliers define the bounds of uncertainty that were established based on reasonable assumptions of bounding cases for each of the three variables onto which the sensitivity analysis was performed. In the Monte-Carlo analysis, values of each sensitivity were randomly selected based upon a randomized linear distribution spanning from the mean value minus the product of error multiplier and the mean value to the mean value plus the product of the error multiplier and the mean value. Thus, there is an equal possibility for the Monte-Carlo analysis to select any value that lies between these two extremes.

The mean difference (mean diff) is defined as the average of the difference between the calculated ice thickness (Hacc) and the remotely-sensed ice thickness (H) of all nodes within the accumulation zone. The mean span of the error of the calculated and the remotely-sensed ice thicknesses in the accumulation zone are expressed as 'Span Hacc' and 'Span H' respectively. These values are the averaged sum of distances between the maximum value and the minimum value of the variable across the nodes of the accumulation zone. It can be shown here that for all permutations of error within the bounds of: (basal elevation +/- 20%, flow parameter +/- 40%, and mass balance +/- 30%), the solutions for remotely-sensed ice thickness and surface calculated ice thickness converge in the accumulation zone and diverge consistently outside of the range of error in the ablation zone, indicating an element of sliding exists in the ablation zone.

The error associated with the flow parameter (A) changes the calculated ice thickness dramatically in the ablation zone. The impact of one percentage increase of error associated with the flow parameter is approximately 1.41m in calculated ice thickness while the impact of a percentage of error increase associated with surface mass balance is approximately 0.29m. This implies that the flow parameter is approximately five times more sensitive than the surface mass balance in determining the ice thickness in the ablation zone. The effect of error in the determination of the basal elevation affects the determination of the remotely-sensed ice thickness by approximately 0.91m per percentage of error. In the accumulation zone, the flow parameter is considered constant and does not play a factor. The impact of a degree change of error associated with basal slope is approximately ten times that of a degree change of surface mass balance.

To most effectively improve the methods in which to accurately calculate the ice thickness through surface observation, an improvement in the accuracy of modeling the flow parameter is advised. As the flow parameter is modeled as a function of ice thickness, ice temperature, and presence of Wisconsan Ice, it would be advised to first invest into methods that could better determine the temperature profiles of ice columns. As this would need to be compared with more accurate measurements of ice thickness, and since interpretation error contributes the most to the overall error associated with basal height, it would be further advised to increase the resolution of field sites that are being mapped with the MCoRDS ice penetrating radar. Ideally, a test site could be used that combines a fine resolution of Ice Bridge overpasses with data from a wide array of in-situ instrumentation that can better determine the inputs to depth-dependent determinations of the flow parameter.

Error Multipliers			Accumulation Zone			Ablation Zone		
Zberror (%)	Aerror (%)	Bierror (%)	mean diff (m)	Span Hacc (m)	Span H (m)	mean diff (m)	Span Hacc (m)	Span H (m)
0.07	0.00	0.15	11.36	35.15	33.85	135.11	9.53	11.69
0.07	0.00	0.30	8.43	37.93	29.39	135.22	11.43	10.59
0.20	0.00	0.30	5.93	38.32	68.51	113.98	11.46	22.39
0.07	0.20	0.15	9.77	33.48	31.23	137.61	37.59	10.95
0.07	0.40	0.15	7.92	32.31	31.09	134.70	66.13	11.06
0.20	0.40	0.15	7.08	31.87	70.34	133.86	36.72	23.20
0.20	0.20	0.30	9.85	36.83	70.08	138.17	40.51	23.05

Table 9.7: Sensitivity Analysis Summary

9.4 Using a Constant Flow Parameter

Model iterations were performed using the generally accepted constant value for the flow parameter of 3.0E-16, which was held constant for all ice thicknesses and does not account for variability of ice temperature or composition. We notice that though this value still provides a valid fit in the accumulation zone (the difference between remotely-sensed data and calculated data is less than the distribution of error from the data sources), the data in the ablation zone shows only a slight discrepancy between the remotely-sensed data and the calculated data. As it is reasonable to expect a significant contribution of sliding to the total glacial velocity, this implies that the ability to determine the temperature and the composition of the ice accurately plays a large role in the ability to characterize sliding through the method presented in this analysis. We see in Figure 9.12 that, although there remains good correlation of ice thickness between the remotely-sensed solution and the calculated solution, there is little difference in the ablation zone that would be attributable to sliding. For a constant value of A:

- Mean difference between the remotely-sensed and calculated determinations of ice thickness in Accumulation Zone is 8.85 m (0.71% of total thickness.
- Range of uncertainty in the calculated ice thickness (H_{acc}) in the Accumulation Zone is 37.93 m (3.03%).
- Range of uncertainty in the remotely-sensed ice thickness in the Accumulation Zone is 70.98 m (5.67%).
- Mean difference between the remotely-sensed and calculated determinations of ice thickness in Ablation Zone is 50.24 m (7.06% of total thickness).
- Range of uncertainty in the calculated ice thickness (H_{abl}) in the Ablation Zone is 31.66 m (4.45%).
- Range of uncertainty in the remotely-sensed ice thickness (h) in the Ablation Zone is 23.49 m (3.30%)

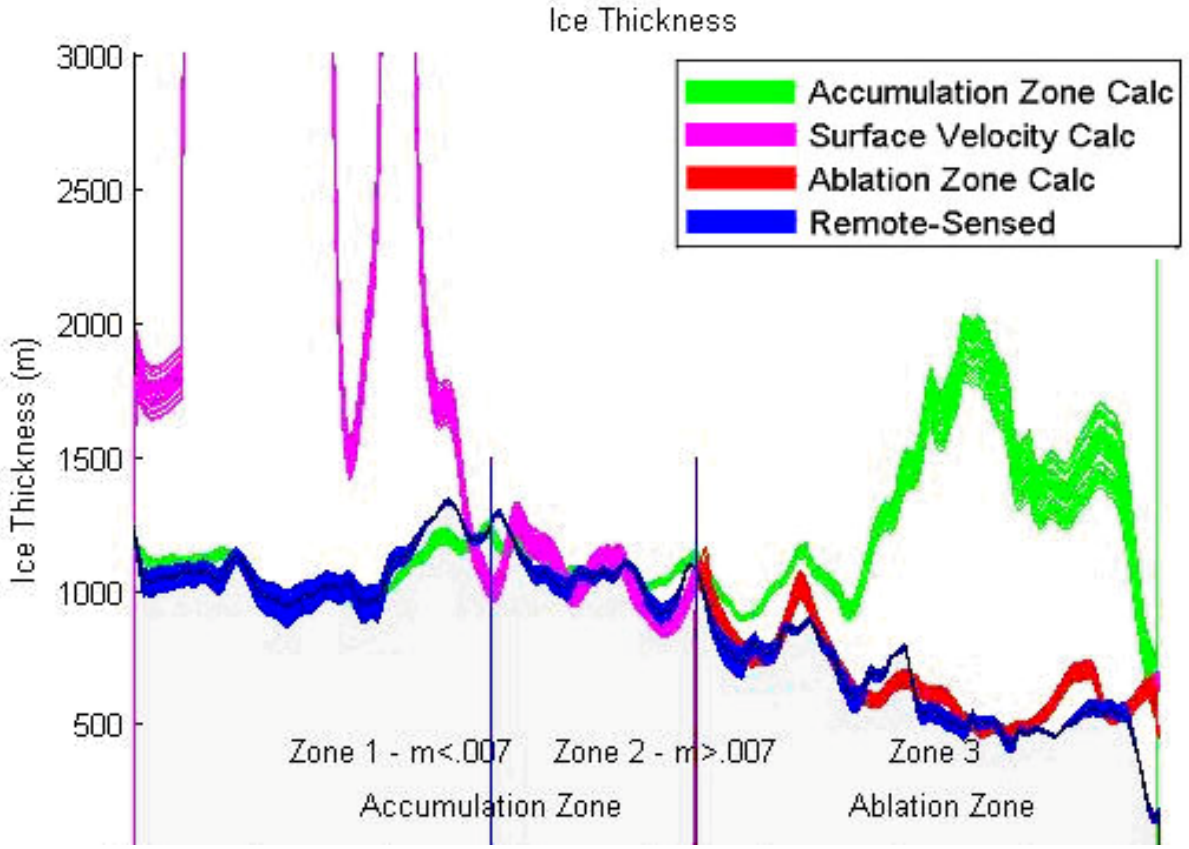

Figure 9.12: Monte Carlo Iterations using a constant flow parameter value of 3.0E-16. This figure is the same as Figure 9.4 but shows the distribution of fifty randomized Monte-Carlo-like iterations calculating the ice thickness derived from the accumulation zone equation (eq. 8.10), the surface velocity equation (eq. 8.8), and the ablation zone equation (eq 8.12).

10. Determining the relative contributions of glacial sliding in Sermeq Avannarleq, Greenland: Conclusions

The following conclusions are made from this study:

1) The sliding component of velocity in Sermeq Avannarleq quickly arises to about 50% of total glacial motion at the ELA and becomes relatively more dominant closer to the terminus, where sliding contributes nearly all of the glacial motion.

2) The effects of basal slope seem to play a strong role in the relative contribution of glacial sliding to overall glacial velocity and suggests a relationship between sliding percentage and basal slope for slopes beyond a minimum threshold, determined to be approximately 2.5 degrees, though it is important to note that this assessment was based on only four observations and more observations would be needed to confirm this hypothesis. The percentage of glacial sliding was found to decrease proportionally to the increase of basal slope up to approximately a 12-degree slope, where deformational velocity contributed to almost all (>95%) of glacial velocity. It is assumed the effects of ice compression upstream of the basal elevation increase drive internal stresses and thus deformational motion.

3) It was found that the accumulation zone equation (equation 8.10) uniformly conformed better to the remotely-sensed solution because it relies more on the surface velocity data provided by InSAR, which has less uncertainty and relies upon fewer assumptions than solutions that rely more upon variables of higher uncertainty (e.g. surface slope and the flow parameter). Likewise, the ablation zone equation (equation 8.12) shows to be effective since a more accurate determination of surface velocity and flux allow for more of the uncertainty to be bounded by the

ice properties (e.g. temperature distribution, Wisconsan ice factor) that comprise the flow parameter.

4) Through the use of accurate and spatially distributed surface velocity measurements derived from InSAR, we could determine the strain fields and could thus sidestep the dependency on the flow parameter and the surface slope that have traditionally played a larger role in glacial modeling. We could then solve for ice thickness using only the surface mass balance and surface velocity data in the accumulation zone and solve for ice thickness using a greater dependence on these observables (which can be validated in the accumulation zone) in the ablation zone. This manipulation circumvented problems that had been faced by MacAyeal in attempting a direct algebraic inversion. The close correlation of the results presented here demonstrates the importance of high-quality inputs such as those from InSAR and thus reduces the relative significance of the flow parameter and the corresponding range of error that bounds the sliding component of velocity.

11. Conclusions

Integrative remote sensing methods are effective in studying large heterogeneous phenomena comprehensively. Unique elements in the study of continental glaciers and noctilucent clouds can be obtained via spaceborne, airborne, in-situ, and ground-based measurements, and key questions can be addressed through the synthesis of these methods. Demonstrated here is the applicability of integrative methods, when applied to noctilucent clouds through the synchronized observations of airborne and spaceborne platforms, to observe similar cloud structure, provide finer detail to common observations, and to extrapolate these observations to lower latitudes and temporal timespans within an orbital period of the spacecraft. The applicability of these integrative methods were also applied to the Greenland Ice Sheet, where the availability of more accurate surface velocity measurements and comprehensive flow parameter data currently available has led to the successful modeling, through direct algebraic inversion, of the relative contribution of glacial sliding, a key component to the understanding of positive feedback in glacial dynamics. Both NLCs and the Greenland Ice Sheet are seen as two critical components to the understanding of global climatological trends.

A synchronized observation of a NLC using an airborne camera and a PMC using spaceborne cameras was obtained on 6 July 2009. Two Canon EOS-30D cameras were integrated to a Mooney M20K research aircraft and flown to a location of 58.32^{o}N, 112.30^{o}W in Northern Alberta, Canada to coordinate with the overpass of the AIM satellite at 06:48GMT. The aircraft was positioned so that imagery would be taken while the sun was at a SDA of 8.5 degrees and then oriented so that the imager would be pointed along the AIM groundtrack. The common-volume imagery obtained from both the CIPS experiment and the aircraft at the time of

the AIM overpass concurrently detected clouds identified by similar band structures. The imagery from the aircraft also shows fine transverse cloud structures not discernable within the CIPS image, implying that greater spatial resolution is achievable through the airborne imagery. Subsequent analysis of the CIPS imagery from the AIM satellite at this location shows a correlation in orientation of the prominent structures in both sets of imagery, showing overlay of prominent features and coincidence of band orientation.

The NLC experiment verified that synchronous imagery of NLC structures could be obtained through use of airborne and spaceborne imagers with about 100 km of spatial overlap between the two images, if the aircraft is flown at least 18000 feet altitude, enabling common features to be extrapolated through the more sensitive and higher-resolution aircraft imagery towards the day-to-night terminator. This capability is most significant as it provides a basis to refine the processing algorithms and detection thresholds of the spaceborne platform at the day-to-night terminator. In future campaigns it is hoped that through more coincident observations of NLCs from polarized and geo-tagged airborne cameras and from successive AIM orbits, we can gain a deeper insight into the temporal evolution of NLC structures and their magnitudes of polarization, which may provide insight into particle shape, and partly address the questions regarding the rapid change in PMC structures seen in successive AIM orbits and give insight into the effect of GWs in PMC formation and evolution.

A glacial analysis was conducted using data from spaceborne platforms, airborne data from the Operation Ice Bridge campaign, and in-situ sensor data to determine the contribution of sliding relative to deformation in the ablation zone near Sermeq Avannarleq, Greenland. This analysis was performed to establish a method from which sliding ratios could be inferred at other

outlet glaciers and to identify where the greatest improvements can be made to observational and modeling techniques.

The glacial analysis showed that the sliding component of velocity quickly arises to about 50% of total glacial motion at the ELA and becomes relatively more dominant closer to the terminus, where sliding contributes nearly all of the glacial motion, and that the percentage of glacial sliding was found to decrease proportionally to the increase of basal slope up to approximately a 12-degree slope, where deformational velocity contributed to almost all (>95%) of glacial velocity. The use of more accurate surface velocity measurements was found to reduce the relative significance of the flow parameter, circumventing problems that had been faced by MacAyeal in attempting a direct algebraic inversion and validating the importance of high-quality inputs such as space-based observations of surface velocity and elevation.

As expected, sliding was found to be initiated near the ELA and to dominate closest to the termini of outlet glaciers. The process is dynamic and dependent on highly-variable parameters such as temperature. As ice warms, we expect glacial sliding to increase due to increased lubrication at the bedrock interface through the mechanisms of penetration or intrusion described previously. Ice thickness is also dynamic. As ice gets thinner, we expect the reduction in the normal force applied by the glacier upon the bedrock to drive an increase in basal sliding. A more detailed determination of the flow parameter and mass balance data through in-situ observations along the flowline would significantly reduce the uncertainty associated with sliding measurements. Ice-penetrating radar data could also be obtained along flowlines determined through InSAR-derived surface velocity profiles, dramatically decreasing

interpolation error associated with the bedrock elevation data. Further, analyses of additional outlet glaciers through similar methods would be expected to further validate these results.

References:

Abshire, J. et al. 2005. Geoscience Laser Altimeter System (GLAS) on the ICESat mission: on-orbit measurement performance. *Geophysical Research Letters* v. 32, L21S02, doi:10.1029/2005GL1024028.

America's Climate Choices: Panel on Advancing the Science of Climate Change; National Research Council (2010). *Advancing the Science of Climate Change*. Washington, D.C.: The National Academies Press. ISBN 0309145880.

Backhouse, T.W., 1885. The luminous cirrus cloud 351 of June and July, *The Meteorological Magazine* 20, p. 133.

Bailey, S.M., Thomas, G.E., Rusch, D.W., Merkel, A.W., Jeppesen, C.D., Carstens, J.N., Randall, C.E., McClintock, W.E., Russell III, J.M., Phase functions of polar mesospheric cloud ice as observed by the CIPS instrument on the AIM satellite, *Journal of Atmospheric and Solar-Terrestrial Physics, Vol. 71, Issues 3-4*, March 2009, Pages 373-380

Bamber, J. L., S. Ekholm, and W. Krabill (1998), The accuracy of satellite radar altimeter data over the Greenland Ice Sheet determined from airborne laser data, Geophys. Res. Lett., 25(16), 3177-3180.

Baumgarten, G., Fiedler, J., Fricke, K. H., Gerding, M., Hervig, M., Hoffmann, P., Müller, N., Pautet, P. D., Rapp, M., Robert, C., Rusch, D., von Savigny, C., Singer, W., 2009a. The noctilucent cloud (NLC) display during the ECOMA/MASS sounding rocket flights on August 3, 2007: Morphology on global to local scales. *Ann. Geophys*. 27, pp. 953–965

Baumgarten, G., Gerding M., Kaifler, B., Müller N., 2009b. A transEuropean network of cameras for observation of noctilucent clouds from 37°N to 69°N, in Proceedings of the 19 th ESA Symposium on European Rocket and Balloon Programmes and Related Research, 711 June 2009, Bad Reichenhall, Germany (ESA SP671). pp. 129-134.

Baumgarten, G., Fiedler, J., Lübken, F.J., von Cossart, G., 2008. Particle properties and water content of noctilucent clouds and their interannual variation. J. Geophys. Res. 113, D06203.

Benze, S., Randall, C.E., DeLand, M.T., Thomas, G.E., Rusch, D.W., Bailey, S.M., Russell III, J.M., McClintock, W., Merkel, A.W., Jeppesen, C., 2009. Comparison of polar mesospheric cloud measurements from the Cloud Imaging and Particle Size experiment and the solar backscatter ultraviolet instrument in 2007. *J. Atmos. Sol. Terr. Phys.*71, pp 365-372.

Blatter, H., G. K. C. Clarke, and J. Colinge (1998), Stress and velocity fields in glaciers: part II. Sliding and basal stress distribution, J. Glaciol., 44(148), 457–466.

Box, J.E.,Bromwich, D.H., Bai, L., Greenland ice sheet surface mass balance 1991–2000: Application of Polar MM5 mesoscale model and in situ data, Polar Meteorology Group, Byrd Polar Research Center, Ohio. *Journal of Geophysical Research, Vol. 109,* D16105, doi:10.1029/2003JD004451, 2004

Box, J.E., Cassano, J.J., Bromwich, D.H., Li, L. and Steffen, K. (2001), Evaluation of Polar MM5 simulations of Greenland's atmospheric circulation, *J. Geophys. Res.*, 106, 33,867–33,889, doi:10.1029/2001JD900044.

Burgess, E.W., Forster, R.R., Box, J.E., Mosley-Thompson, E., Bromwich, D.H., Bales, R.C., Smith, L.C., A spatially calibrated model of annual accumulation rate on the Greenland Ice Sheet (1958–2007). *Journal of Geophysical Research* 115:F2, 2010.

Chandra, C., Jackman, C.H., Fleming, E.L., Russell III, J.M., 1997. The seasonal and long term changes in mesospheric water vapor. *Geophysical Research Letters* 24, 639–642.

Chandran, A., Rusch, D. W., Palo, S. E., Thomas, 374 G. E., Taylor, M., 2009. Gravity Wave observations from the Cloud Imaging and Particle Size (CIPS) Experiment on the AIM spacecraft, *J. Atmos. Sol. Terr. Phys.*

Das, S., Joughin, I., Behn, M., Howat, M., King, M., Lizarralde, D., Bhatia, M., "Fracture Propagation to the Base of the Greenland Ice Sheet During Supraglacial Lake Drainage", *Science* 9 May 2008: Vol. 320 no. 5877 pp. 778-781 *DOI:* 10.1126/science.1153360 .

Deland, M.T., Shettle, E.P., Thomas, G.E., Olivero, J.J., 2006. A quarter-century of satellite polar mesospheric cloud observations, *Journal of Atmospheric and Solar-Terrestrial Physics* 68, pp. 9–29.

DiMarzio, J., A. Brenner, R. Schutz, C. A. Shuman, and H. J. Zwally. 2007. *GLAS/ICESat 1 km laser altimetry digital elevation model of Greenland*. Boulder, Colorado USA: National Snow and Ice Data Center. Digital media.

Donahue, T. M., Guenther, B., and Blamont, J. E.: Noctilucent clouds in daytime: Circumpolar particulate layers near the summer mesopause, J. Atmos. Sci., 36, 515–517, 1972.

Fausto, R.S., Ahlstrøm A.P., Van As, D., Bøggild, C.E., Johnsen, S.J., A new present-day temperature parameterization for Greenland, *Journal of Glaciology, Volume 55, Number 189, February 2009* , pp. 95-105(11).

Fogle, B.B., Haurwitz, 1969. Wave forms in noctilucent clouds, *Deep Sea Res.*

Fritts, D.C., Rastogi, P.K., 1985. Convective and dynamical instabilities due to gravity wave motions in the lower and middle atmosphere: theory and observations. Radio Science, 1247–1277.

Gadsden, M., Parviainen, P., 1995. Observing Noctilucent Clouds. International Association of Geomagnetism and Aeronomy.

Gadsden, M., Schröder, W., 1989. Noctilucent Clouds, Springer, Berlin.

Gadsden, M., 1981. The silver-blue cloudlets again: nucleation and growth of ice in the mesosphere. *Planet and Space Science* 29, pp. 1079–1087.

Gadsden, M., 1998. The North-West Europe data on noctilucent clouds: a survey. *Journal of Atmospheric and Solar-Terrestrial Physics* 60, pp. 1163–1174.

Gerlach, T.M., 2011, Volcanic versus anthropogenic carbon dioxide: Eos Trans. AGU, v. 92, n. 24, p. 201-202.

Grahn, S., Witt, G., 1971. Rep AP-4 Inst Meteorol. University of Stockholm.

Gu YY, Gardner CS, Castleberg PA, Papen GC, Kelley MC., Validation of the Lidar In-Space Technology Experiment: stratospheric temperature and aerosol measurements. Appl Opt. 1997 Jul 20;36(21):5148-57.

Gumbel, J. and Witt, G.,'In Situ Measurements of the Vertical Structure of a Noctilucent Cloud', *Geophysical Research Letters*, Vol. 25, No. 4, pgs 493-496, 1998.

Gumbel et al., 'Scattering phase functions and particle sizes in noctilucent clouds', *Geophysical Research Letters*, Vol. 28, No. 8, pgs. 1415-1418, 2001.

Hemenway C.L., Soberman R.K., Witt G. (1964), "Sampling of noctilucent cloud particles." Tellus 16:84-88.

Hervig, M. et al., 'First Satellite Observations of Meteoric Smoke in the Middle Atmosphere', LPMR presentation, 2009.

Houghton, J.T.,Y. Ding, D.J. Griggs, M. Noguer, P.J. van der Linden, X. Dai, K. Maskell, and C.A. Johnson (eds.) "Climate Change 2001: The Scientific Basis. Contribution of Working Group I to the Third Assessment Report of the Intergovernmental Panel on Climate Change (IPCC)", Cambridge University Press, Cambridge, United Kingdom and New York, NY, USA, 881pp.

'Inventory of U.S. Greenhouse Gas Emissions and Sinks: 1990-2009', U.S. Environmental Protection Agency #430-R-11-005, April 2011.

Jensen, E.J., Thomas, G.E., 1988. A growth-sedimentation model of polar mesospheric clouds: comparison with SME measurements. *Journal of Geophysical Research* 93, pp. 2461–2473.

Joughin, I., B. Smith, I. Howat, and T. Scambos. 2010. MEaSUREs Greenland Ice Velocity Map from InSAR Data. Boulder, Colorado, USA: National Snow and Ice Data Center. Digital media.

Joughin, I., B. Smith, I. M. Howat, T. Scambos, and T. Moon. 2010. Greenland Flow Variability from Ice-Sheet-Wide Velocity Mapping. *Journal of Glaciology*, 56 (197), pp. 415-430, doi: 10.3189/002214310792447734.

Joughin, I. 2002. Ice-sheet velocity mapping: a combined interferometric and speckle-tracking approach. *Ann. Glaciol.,* **34**, 195–201.

Karlsson, B. and M. Rapp (2006), Latitudinal dependence of noctilucent cloud growth, Geophys. Res. Lett., 33, L11812, doi:10.1029/2006GL025805.

Knauss, J. A. (1996). *Introduction to Physical Oceanography*. Prentice Hall. ISBN 0-13-238155-9.

Krabill, W. et al. 2002. Aircraft laser altimetry measurement of elevation changes of the Greenland Ice Sheet: technique and accuracy assessment. *J. Geodynamics* 34, 357-376.

Leslie, R., 1885. Sky glows. *Nature* 32, p. 245.

Lumpe, J. D.; Bailey, S. M.; Carstens, J. N.; Nielsen, K.; Thomas, G. E.; Gumbel, J.; Randall, C. E.; Templeman, B.; Cilke, D.; Russell, J. M.; Rusch, D. W. "Retrieval of PMC Properties From CIPS: Algorithm Description, Error Analysis and Cloud Detection Sensitivity", American Geophysical Union, Fall Meeting 2009, abstract #SA41A-1587

MacAyeal, D.R., Irregular Oscillations of the West Antarctic Ice Sheet, *Nature, Vol. 359,* 3 September 1992.

Marsh, D., Smith, A., Noble, E., 2003. Mesospheric ozone response to changes in water vapor. *Journal of Geophysical Research 108* (D3), 4109.

McClintock, W.E., Rusch, D.W., Thomas, G.E., Merkel, A.W., Lankton, M.R., Drake, V.A., Bailey, S.M., Russell, J.M., 2008. The cloud imaging and particle size experiment on the aeronomy of ice in the mesosphere mission: Instrument concept, design,calibration, and on-orbit performance. 424 *Journal of Atmospheric and Solar–Terrestrial Physics.*

Meese, D. A., A. J. Gow, R. B. Alley, G. A. Zielinski, P. M. Grootes, M. Ram, K. C. Taylor, P. A. Mayewski, and J. F. Bolzan (1997), The Greenland Ice Sheet Project 2 depth-age scale: Methods and results, *J. Geophys. Res.*, 102(C12), 26,411–26,423.

Merkel, A.W., Thomas, G.E., Palo, S.E. and Bailey, S.M. (2003). Observations of the 5-day planetary wave in PMC measurements from the Student Nitric Oxide Explorer Satellite. *Geophysical Research Letters 30(4): doi: 10.1029/2002GL016524. issn: 0094-8276.*

Nye, J.F., The Flow Law of Ice from Measurements in Glacier Tunnels, Laboratory Experiments and the Jungfraufirn Borehole Experiment *Proc. R. Soc. Lond. A 7 October 1953 vol. 219 no. 1139 477-489.*

Ohmura, A., Completing the World Glacier Inventory, Annals of Glaciology 50(53) 2009.

Paterson, W.S.B. *1994*. The physics of glaciers. 3rd edition. Oxford, New York, Tokyo, Pergamon, ix, 480 pp. ISBN 0-08037945.

Philbrick C. R., et al. (1984), Adv. Space Sci. 4, 153.

.

Phillips, Rajaram, Colgan and Steffen: "Observed Rapid Increase in Glacier Flow Velocity caused by Cryo-Hydrologic Warming: Case Study in Western Greenland", 2011, Nature Geoscience, submitted.

Qin, D., Chen, Z., Averyt, K.B., Miller, H.L., Solomon, S., Manning, M., Marquis, M., Tignor M.. "IPCC, 2007: Summary for Policymakers". *Climate Change 2007: The Physical Science Basis. Contribution of Working Group I to the Fourth Assessment Report of the Intergovernmental Panel on Climate Change*. Cambridge University Press, Cambridge, United Kingdom and New York, NY, USA.

Rapp, M., Thomas, G.E., (2006). Modeling the microphysics of mesospheric ice particles: assessment of current capabilities and basic sensitivities. *Journal of Atmospheric and Solar-Terrestrial Physics* 68, pp. 715–744.

Reid, G.C. (1997). *The nucleation and growth of ice particles in the upper mesosphere.* Coupling and Energetics in the Stratosphere-Mesosphere- Thermosphere-Ionosphere System, 20. 1285-1291.

Remsburg, E.E., Bhatt, P.P., Deaver, L.E., 2002. Seasonal and long term variations in middle atmosphere temperature from HALOE on UARS. *Journal of Geophysical Research* 107 (D19), 4411.

Rishbeth H., and R. G. Roble, Cooling of the upeer atmosphere by enhanced greenhouse gases-Modelling of the thermospheric and ionospheric effects, *Planet. Space Sci.* 40, 1011-1026 (1992).

Roble, R.G., Dickinson, R.E., "How will changes in carbon dioxide and methane modify the mean structure of the mesosphere and thermosphere?", Geophysical Research Letters, Vol 16, No. 12, pp. 1441-1444 (1989). doi:10.1029/GL016i012p01441

Rusch, D. W., Thomas, G. E., McClintock, W., Merkel, A. W., Bailey, S. M., Russell III, J.M., Randall, C.E., Jeppesen, C., Callan, M., 2009. The Cloud Imaging and Particle Size Experiment on the Aeronomy of Ice in the Mesosphere Mission: Cloud Morphology for the Northern 2007 season. *J. Atmos. Sol., Terr. Phys*.

Russell III, J. M., Bailey, S. M., Horányi, M., Gordley, L. L., Rusch, D. W., Hervig, M. E., Thomas, G. E., Randall, G. E., Siskind, D. E., Stevens, M. H., Summers, M. E.,Taylor, M. I., Englert, C. R., Espy, P. J., McClintock, W. E., Merkel, A. W., 2009. Aeronomy of Ice in the Mesosphere (AIM): Overview and early science results. *J. Atmos. Sol. Terr. Phys.*

Shettle, E.P., DeLand, M.T., Thomas, G.E., Olivero, J.J., Long term variations in the frequency of polar mesospheric clouds in the Northern Hemisphere from SBUV, *Geophysical Research Letters, Vol. 36,* L02803, 5 PP., 2009. doi:10.1029/2008GL036048

Shi, L., Allen, C.T., Ledfford, J.R., Rodriguez-Morales F., Blake, W.A., Panzer, B.G., Prokopiack, S.C., Leuschen, C.J., Gogineni, S.,"Multichannel Coherent Radar Depth Sounder for NASA Operation Ice Bridge." IGARSS'2010. pp.1729-1732.

Steffen, K., J. E. Box, and W. Abdalati, 1996 "Greenland Climate Network: GC-Net", in Colbeck, S. C. Ed. CRREL 96-27 Special Report on Glaciers, Ice Sheets and Volcanoes, trib. to M. Meier, pp. 98-103.

Stevens, M. H., Gumbel, J., Englert, C. R., Grossmann, K. U., Rapp, M., Hartogh, P., "Polar Mesospheric Clouds Formed From Space Shuttle Exhaust", *Geophysical Research Letters,* vol. 30, issue 10, 2003.

Taylor, M.J., Hapgood, M.A., Simmons, D.A.R., 1984. The effect of atmospheric screening of the visible border of noctilucent clouds. *Journal of Atmospheric Terrestrial Physics* 14, pp. 865–869.

Taylor, M.J., Gadsden, M., Low, R.P., Zalcik, M.S., Brausch, J., 2002. Mesospheric cloud observations at unusually low latitudes. *Journal of Atmospheric and Solar-Terrestrial Physics* 64, pp. 991–999.

Taylor, M.J., 2009. Coordinated optical and radar image measurements of noctilucent clouds and polar mesospheric summer echoes, Journal of Atmospheric and Solar-Terrestrial Physics, Vol 71, Issue 6-7, Pages 675-687.

Thayer, J.P. et al., 'Noctilucent cloud observations over Greenland by a Rayleigh lidar' Geophysical Research Letters, Vol. 22, No. 21, pp. 2961-2964, 1995.

Thomas, R. H. Abdalati W, Frederick E, Krabill WB, Manizade S, Steffen K, (2003) Investigation of surface melting and dynamic thinning on Jakobshavn Isbrae, Greenland. Journal of Glaciology 49, 231–239.

Thomas, G. E., 2003. Are noctilucent clouds harbingers of global change in the middle atmosphere? *Adv. Space Res., 32*, 9, 1737-1746.

Thomas, G.E. et al., 'Relation between increasing methane and the presence of ice clouds at the mesopause', *Nature*, Vol. 338, 1989.

Thomas, G.E., 1991. Mesospheric clouds and the physics of the mesopause region. Reviews of Geophysics 29, 553–576.

Thomas G.E., MacKay C.P.,(1985) On the mean particle size and water content of polar mesospheric clouds. Planet. Space Sci. 33: 1209-1224.

Turco, R.P., Toon, O.B., Whitten, R.C., Keesee, R.G., Hollenback, D., 1982. Noctilucent clouds: simulation studies of their genesis, properties and global influences. Planetary and Space Science 30, pp. 1147–1181.

"Volcanic Gases and Their Effects". U.S. Department of the Interior. 2006-01-10.

von Savigny, C., S. V. Petelina, B. Karlsson, E. J. Llewellyn, D. A. Degenstein, N. D. Lloyd, and J. P. Burrows (2005), Vertical variation of NLC particle sizes retrieved from Odin/OSIRIS limb scattering observations, Geophys. Res. Lett., 32, L07806, doi:10.1029/2004GL021982.

von Zahn, U., 2003. Are noctilucent clouds truly a ―miner's canary‖ of global change? *Eos, Transactions, American Geophysical Union* 84 (28), pp. 261–268.

von Zahn, U. et al., 'Noctilucent clouds and the mesospheric water vapour: the past decade', *Atmos. Chem. Phys.*, 4, 2449–2464, 2004.

Witt, G., 1962. Height, structure and displacements of noctilucent clouds, *Tellus* 14, pp. 1–18.

Witt G. (1969) The nature of noctilucent clouds". Space Res IX:157-169.

Zwally, J.H., Abdalati, W, Herring, T., Larson, Kristine, Saba, J. Steffen, K. "Surface Melt-Induced Acceleration of Greenland Ice-Sheet Flow ", Science 12 July 2002: Vol. 297 no. 5579 pp. 218-222 DOI: 10.1126/science.1072708.

Zwally, H.J., Li, J., Brenner, A.C., Beckley, M., Cornejo, H.G., DiMarzio, J., Giovinetto, M.B., Neumann, T.A., Robbins, J., Saba, J.L., Yi, D., Wang, W., 'Greenland ice sheet mass balance: distribution of increased mass loss with climate warming; 2003–07 versus 1992–2002', Journal of Glaciology, Vol. 57, No. 201, 2011.

Zwally, H.J., Overview of Ice-Sheet Mass Balance and Dynamics from ICESat Measurements, American Geophysical Union, Fall Meeting 2010, abstract #U34A-01.

Websites:

www.spotimage.com

www.epa.gov/climatechange/emissions/index.html

www.nsidc.org/data/docs/measures/nsidc0478_joughin/index.html

www.nasa.gov/centers/goddard/news/topstory/2003/0313irradiance.html

www.espo.nasa.gov/oib

www.aim.hamptonu.edu

www.esrl.noaa.gov/gmd/ccgg/trends/

www.aim.hamptonu.edu/instrmt/cde

www.csr.utexas.edu/grace/